

DISSERTATION

COHERENT EUV LITHOGRAPHY WITH TABLE-TOP LASER

Submitted by

Lukasz Urbanski

Department of Electrical and Computer Engineering

In partial fulfillment of the requirements

For the Degree of Doctor of Philosophy

Colorado State University

Fort Collins, Colorado

Fall 2012

Doctoral Committee:

Advisor: Mario C. Marconi

Randy A. Bartels

Carmen S. Menoni

Vakhtang Putkaradze

ABSTRACT

COHERENT EUV LITHOGRAPHY WITH TABLE-TOP LASER

This dissertation describes alternative techniques of optical lithography in the extreme ultraviolet (EUV) region of the electromagnetic spectrum. The pursuit of the Moore's law forces the semiconductor industry to transfer to shorter wavelengths of illumination in projection lithography. The EUV light is perhaps the most viable candidate for the next generation integrated circuits printing. However, the EUV lithography encounters many challenges associated with the very nature of the light it is using. Many novel techniques and materials are being applied at the same time in the lithography process. As such the process itself is far from being reliable. Thus the solutions are being sought among the alternative methods of printing in the nano-scale that would aid to temporarily overpass the resolution gap.

This thesis contains a description of several alternative techniques of nanofabrication with the EUV light. For each method the analytical description is provided that is further corroborated with numerical model simulations. Furthermore every technique presented here is verified experimentally. The proposed techniques are discussed in terms of their applicability as a self consistent nanofabrication process.

The illumination source for all the techniques presented is the capillary discharge laser (CDL) that was engineered at Colorado State University; it is characterized in the chapter 2 of this dissertation. The CDL is an unbeatable table-top source of high average power illumination with the degree of coherence that is sufficient for coherent nano-scale printing. A separate chapter is dedicated to the description of the fabrication protocol of a diffractive optical element

(the mask) used in the EUV nanopatterning techniques. This particular chapter is intended to serve as a potential reference manual for the EUV masks fabrication. The coherent EUV nanofabrication techniques described in the chapters 4-6 are: the holographic projection lithography, generalized Talbot imaging (GTI), and de-magnified generalized Talbot imaging. A separate chapter is devoted to the defect tolerance property of the GTI technique.

ACKNOWLEDGEMENTS

I would like to thank Professor Mario C. Marconi for giving me the opportunity to work with him at the Colorado State University's Engineering Research Center for Extreme Ultraviolet Science and Technology. I would like to thank my committee members: Professor Randy A. Bartels, Professor Carmen S. Menoni, and Professor Vakhtang Putkaradze for their involvement and for reading of this thesis. I would like to thank Professor Jorge J. Rocca, Dr. Aaron Stein, and Dr. Ming Lu for their valued input to this thesis. I would also like to acknowledge all my coworkers especially: Wei Li, Ilya Kuznetsov, Dr. Dinesh Patel, Dr. Christopher G. Brown, Nils Monserud, Dr. Przemyslaw Wachulak, Dr. Brendan Reagan, Keith Wernsing, Isela Howlett, Dr. Jing Li, Michael Grisham, Dr. Fernando Brizuela, and Professor Bradley M. Luther.

I would like to thank my wife, Malgorzata Urbanska, my family and my friends for their love and support.

This work was supported by the National Science Foundation, award ECCS 0901806, the NSF ERC for Extreme Ultraviolet Science and Technology, award EEC 0310717. This research was carried out in part at the Center for Functional Nanomaterials, Brookhaven National Laboratory, which is supported by the U.S. Department of Energy, Office of Basic Energy Sciences, under Contract No. DE-AC02-98CH10886.

TABLE OF CONTENTS

CHAPTER 1	INTRODUCTION.....	1
1.1	NANOTECHNOLOGY OVERVIEW.....	1
1.2	APPLICATIONS	3
1.3	NANOFABRICATION	6
1.4	EXTREME ULTRAVIOLET AND SOFT X-RAY LITHOGRAPHY.....	11
1.5	ALTERNATIVE EUV LITHOGRAPHY NANOFABRICATION	12
1.6	REFERENCES.....	15
CHAPTER 2	THE CAPILLARY DISCHARGE LASER	22
2.1	INTRODUCTION.....	22
2.2	HIGH AVERAGE POWER.....	22
2.3	SPATIAL COHERENCE OF THE CDL.....	27
2.4	TEMPORAL COHERENCE OF THE CDL	32
2.5	SUMMARY	38
2.6	REFERENCES.....	39
CHAPTER 3	MASK FABRICATION	45
3.1	INTRODUCTION.....	45
3.2	MASK DESIGN.....	46
3.2.1	MATERIALS CONSIDERATIONS	46

3.2.2	FABRICATION PROTOCOL.....	50
3.3	MASK DESIGN.....	56
3.4	ELECTRON BEAM LITHOGRAPHY.....	58
3.4.1	SYSTEM OVERVIEW	58
3.4.2	STAGE-POSITION DETECTION.....	61
3.4.3	FILES PREPARATION FOR E-BEAM LITHOGRAPHY.....	62
3.5	REFERENCES.....	64
CHAPTER 4 HOLOGRAPHIC LITHOGRAPHY.....		66
4.1	INTRODUCTION.....	66
4.2	CGH DESIGN.....	67
4.2.1	Fresnel Propagation	67
4.2.2	Phase optimization.....	70
4.2.3	Halftoning.....	71
4.3	HARD THRESHOLD DESIGN	72
4.4	DITHERING DESIGN	74
4.5	NUMERICAL RECONSTRUCTION.....	77
4.6	EXPERIMENTAL SETUP AND RESULTS	79
4.7	SUMMARY.....	84
4.8	REFERENCES.....	86
CHAPTER 5 GENERALIZED TALBOT IMAGING.....		88

5.1	INTRODUCTION.....	88
5.2	HISTORICAL BACKGROUND.....	88
5.3	ANALYTICAL DESCRIPTION.....	89
5.4	NUMERICAL SIMULATION.....	93
5.5	GENERALIZED TALBOT EFFECT.....	94
5.6	APPLICATION OF GENERALIZED TALBOT IMAGING TO NANOPATTERNING 97	
5.7	SUMMARY.....	106
5.8	REFERENCES.....	107
CHAPTER 6 DEMAGNIFIED TALBOT IMAGING.....		111
6.1	INTRODUCTION.....	111
6.2	ANALYTICAL DESCRIPTION.....	112
6.3	NUMERICAL SIMULATION.....	116
6.4	DGTI EXPERIMENT.....	117
6.5	LIMITATIONS.....	123
6.6	SUMMARY.....	127
6.7	REFERENCES.....	129
CHAPTER 7 DEFECT TOLERANT GENERALIZED TALBOT IMAGING.....		131
7.1	INTRODUCTION.....	131
7.2	ANALYTICAL DESCRIPTION.....	132

7.3	NUMERICAL SIMULATION	135
7.4	EXPERIMENTAL VERIFICATION OF DEFECT TOLERANCE	137
7.4.1	MASK DESIGN	137
7.4.2	EXPERIMENTAL SETUP.....	140
7.4.3	EXPERIMENTAL RESULTS.....	141
7.5	DATA ANALYSIS	144
7.6	SUMMARY	148
7.7	REFERENCES.....	149
APPENDIX 1	DERIVATION OF THE TALBOT DISTANCE IN THE DEMAGNIFIED TALBOT IMAGING.....	151
APPENDIX 2	RESIST PROCESSING	154
APPENDIX 3	NUMERICAL CALCULATIONS.....	158

CHAPTER 1 INTRODUCTION

1.1 NANOTECHNOLOGY OVERVIEW

“There is plenty of room at the bottom”, a seminar given by Richard Feynman in 1959 at the annual meeting of the APS at Caltech became an invitation for the scientists to enter the nanoworld [1]. Feynman foresaw the new possibilities arising from the exploration of the nanoscale (*nanos gr. dwarf*) physics in the late 1950s. By his inspirational speech, he has laid the foundation of what is at present known as the nanotechnology. After over half of a century has elapsed since Feynman’s famous invitation, the impact of nanotechnology on the science became tremendous. As a broad and interdisciplinary area of research and development activity, nanotechnology undergoes an explosive growth worldwide in the past few decades. The potential of nanotechnology for revolutionizing the ways in which materials and products are created pervades in the course of years. Not only does it thrive on straightforward transfer of existing concepts from the macro and micro scales, but also provides for exploration of new nature and range of functionalities in the nanoworld. It is already a self-standing branch of science and as such it is having a significant scientific and economic impact, which will assuredly increase in the future.

The realm of the nanoworld has been an inseparable part of nature ever since. It is only few decades since humans have learned how to peek upon this natural set of nanotechnologies. The inventions and advancement of electron microscopy and scanning probe techniques enabled scientists to understand and often draw inspiration from the nanoworld [2-5].

Figure 1-1 illustrates a chart of scales accompanied by their objects representatives [6]. The chart is divided to natural and manmade objects.

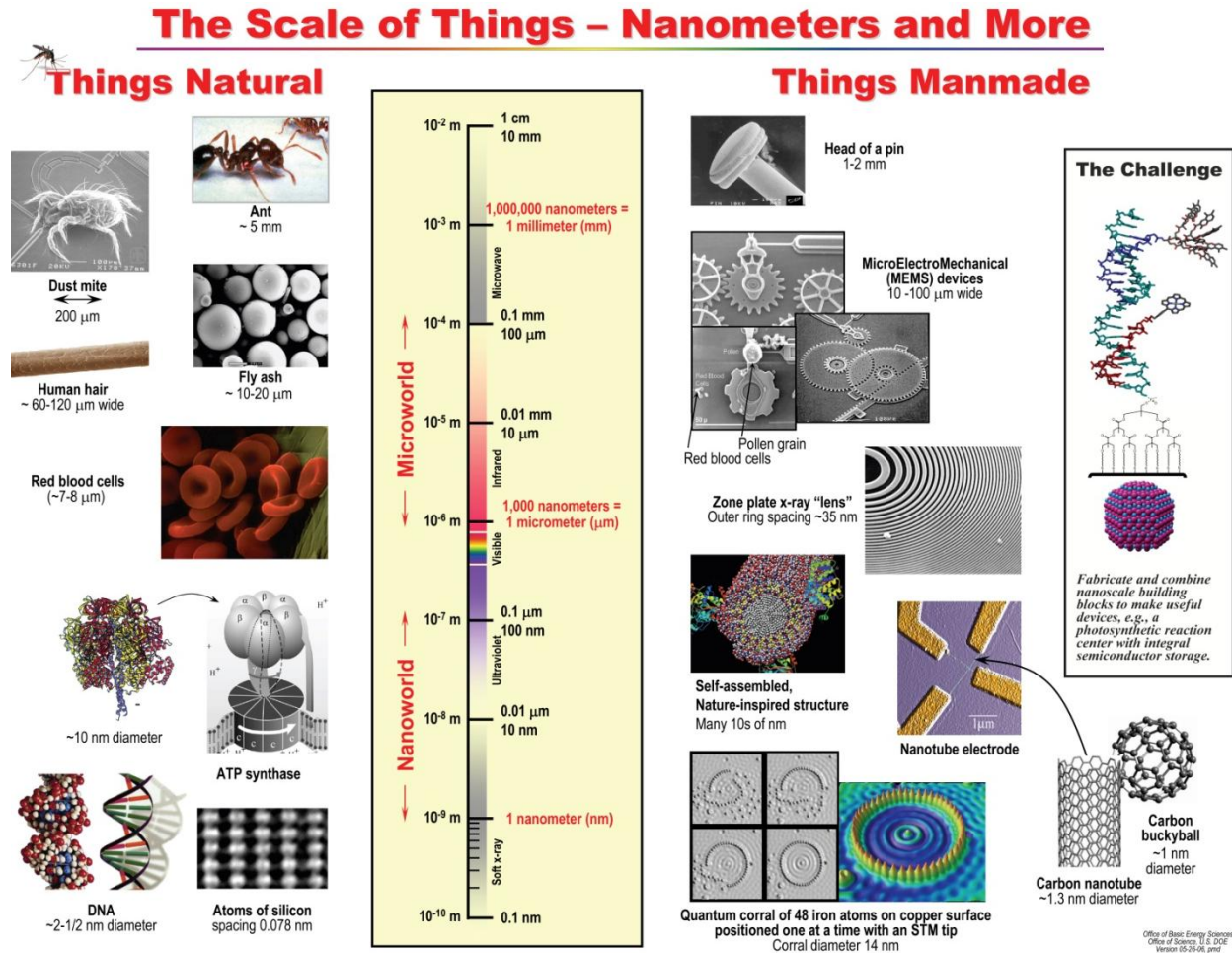
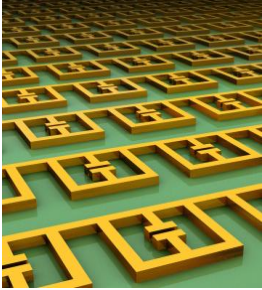
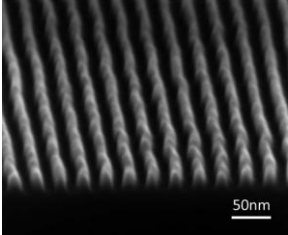



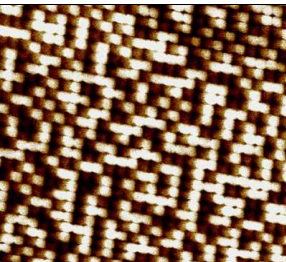
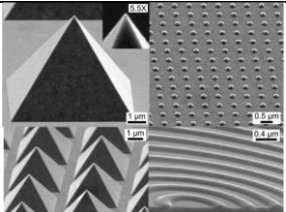
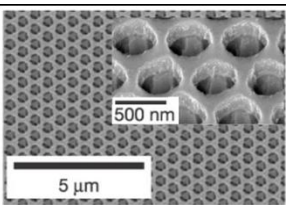
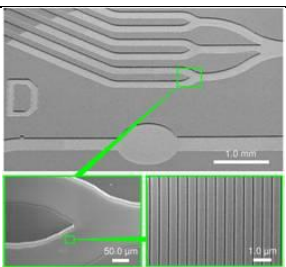
Figure 1-1. The scale of things. (Graphic adopted from the US Department of Energy ,basic energy sciences.)

Exploration of the nanoworld has become a new theme common to many disciplines. In electronics, the emergence of fabrication tools and techniques capable of constructing structures with dimensions ranging from 0.1 to 50 nm has opened up numerous possibilities for investigating new devices in a size domain hitherto inaccessible to experimentalists and thus provided for further pursuit of the Moore’s law [7].

1.2 APPLICATIONS

Nanotechnology as a branch of science experiences an impetuous growth. Entire branches of science based on nanotechnology such as photonics and plasmonics have been derived and cultivated in the course of years. In electrical and mechanical engineering, a new class of nanostructures called micro electro-mechanical systems (MEMS) has emerged revealing unique mechanical and electro-magnetic characteristics of materials unobservable in the macro and micro scales [8]. New alloys and composites with radically improved properties emerge as the nanotechnology permeates the material sciences. The nature of cell-driving mechanisms that rely on the nanostructures can now be studied in molecular biology [9].

Application	Figure	Reference
Metamaterials		[10]
Guided self assembly		[11]

<p>Micro electro mechanical systems (MEMS)</p>	 <p>A grayscale photograph showing several interlocking gears of various sizes, which are micro-electromechanical systems (MEMS) components.</p>	<p>[12]</p>
<p>Nanomagnetics</p>	 <p>A false-color scanning electron micrograph (SEM) showing a dense array of small, rectangular magnetic structures on a surface.</p>	<p>[13]</p>
<p>Plasmonics</p>	 <p>A grayscale SEM image showing various plasmonic structures, including a large triangular structure, a series of parallel ridges, and a grid of small circular holes. Scale bars are visible: 1 μm, 0.5 μm, and 0.4 μm.</p>	<p>[14]</p>
<p>Photonics</p>	 <p>A grayscale SEM image showing a periodic array of circular holes in a material. A scale bar indicates 5 μm. An inset shows a magnified view of the holes with a 500 nm scale bar.</p>	<p>[15]</p>
<p>Microfluidics</p>	 <p>A grayscale SEM image of a microfluidic device. It shows a network of channels and chambers. A scale bar indicates 1.0 mm. A green box highlights a specific region, which is magnified in an inset below. The inset shows a close-up of the channel walls with a 50.0 μm scale bar and a 1.0 μm scale bar.</p>	<p>[16]</p>

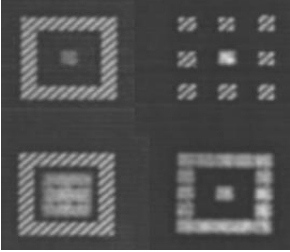
Genomics		[17]
----------	--	------

Figure 1-2. Chart of selected applications of the nanostructures.

Figure 1-2 is a fusion of several selected applications of nanostructures. The first one uses nanopatterned arrays of split ring resonators (SRR). As an ensemble, they exhibit very specific properties in terms of their response to the electromagnetic radiation. These properties are very much different from the properties of the bulk material used for building the SRRs. By using such materials (also referred to as metamaterials) one has the ability to tune their electromagnetic constants. For example, the transmission coefficient of an array of SRRs changes its value by 60% while illuminated by ~50 fs, 800 nm pulse. Thus such material has the potential of being used as a switch. What is important to notice, the switching behavior of metamaterial is solely due to its shape and size [10].

Next example is a template for guided self assembly. As described in [11] a template (lines) is created by means of optical projection lithography (193nm, immersion). Subsequently, it is transferred to a layer of cross-linkable polystyrene. A block copolymer was then applied self-assembling into structures fitting in-between the polystyrene lines, thus multiplying the template lines period. Such a double patterning technique has the potential of being used in the interim until the next generation nanofabrication tools based on the EUV lithography are fully available. Another example shown are patterned arrays of magnetic media. In the case presented, a matrix

of multilayered nanodots made of cobalt and palladium is obtained by the means of electron beam lithography. Such arrays have the potential to increase the memory density to 1 Tbit/inch². Another very interesting example of nanostructures application is plasmonics. Succinctly speaking, nanostructures made of certain metals (gold, silver) exhibit localized electron cloud oscillation that can be excited by photons. Such collective oscillations are referred to as plasmon polaritons. They are observable in thin metallic layers of various nanostructures. Special interest is put on fabrication of devices enabling efficient coupling of plasmons to the material. This can be achieved via nanofabrication. Some examples of plasmon polaritons launching structures can be found in [14]. Plasmonics is a very dynamically growing field of science. Possible applications of plasmons are in lithography and detection.

There are, of course, many other examples of nanostructures applications such as microfluidics or genomics [16, 17], in this brief introduction a selected set of nanostructures was chosen to exemplify the broad field of application of nanostructures

1.3 NANOFABRICATION

The term nanotechnology was coined by Noiro Taniguchi in 1974. It refers to the “ability of engineering materials precisely at nanometer scale” [18]. There are multiple techniques to manipulate materials in the nanoscale. They can be divided with regard to the physical mechanism interaction with the material. This work is intended to address only the nanopattern fabrication and rather restrain from further material functionalization (etching, metallization).

Thus, the nanofabrication methods most commonly used are:

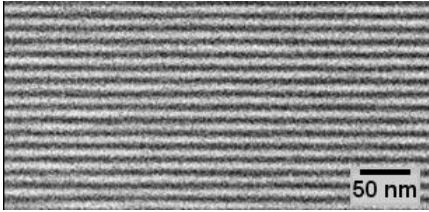
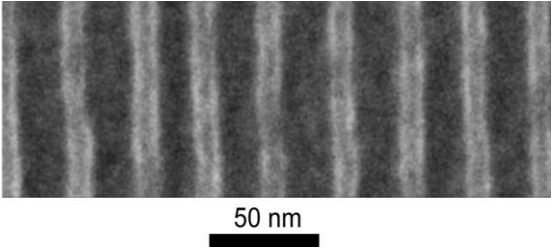
- optical lithography,
- electron beam lithography,

- nanoimprint lithography,
- scanning probe lithography.

At this point, it is worthwhile to devote some explanation to the word “lithography”. Historically, lithography, is a process in which a master pattern is being transferred from one surface (originally from smooth surface of a wood, stone and later metal) to another (paper) by the selective use of ink repellent and ink receptive materials [19]. By an analogy, in all the aforementioned lithography types the material is being shaped in the course of interaction with different writing media. In the optical lithography, photons are used to activate a layer of photoresist at loci corresponding to the bright spots in the master mask. In electron beam lithography, the resist is being irradiated by thin pencil of electrons finely focused by means of electron optics. Nanoimprint lithography shares the most commonalities with the primitive lithography concept. As such, it uses a hard stamp which is being embossed in a layer of soft monomer or polymer resist that is being subsequently cured with either UV light or heat. Scanning probe lithography is a family of techniques where the resist is being modified by fine tip of extremely small radius actuated by a piezo-driven stage. Below is a chart comparing the capabilities of the lithography techniques enlisted above. The second column contains electron micrographs of resist patterned with various techniques, whereas the third column provides with the critical dimension achieved by a specific technique. It is important to understand, that all the aforementioned techniques of nanofabrication have both their advantages and caveats, and that is naive to compare them solely on the basis of the critical dimension achievable.

The optical lithography is a powerful technique, which uses photons as the writing medium. A master mask is illuminated by intense light emanating from either an argon fluoride (ArF~193nm) or krypton fluoride (KrF~248nm) excimer lasers through an optical system referred

to as the reduction camera (or stepper). The demagnified image of the mask is then recorded in a resist coated wafer [24]. Among all the aforementioned methods it is the most widely used by the semiconductor industry in fabrication of computer chips in the present. According to the Semiconductor Industry Association (SIA) and the Technology Roadmap for Semiconductors, which provides a 15 years (or 6generations) projection of the integrated circuits characteristics, optical lithography is anticipated as the most successful candidate for manufacturing of next generation logical devices [19].

Technique	Result	Critical dimension
Optical lithography		11nm [20]
Electron beam lithography		2.5nm [21]

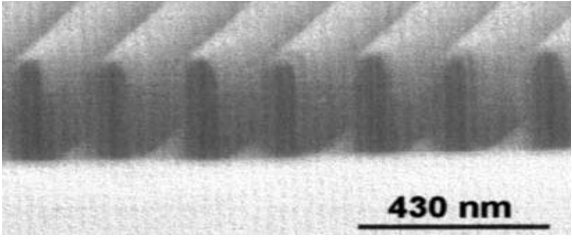
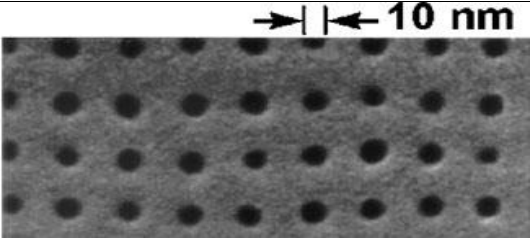
<p>Scanning probe lithography</p>		<p>65nm [22]</p>
<p>Nanoimprint lithography</p>		<p>10nm [23]</p>

Figure 1-3. Chart comparing different nanofabrication techniques and record critical dimension thereof.

The main limitation of this method is given by the diffraction limit because the critical dimension is limited by the wavelength of illumination and the numerical aperture of the optical system [25]. The unparalleled advantage of this method lays in its high throughput.

The electron beam lithography (EBL) provides the world’s smallest features manmade [21]. It utilizes a high energy (typically 10-100keV), low current (pA~nA) electron beam to write patterns of choice onto the surface of the resist. The beam is shaped by electron optics that is focusing it down to the desired diameter and correcting for aberrations. EBL tools were derived from the early scanning electron microscopes. The process of forming the beam of electrons and scanning it across a surface is very similar to what happens inside the cathode ray tube (CRT) display, but EBL typically has three orders of magnitude better resolution. The main advantages of the technology are its capability of printing with very high resolution, almost to the atomic level and compatibility with a variety of materials and an almost infinite number of patterns. The

main caveats of EBL are: it is a serial process which means it is slow (being one or more orders of magnitude slower than optical lithography); it is expensive and complicated. The electron beam lithography tools require frequent service to stay properly maintained [24].

Another class of methods of nanofabrication to be succinctly described here is nanoimprint lithography. Nanoimprint lithography (NIL) is a promising approach to nanofabrication in its early stage of development. Among the mentioned techniques, it has the strongest premise to be associated with the historical lithography. In NIL one uses a hard stamp (or a mold) which is fabricated using either optical or EB lithography which is being embossed in soft resist. NIL is a robust technique, which offers high throughput. Often times during the imprint process, the resist is cured either with ultraviolet light or heat to promote better pattern definition. Such a derivative of NIL is referred to as UV-NIL. NIL is a versatile technique; the materials used for nanoimprint include imprintable dielectrics, conducting polymers, biocompatible materials, and materials for microfluidic devices. One significant advantage of NIL is its potential to decrease the cost of nanofabrication with simultaneous increasing the throughput as compared to EBL. Photocuring adds another constraint on materials design, but offers the advantages of using a low-viscosity imprint resist especially in high-throughput and multilevel device fabrication. The development of a photocurable interlayer dielectric may have a significant impact on the semiconductor industry by simplifying the fabrication processes [26]. Thus NIL can be considered to be more than just a mere scientific curiosity. An obvious disadvantage on NIL is the fact that it is a contact method of nanofabrication. As such it is characterized by mold wearing out and contamination. The method is also very defect prone, as resist leftovers adhere to the mold surface rendering subsequent prints to be less accurate.

1.4 EXTREME ULTRAVIOLET AND SOFT X-RAY LITHOGRAPHY

Perhaps the widest use of nanofabrication is found in the semiconductor industry. It continues to derive profit from device scaling. Thus any technique that promises to extend dimensional scaling receives great deal of attention from this specific industry branch [27]. As can be readily seen in the paragraph describing the optical lithography, the critical dimension of the printable feature depends on the wavelength of illumination and the numerical aperture of the imaging system. It is then natural, to project that the relentless pursuit of the semiconductor industry for smaller feature size will eventually turn its attention towards application of shorter wavelengths. Extreme ultraviolet (EUV) and soft X-ray light occupies the region of electromagnetic spectrum that lays between 1 and 50nm, as can be seen on the Figure 1-4 [19]. EUV radiation at 13.5nm wavelength is the most plausible candidate to be employed in the next generation integrated circuit printing [27].

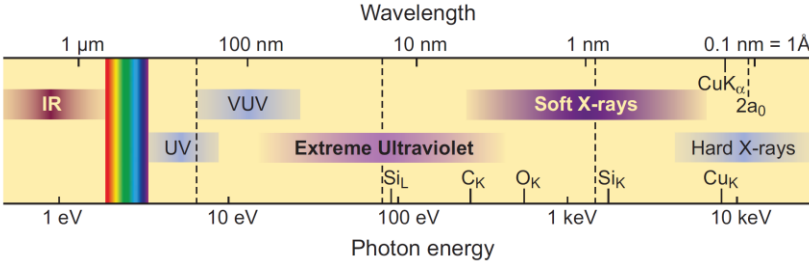


Figure 1-4. Extreme ultraviolet and soft x-ray radiation placement in the electromagnetic radiation spectrum. (Adopted from reference [19]).

The first papers proposing the use of EUV or soft x-ray radiation for projection lithography were published in the late 1980's [28-33]. Nowadays, the extensions of conventional optical lithography have continued to dominate semiconductor device manufacturing [34]. Although much effort is being devoted to make the transition from classical optical projection lithography to EUV lithography possible, there is many issues which have yet to be addressed in order to make the shift seamless. There are many degrees of freedom in the process, which have to be tamed simultaneously in order for it to bear fruit. The main challenges are the light source, multilayer optics, debris mitigation, mask and resist. Each of these components represents state of the art advancement in its domain.

1.5 ALTERNATIVE EUV LITHOGRAPHY NANOFABRICATION

While EUVL is still coping with addressing some reliability issues to reduce the cost of ownership for high volume manufacturing, in the low volume manufacturing, nanofabrication solutions are being sought among alternative techniques. Even for the industrial purposes, there is a high interest in the unconventional methods of nanofabrication, as they could be the most viable candidates for linking the resolution gap in the interim. Some of the alternative methods use EUV light in arrangements different from the conventional projection scheme used in the EUVL reduction cameras.

Several techniques which are subject to this dissertation are described in the subsequent chapters. They are all using the capillary discharge laser (CDL), which emits light at $\lambda=46.9\text{nm}$ as the source of illumination. The light emission from CDL is characterized by high average power and both spatial and temporal coherence [35-38]. Providing light with the aforementioned parameters, the CDL has been used in many applications [39-49]. The illumination coherence is

crucial from the point of view of the nanofabrication techniques presented in this thesis. High degree of temporal and spatial coherence is necessary for high quality pattern generation in the methods presented. Chapter 2 is fully devoted to the description of the capillary discharge laser. The conclusions drawn from the experimental work presented in the chapter 2 set the optimum operating conditions for of the CDL for applications such as nanofabrication. The work described in this chapter has been published in [35-38].

Chapter 3 provides with a detailed description of the diffractive optics (or masks) fabrication. Each nanofabrication experiment described in this thesis required a corresponding diffractive mask. The masks are crucial elements which interact with the EUV light. Their complexity in terms of specialized materials applied and dedicated fabrication techniques make them state of the art devices for nanofabrication with the EUV light. The amount of work invested in the fabrication of the specialized diffractive EUV optics well grants them a chapter in this dissertation.

Chapter 4 describes holographic projection lithography with coherent EUV light. Two different methods of designing a computer generated hologram (CGH) are discussed. Analytical description of the CGHs' reconstruction in terms of the solution to the Fresnel-Kirchhoff integral is provided. Deterministic relations are supported by numerical analysis. An experimental verification of the theoretical prediction is conducted. The numerical results obtained are in very good correspondence with the theory. Limitations of the method and its potential as a viable technique for nanofabrication are discussed. The work described in this chapter has been published in [48].

Chapter 5 describes an interesting approach to nanopatterning called the generalized Talbot imaging (GTI). In this technique, a periodic array of arbitrarily designed patterns is illuminated with coherent light supplied from the CDL. Due to the self-imaging effect, such periodic pattern creates a replica of itself at certain discrete distances. Those replicas are recorded in the photoresist. A theoretical account of the effect is introduced, both analytical and numerical. Most importantly, the experimental verifications are presented. The results are in good correspondence with theoretical predictions. GTI is a non-contact, high fidelity, high resolution, defect tolerant optical imprint technique. The work presented in this chapter resulted in the publication [47].

Chapter 6 is an account of an extension of the GTI technique by adding a size scalability feature to the already rich spectrum of its properties. It is called the demagnified generalized Talbot imaging and abbreviated DGTI. The limits of the applicability of this particular method are explained. The results presented in this chapter have been published in [49].

Chapter 7 treats about the defect tolerance property of the GTI technique. The problem is attacked both theoretically and experimentally. A GTI mask with a purposefully planted defect is fabricated and illuminated with coherent EUV light in order to investigate the degree of defect tolerance. Different defect layouts and concentrations are tested to provide a general answer to the question about the extent of defect tolerance. The work presented in this chapter has been published in [50].

1.6 REFERENCES

- [1] *Transcript of the talk from December 29th 1959 at the annual meeting of the American physical society at the California institute of technology*, R. Feynman, (1959).
- [2] *The Development Of The Electron-Microscope And Of Electron-Microscopy*, E Ruska. *Reviews Of Modern Physics*, **59**, 627 (1987).
- [3] *Surface Studies By Scanning Tunneling Microscopy*, G. Binnig, H. Rohrer, C. Gerber, and E. Weibel, *Phys. Rev. Lett.* **49**, 57 (1982).
- [4] *Nanomotor rotates microscale objects*, R. Eelkema, M.M. Pollard, J. Vicario, N. Katsonis, B.S. Ramon, C.W.M. Bastiaansen, D.J. Broer, and B.L. Feringa, *Nature*, **440**, 163 (2006).
- [5] *Nature-Inspired Molecular Machines*. A. Lawit, J. Bala-Krishna and T. J. Huang, *Wiley-VCH Verlag* (2007).
- [6] *The scale of things*, US Department of Energy Basic Energy Sciences, (2006).
- [7] *Cramming more components onto integrated circuits*, G.E. Moore, *IEEE Proc.* **86**, 82 (1998).
- [8] *Geometry-dependent casimir forces on a silicon chip*, J. Zou, Z. Marcet, A.W. Rodriguez, M.T.H. Reid, A.P. McCauley, I.I. Kravchenko, T. Lu, Y. Bao, S.G. Johnson, and H.B. Chan, *ArXiv e-prints* (2012).

- [9] *Ergodic and nonergodic processes coexist in the plasma membrane as observed by single-molecule tracking*, A.V. Weigel, B. Simon, M.M. Tamkun, and D. Krapf, *Proc. Nat. Acad. Sci.* **108**, 6438 (2011).
- [10] *Dynamical electric and magnetic metamaterial response at terahertz frequencies*, W. J. Padilla, A. J. Taylor, C. Highstrete, Mark Lee, and R. D. Averitt, *Phys. Rev. Lett.*, **96**, 107401 (2006).
- [11] *Integration of block copolymer directed assembly with 193 immersion lithography*, Chi-Chun Liu, Paul F. Nealey, Alex K. Raub, Philip J. Hakeem, Steve R. J. Brueck, Eungnak Han, and Padma Gopalan, *J. Vac. Sci. Technol. B* **28**, C6B30 (2010).
- [12] *MEMS*, P.N. Mahalik, *McGraw-Hill Education* (2008).
- [13] *Origins of switching field distributions in perpendicular magnetic nanodot arrays*, J.M. Shaw, W.H. Rippard, S.E. Russek, T. Reith, and C.M. Falco. *Journal of Applied Physics*, **101**, 023909 (2007).
- [14] *Ultrasmooth Patterned Metals for Plasmonics and Metamaterials*, P. Nagpal, N.C. Lindquist, S.H. Oh, and D.J. Norris. *Science*, **325**, 594 (2009).
- [15] *A three-dimensional optical photonic crystal with designed point defects*, MH Qi, E. Lidorikis, P.T. Rakich, S.G. Johnson, J.D. Joannopoulos, E.P. Ippen, and H.I. Smith. *Nature*, **429**, 538 (2004).
- [16] *Single-step fabrication and characterization of photonic crystal biosensors with polymer microfluidic channels*, C.J. Choi and B.T. Cunningham. *Lab Chip*, **6**, 1373 (2006).

- [17] *Biological lithography: Improvements in DNA synthesis methods*, C. Kim, M. Li, M. Rodesch, A. Lowe, K. Richmond, and F. Cerrina, *J. Vac. Science Technol. B*, **22**, 3163 (2004).
- [18] *On the Basic Concept of 'Nano-Technology'*, N. Taniguchi, *Bulletin of the Japan Society of Precision Engineering*, 18 (1974).
- [19] *Soft X-Rays and Extreme Ultraviolet Radiation Principles and Applications*. D.T. Attwood. *Cambridge University Press* (2007).
- [20] *Extreme ultraviolet interference lithography at the Paul Scherrer Institut*, V. Auzelyte, C. Dais, P. Farquet, D. Gruetzmacher, L.J. Heyderman, F. Luo, S. Olliges, C. Padeste, P.K. Sahoo, T. Thomson, A. Turchanin, C. David, and H.H. Solak. *Journal Of Micro-Nanolithography MEMS And MOEMS*, **8**, (2009).
- [21] *Comparison of hydrogen silsesquioxane development methods for sub-10 nm electron beam lithography using accurate linewidth inspection*, D. S. Macintyre and S. Thoms, *J. Vac. Sci. Technol. B* **29**, 06F307 (2011).
- [22] *Electron beam and scanning probe lithography: A comparison*. K. Wilder, C.F. Quate, B.Singh, and D.F. Kyser, *J. Vac. Sci. Technol. B* **16**, 3864 (1998).
- [23] *Sub-10 nm imprint lithography and applications*. S.Y. Chou, P.R. Krauss, W. Zhang, L.Guo, and L. Zhuangvolume, *J. Vac. Sci. Technol. B* **15**, 2897 (1997).
- [24] *Handbook of Microlithography, Micromachining, and Microfabrication: Microlithography*. P. Rai-Choudhury, *SPIE Optical Engineering Press* (1997).

- [25] *Principles of Optics: Electromagnetic Theory of Propagation, Interference and Diffraction of Light*, M. Born, E. Wolf, A.B. Bhatia, P.C. Clemmow, D. Gabor, A.R. Stokes, A.M. Taylor, P.A. Wayman, and W.L. Wilcock, *Cambridge University Press* (1999).
- [26] *Nanomanufacturing Handbook*. A. Busnaina. *CRC Press* (2006).
- [27] *EUV Lithography*, V. Bakshi, *SPIE Optical Engineering Press* (2009).
- [28] *X-ray lithography for sub-100-nm-channel-length transistors using masks fabricated with conventional photolithography, anisotropic etching, and oblique shadowing*, S. Y. Chou, H.I. Smith, and D. A. Antoniadis, *J. Vac. Sci. Technol. B* **3**, 1587 (1985).
- [29] *Sub-100-nm channel-length transistors fabricated using x-ray lithography*, S. Y. Chou, H.I. Smith, and D. A. Antoniadis, *J. Vac. Sci. Technol. B*, **4**, 253 (1986).
- [30] *II. Tenth micron lithography with a 10 Hz 37.2 nm sodium laser*, W.T. Silfvast and O.R. Wood, *Microelectronic Eng.* **8**, 3 (1988).
- [31] *Soft x-ray projection lithography using an x-ray reduction camera*, A.M. Hawryluk and L.G. Seppala. *J. Vac. Sci. Technol. B*, **6**, 2162 (1988).
- [32] *Soft x-ray reduction lithography using multilayer mirrors*, H. Kinoshita, K. Kurihara, Y. Ishii, and Y. Torii, *J. Vac. Sci. Technol. B*, **7**, 1648 (1989).
- [33] *Reduction imaging at 14 nm using multilayer-coated optics: Printing of features smaller than 0.1 μm* , J. E. Bjorkholm, J. Bokor, L. Eichner, R. R. Freeman, J. Gregus, T. E. Jewell, W. M. Mansfield, A. A. Mac Dowell, E. L. Raab, W. T. Silfvast, L. H. Szeto, D.

- M. Tennant, W. K. Waskiewicz, D. L. White, D. L. Windt, O. R. Wood II, and J. H. Bruning, *J. Vac. Sci. Technol. B*, **8**, 1509 (1990).
- [34] *Extreme ultraviolet lithography*. C. W. Gwyn, R. Stulen, D. Sweeney, and D. Attwood, *J. Vac. Sci. Technol. B*, **16**, 3142 (1998).
- [35] *Demonstration of a high average power tabletop soft x-ray laser*, B. R. Benware, C. D. Macchietto, C. H. Moreno, and J. J. Rocca. *Phys. Rev. Lett.* **81**, 5804 (1998).
- [36] *Generation of millijoule-level soft-x-ray laser pulses at a 4-hz repetition rate in a highly saturated tabletop capillary discharge amplifier*, C. D. Macchietto, B. R. Benware, and J. J. Rocca. *Opt. Lett.* **24**, 1115 (1999).
- [37] *Achievement of essentially full spatial coherence in a high-average-power soft-x-ray laser*, Y. Liu, M. Seminario, F. Tomasel, C. Chang, J. Rocca, and D. Attwood *Phys. Rev. A*, **63**, 1 (2001).
- [38] *Spectral linewidth of a Ne-like Ar capillary discharge soft-x-ray laser and its dependence on amplification beyond gain saturation*, L. Urbanski, M. C. Marconi, L. M. Meng, M. Berrill, O. Guilbaud, A. Klisnick, and J. J. Rocca, *Phys. Rev. A*, **85**, 033837 (2012).
- [39] *Determination of xuv optical constants by reflectometry using a high-repetition rate 46.9-nm laser*, I.A. Artioukov, B.R. Benware, J.J. Rocca, M. Forsythe, Yu.A. Uspenskii, and A.V. Vinogradov, *Selected Topics in Quantum Electronics, IEEE Journal of*, **5**, 1495 (1999).

- [40] *Dense plasma diagnostics with an amplitude-division soft-x-ray laser interferometer based on diffraction gratings*, J. Filevich, K. Kanizay, M. C. Marconi, J. L. A. Chilla, and J. J. Rocca, *Opt. Lett.* **25**, 356 (2000).
- [41] *Reflection mode imaging with nanoscale resolution using a compact extreme ultraviolet laser*, F. Brizuela, G. Vaschenko, C. Brewer, M. Grisham, C. Menoni, M. Marconi, J. Rocca, W. Chao, J. Liddle, E. Anderson, D. Attwood, A. Vinogradov, I. Artioukov, Y. Pershyn, and V. Kondratenko, *Opt. Express*, **13**, 3983 (2005).
- [42] *Demonstration of a desk-top size high repetition rate soft x-ray laser*, S. Heinbuch, M. Grisham, D. Martz, and J. J. Rocca, *Opt. Express*, **13**, 4050 (2005).
- [43] *Single photon ionization of hydrogen bonded clusters with a soft x-ray laser: HCOOH_x and $\text{HCOOH}_y(\text{H}_2\text{O})_z$* , S. Heinbuch, F. Dong, J. J. Rocca, and E. R. Bernstein . *The Journal of Chemical Physics*, **126**, 244301 (2007).
- [44] *Single-shot extreme ultraviolet laser imaging of nanostructures with wavelength resolution*, C.A. Brewer, F. Brizuela, P. Wachulak, D.H. Martz, W. Chao, E.H. Anderson, D.T. Attwood, A.V. Vinogradov, I.A. Artyukov, A.G. Ponomareko, V.V. Kondratenko, M.C. Marconi, J.J. Rocca, and C.S. Menoni, *Opt. Lett.* **33**, 518 (2008).
- [45] *Patterning of nano-scale arrays by table-top extreme ultraviolet laser interferometric lithography*, P. W. Wachulak, M. G. Capeluto, M. C. Marconi, C. S. Menoni, and J. J. Rocca, *Opt. Express*, **15**, 3465 (2007).
- [46] *Soft x-ray laser holography with wavelength resolution*, P. W. Wachulak, M. C. Marconi, R. A. Bartels, C. S. Menoni, and J. J. Rocca, *J. Opt. Soc. Am. B*, **25**, 1811 (2008).

- [47] *Talbot lithography: Self-imaging of complex structures*, A. Isoyan, F. Jiang, Y. C. Cheng, F. Cerrina, P. Wachulak, L. Urbanski, J. Rocca, C. Menoni, and M. Marconi, *J. Vac. Sci. Technol. B*, **27**, 2931 (2009).
- [48] *Extreme ultraviolet holographic lithography with a table-top laser*, A. Isoyan, F. Jiang, Y.C. Cheng, P. Wachulak, L. Urbanski, J. Rocca, C. Menoni, M. Marconi, and F. Cerrina, . *Proc. SPIE*, **7271**, 72713O (2009).
- [49] *Analysis of a scheme for de-magnified talbot lithography*, L. Urbanski, M. C. Marconi, A. Isoyan, A. Stein, C. S. Menoni, and J. J. Rocca. . *J. Vac. Sci. Technol. B*, **29**, 06F504 (2011).
- [50] *Defect tolerant extreme ultraviolet nanoscale printing*, L. Urbanski, A. Isoyan, A. Stein, J.J. Rocca, C.S. Menoni and M.C. Marconi, *Opt. Lett.* **37**, 3633 (2012).

CHAPTER 2 THE CAPILLARY DISCHARGE LASER

2.1 INTRODUCTION

This chapter describes the light source that was used in coherent EUV nanopatterning experiments which are the subject of this dissertation, the capillary discharge laser (CDL). The CDL, first demonstrated in 1994 [1], remains to date the highest average power tabletop source of coherent EUV light [2, 3]. The CDL, developed at Colorado State University, is an amplified spontaneous emission (ASE) Ne-like Ar laser operating at $\lambda = 46.9$ nm. The characteristics of the CDL such as high photon flux, temporal and spatial coherence make it also the tabletop soft-x-ray laser most broadly utilized in applications. It has been used in interferometric studies of high-density plasmas [4], high-resolution microscopy [5, 6], holographic imaging [7], nanoscale patterning and machining [8, 9], material ablation [10, 11], single-photon ionization mass spectrometry studies of nanoclusters [12], the measurement of optical constants of materials [13], and other applications.

This chapter describes the three properties of the CDL, which make it well suited for applications in nanofabrication; namely high average power, spatial and temporal coherence. The chapter is sectioned in to three parts, each of which treats the aforementioned aspect.

2.2 HIGH AVERAGE POWER

High average power is a property highly desired in laser applications such as nanofabrication, nanomachining, nanoscale ablation induced mass spectrometry etc. [8, 14-18]. It allows for substantial reduction of exposure times of the photoresists. Moreover, it provides the ability to ablate the resist in a single laser shot. In microscopy and holography, it provides for bright

illumination which in turn allows to record images (and holograms) in a single laser shot [19, 20]. The CDL emits light at a wavelength $\lambda=46.9\text{nm}$. This wavelength corresponds to the transition $3p-3s J0 - 1$ in an excited neon-like argon ion. [1, 21, 22]. A simplified energy level diagram of the CDL transition at 46.9nm is shown on the Figure 2-1. The upper laser level is populated by electron impact excitation producing a population inversion between the $2p^53p$ and the $2p^53s$ atomic levels. The population inversion is achieved by rapid excitation of the upper level and by a fast relaxation of the lower laser level due to radiative decay to the Ar^{+8} ground level. The electrical pumping is realized by discharging a fast current pulse through a ceramic capillary filled with argon. The current pulse is supplied from Marx generator which charges a liquid dielectric capacitor that in turn discharges through a low inductance discharge circuit.

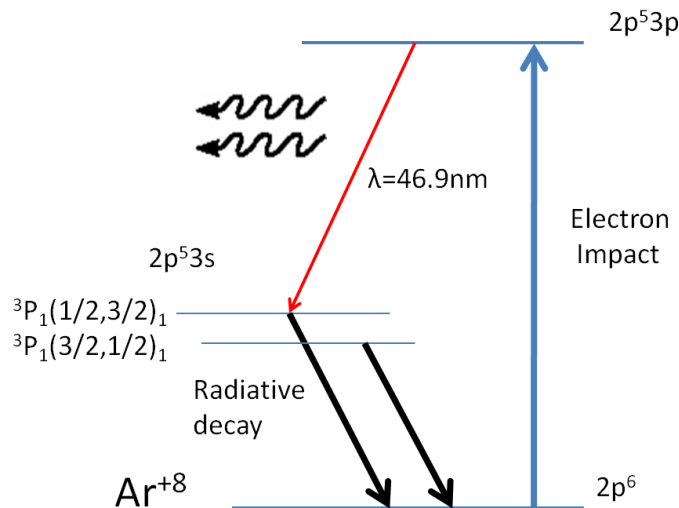


Figure 2-1. Schematically shown simplified Grotrian diagram of the Ne-like Ar CDL.

A schematic of the charging circuit with a liquid dielectric capacitor is shown in the Figure 2-2. The charge accumulated in the capacitor discharges through a circuit with the capillary channel. The current rise time is typically 44ns .

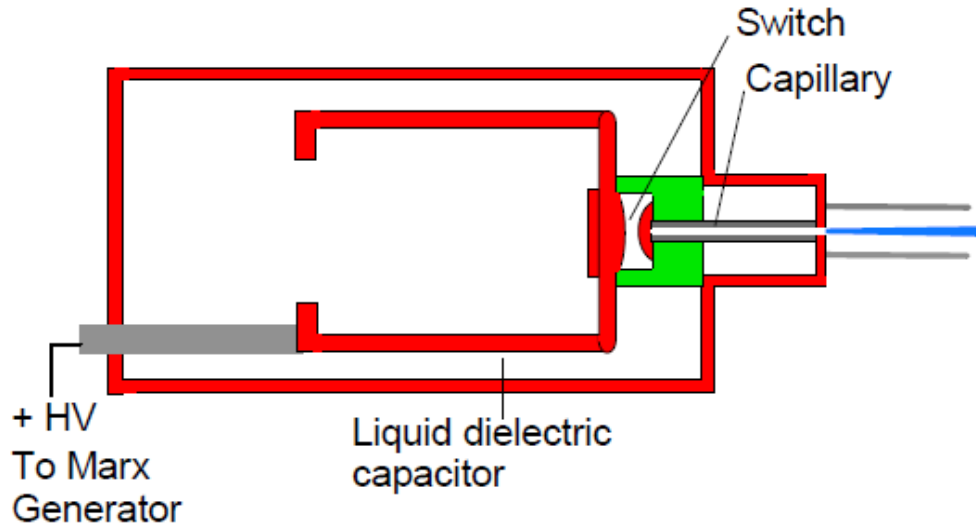


Figure 2-2. Schematic of the capillary discharge laser.

The fast current discharge allows for effective pumping of the laser upper level. The value of the current rise-time is also important from the point of view of the capillary lifetime. Namely, the amount of capillary material which is being ablated off its walls is proportional to the current rise time. Therefore faster discharges are more favorable [23-25].

The plasma contained in the capillary forms a column, which undergoes a compression due to Lorenz force that acts radially on the column compressing it towards the center. The situation is schematically shown in the Figure 2-3.

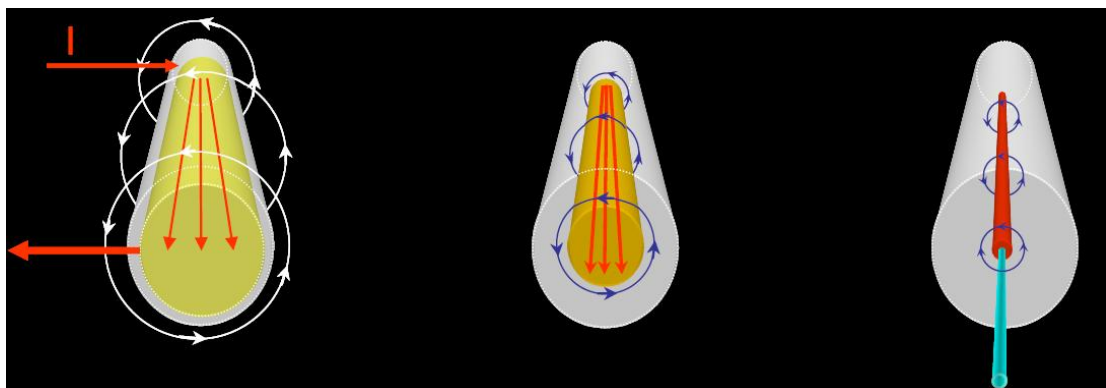


Figure 2-3. Forming of a plasma column in the capillary discharge laser shown schematically.

The diameter of the gas filled capillary at $t=0$ is $\sim 3\text{-}4\text{mm}$. After the pinch the column compresses down to $\sim 300\mu\text{m}$. Diagnostics and modeling [23-25] confirmed that the plasma of these fast capillary discharges is a dynamic and inhomogeneous column, that rapidly contracts, heats up, and expands [27]. The optimum conditions for lasing are established several nanoseconds after the shock wave created by the electromagnetic force reaches the capillary axis. The electron temperature at $\sim 90\text{eV}$, the ion temperature at $\sim 90\text{eV}$, and electron density at $\sim 1.8 \times 10^{18} \text{ cm}^{-3}$ are the typical conditions met in the plasma column [26]. They favor amplification of the 46.9nm line.

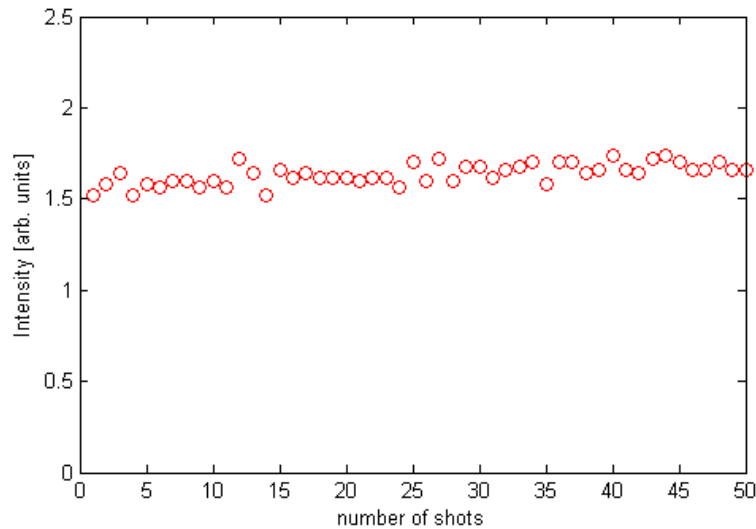


Figure 2-4. CDL output stability. Laser operated at 2Hz repetition rate.

In the Figure 2-4, the CDL's output stability has been measured. The laser was operated at the repetition rate of 2 Hz for the time period of 25 seconds. The laser output was monitored with a photodetector. The peak values of the measured output are plotted as a function of the number of shots.

The gain coefficient measured in the initial setup with a capillary 4 mm in diameter and up to 12cm in length reported in [1] was $gl=7.2$. The absolute value of the average power of the CDL has been characterized in [3]. The measured value of the average power in that case was 0.88 mJ with a deviation of 0.06 mJ.

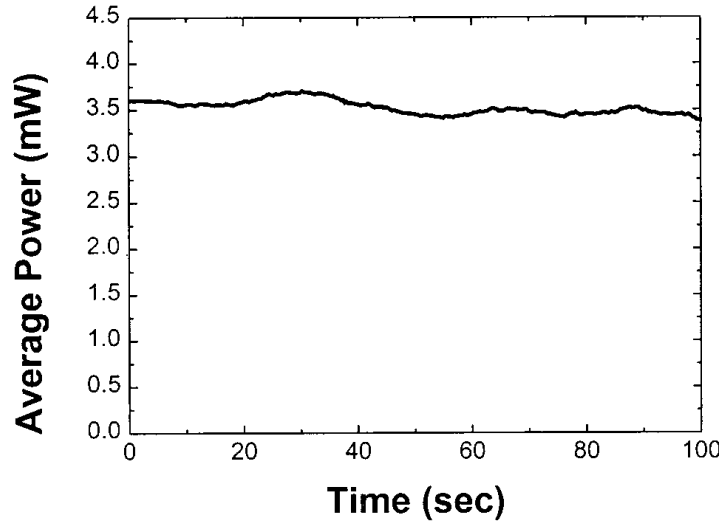


Figure 2-5. The measured average power of the CDL output. The plot is adopted from reference [3].

The CDL's output repeatability is within ~8% of the intensity average value. The laser was operated at 4 Hz repetition rate. The value of the average power shown in the Figure 2-5 was calculated as the moving average of 60 contiguous laser pulses [3]. The typical repetition rate of the CDL operation for applications such as nanofabrication is set at 1 Hz.

The spatial distribution of the CDL beam has an annular shape characterized by ~5mrad divergence angle. This is caused by the anti-guiding effect. Beam antiguiding is due to electron density gradient present across the plasma column. The electron density gradient has its peak value at the center of the plasma column. The refractive index of the plasma is given by the following relation:

$$\eta = \sqrt{1 - \frac{n_e}{n_{ec}}} \quad (1)$$

where: n_e is the electron density, n_{ec} is the critical electron density.

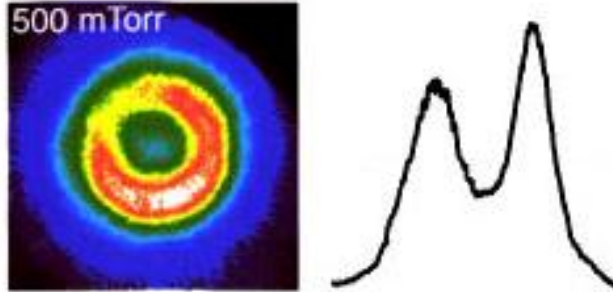


Figure 2-6. The spatial beam profile of the CDL in the far field (left) with a lineout (right). The label 500mTorr indicates the value of the pressure of the Ar gas in the capillary. Figure adopted from [27].

Owing to the refraction, the light propagating through the plasma with lower index of refraction is being refracted to the region of higher refraction index and consequently, is refracted outwards the column. A picture of the typical CDL beam profile with corresponding lineout from the reference [27] are shown in the Figure 2-6.

2.3 SPATIAL COHERENCE OF THE CDL

The degree of spatial coherence plays a critical role in many applications such as interferometry, lithography, and holography. In all applications involving focused light, such as microscopy, Fourier holography the spatial coherence defines the minimum attainable focal spot size [28]. In applications such as holography, holographic microscopy or holographic lithography, the degree

of spatial coherence defines the contrast in the reconstructed hologram [7, 20, 29]. In interferometry, the coherence defines the fringe contrast of the interferogram [4].

The following section describes the experiments that have been carried out in the past in order to measure the CDL's spatial coherence. The first observation of the spatial coherence buildup with the amplifier length in CDL was reported in [30]. The dependence of the spatial coherence as a function of the capillary length and its variation across the beam had been measured. In the experiment from the reference [30], the authors have illuminated a sharp edge with the light emanating from the CDL equipped with capillaries at different lengths. Subsequently, they have measured the ringing effect that occurred downstream the knife edge due to diffraction. The measurements were taken with a CCD device and afterwards compared with model calculations. The spatial coherence monotonic buildup has been observed with increasing capillary length. The experimental results presented in [30] were in good agreement with numerical simulations.

In another experiment, reported in the reference [31], the degree of the spatial coherence was measured using the Young's interferometer. Similarly to the reference [30], the measurements of the degree of spatial coherence were carried out as function of the capillary (or amplifier) length.

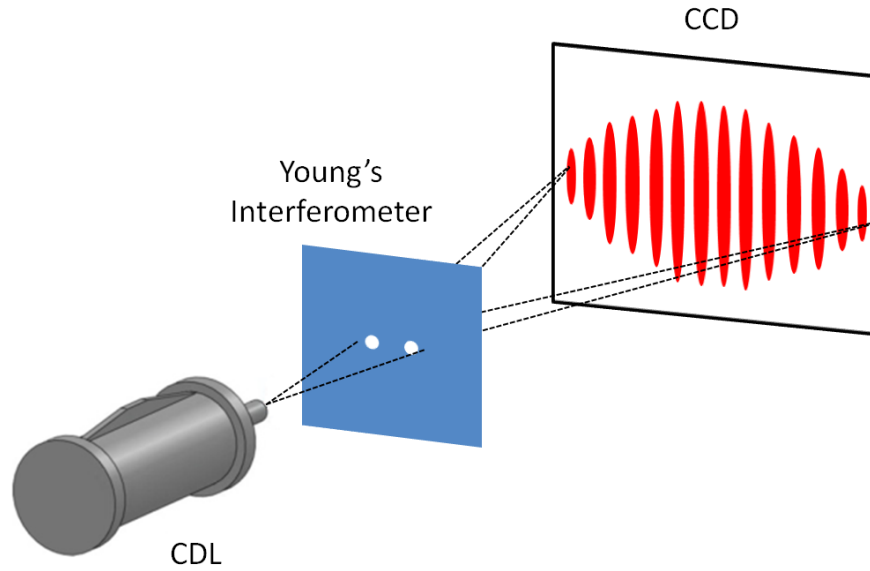


Figure 2-7. A schematic for measurement of spatial coherence using Young's interferometer. Illustration adopted from [31].

The Young's interferometer had a form of a 12.5 μm thick stainless steel shim with two precisely drilled pinholes. Each pinhole measured 10 μm in diameter. The pinholes separation varied in the experiment. As shown schematically on the Figure 2-7, the CDL was illuminating the screen with the pinholes. The resulting interference pattern was recorded on a CCD device. The contrast (or fringe visibility) was measured on the interferograms obtained. The fringe visibility was defined as:

$$V = \frac{I_{\max} - I_{\min}}{I_{\max} + I_{\min}} \quad (2)$$

where: I_{max} and I_{min} are the maximum and minimum intensities obtained from the interferogram. The value of the fringe visibility is proportional to the degree of spatial coherence $|\mu_{12}|$ [32]. To calculate the degree of spatial coherence, the fringe visibility was measured as a function of pinhole separation. The visibility was measured for two different pinhole separations: $300\mu\text{m}$ and $680\mu\text{m}$. The best fit was calculated using the following relation:

$$|\mu_{12}(\Delta x)| = \exp\left[-\frac{\Delta x^2}{2R_C^2}\right] \quad (3)$$

Where the R_C is the coherence radius and Δx is the pinholes separation [ibid.].

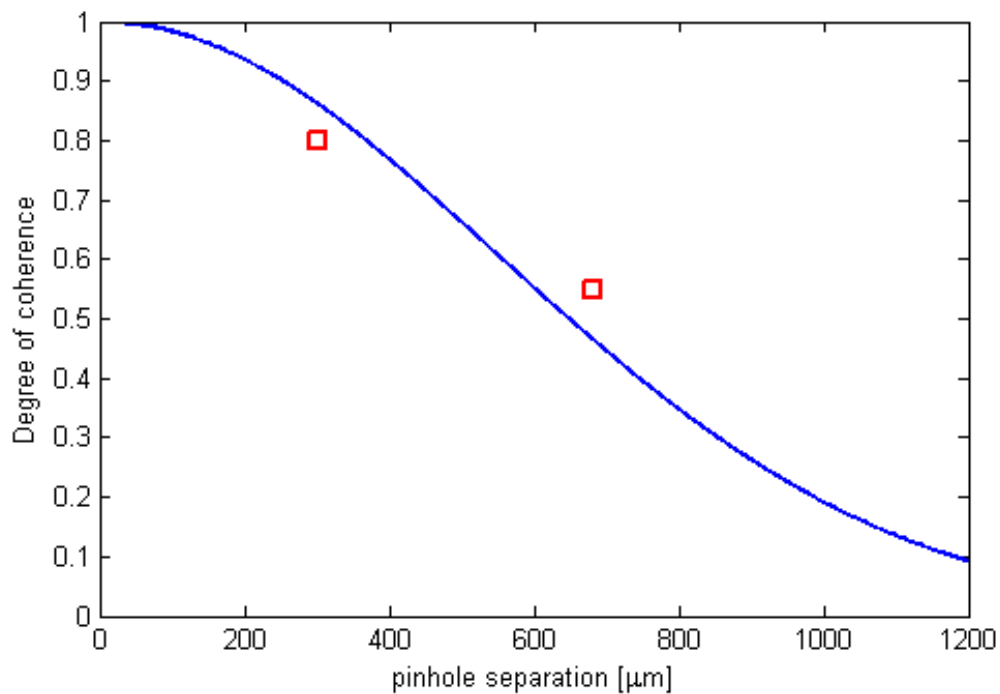


Figure 2-8. The measured degree of coherence (red squares) with calculated fit (solid blue line) [31].

From the fit, the coherence radius was estimated to be $550\mu\text{m}$ at the distance of 15.7cm from the capillary exit. The spatial coherence was also measured as a function of the amplifier length. The laser light obtained from capillaries 18, 27 and 36 cm in length was examined for the degree of coherence. The results are shown in the Figure 2-9. As already shown in [30], the degree of spatial coherence is building up as the gain medium length is being increased. In the Figure 2-9, three interferograms along with corresponding lineouts are shown. Frames a, b and c correspond to capillaries 18, 27 and 36 cm in length respectively. The effect of the increasing degree of spatial coherence is observed in the growing modulation depth of the interference fringes.

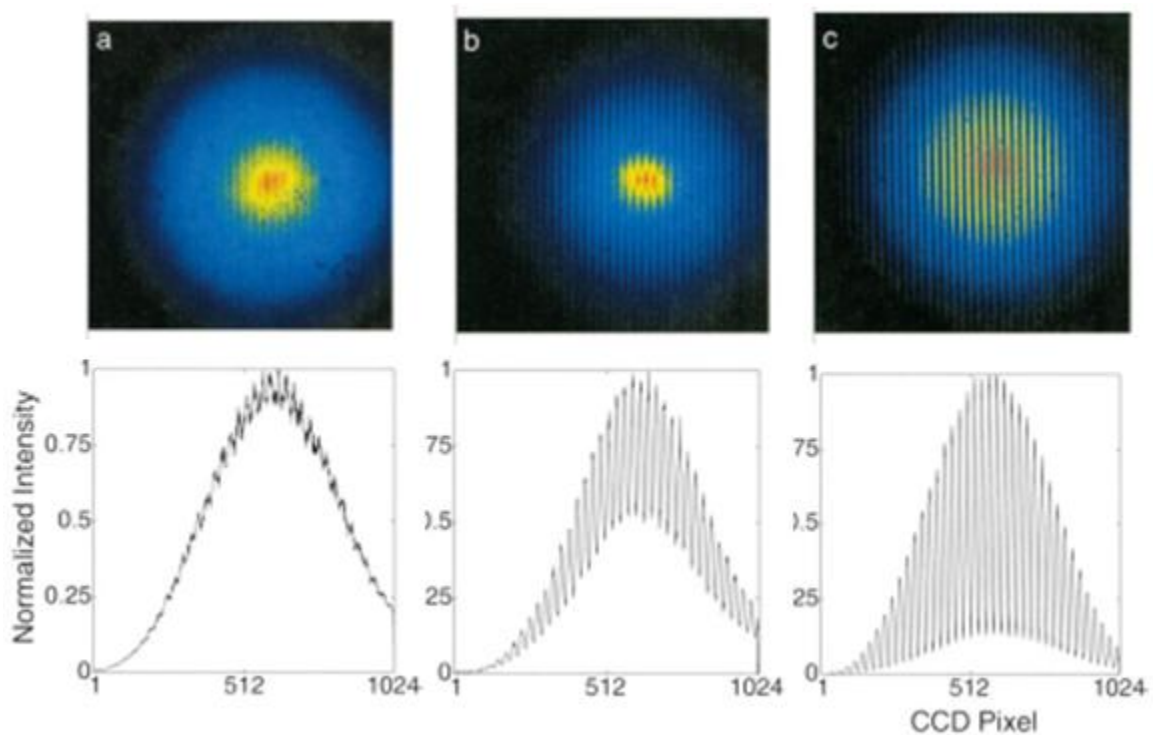


Figure 2-9. Young's interferograms obtained with varying length of the CDL's active medium. Frames to the left show corresponding line-outs. Frames a, b and c correspond to 18, 27 and 36 cm capillary length respectively. Illustration adopted from reference [31].

The results presented in [30, 31] show that the CDL's degree of spatial coherence increases with the amplifier length. The results of the experimental work presented in the references [30, 31] set the operating conditions of the CDL in terms of the capillary length and the distance, at which the experiment ought to be set up.

2.4 TEMPORAL COHERENCE OF THE CDL

Another crucial property of the illumination from the point of view of its potential applicability to nanofabrication is its temporal coherence. In the case of the CDL, the spectral linewidth and the temporal coherence remained to be characterized until recently [26]. Besides the practical interest in knowing the temporal coherence of the CDL for applications, the measurement of the linewidth behavior as a function of plasma column length is also of significant interest for fundamental reasons [33]. The conditions met in the plasma column offer the opportunity to study the gain saturation behavior of a highly inhomogeneous line. This highly inhomogeneous line profile could be expected to lead to the observation of saturation rebroadening of the line not observed in previous studies of line amplification in soft-x-ray plasma amplifiers [33]. The relatively low electron density and moderate ion temperature that characterizes the CDL also gives origin to a small linewidth that is further narrowed in the amplification process. This results in a very narrow laser line that is difficult to measure because its width is below the resolution of most existing spectrometers at this wavelength. The variation of the linewidth as a function of the amplifier length was measured for lengths between 18 and 36 cm. The measurements were conducted using a wavefront division interferometer specifically designed to measure the temporal coherence of soft-x-ray sources [38]. This interferometer was previously used to investigate other types of collisional soft-x-ray lasers, including a 32.8-nm injection-seeded optical-field-ionization soft-x-ray laser in a Xe gas medium [34] and injection-seeded and

self-seeded transient collisional soft-x-ray lasers in the 18.9-nm line of Ni-like Mo in plasmas created by laser irradiation of solid targets [37]. The interferometer consisted of two dihedron mirrors, slightly tilted towards each other, similar as in the Fresnel interferometer. Dihedron shape of mirrors ensures that the measurement is taken in the same part of the illuminating beam.

The light from the CDL illuminated the dihedron pair at 6° incidence angle. The laser beam was split into two parts which underwent reflection from the mirrors and were brought to interference at the CCD detector plane. A back thinned CCD detector was tilted at an angle of 35° relative to the interferometer axis. This relative tilt helped to improve the spatial resolution of the interferograms.

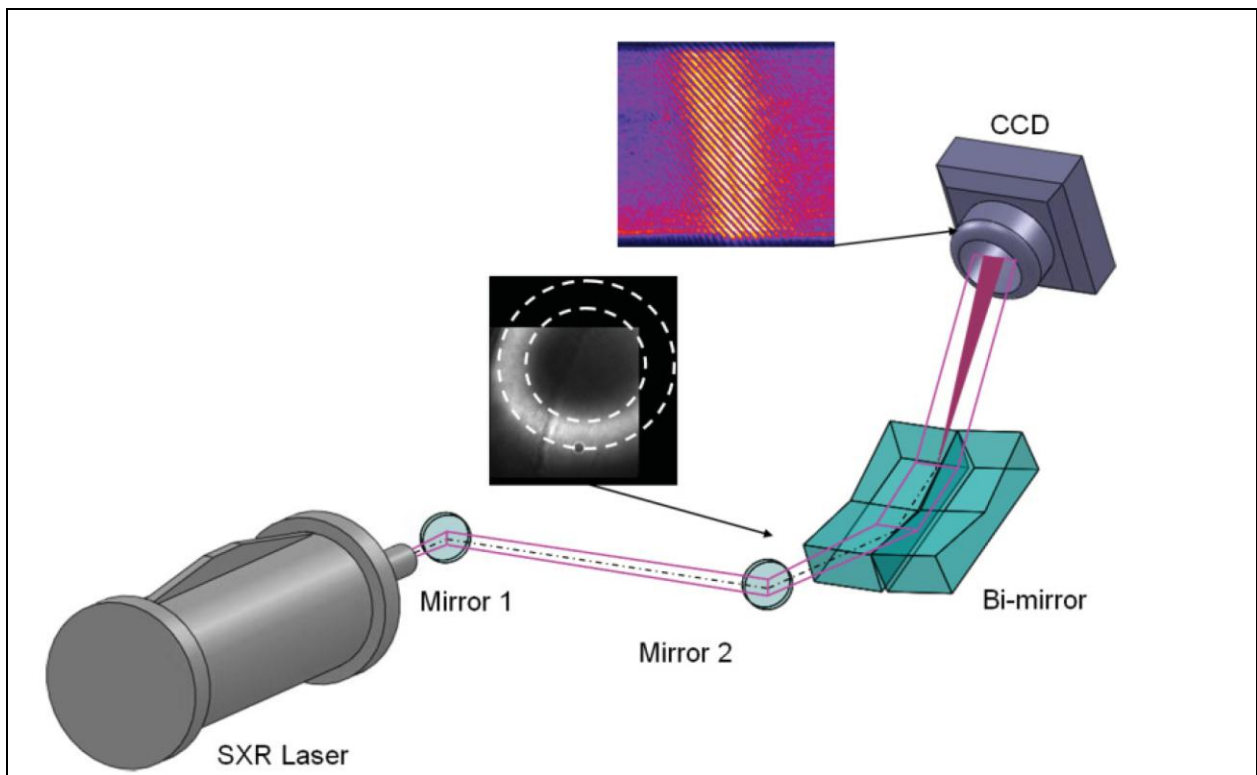


Figure 2-10. Schematic representation of the experimental set up. The output of the CDL is aligned with the axis of the bimirror interferometer using two multilayer mirrors that also contribute to filter off-band plasma radiation. The wave-front-division interferometer produces two beams that interfere onto a CCD.

The inset shows the doughnut shape of the far-field profile of the laser beam recorded using a CCD. The size of the detector did not allow the recording of the entire beam.

One of the dihedron was mounted on a precision translation stage that allowed introducing a controlled optical path difference into one part of the interfering wavefronts. The change in the optical path difference produced a modification of the contrast of the interference fringes. A more detailed description of the instrument can be found in reference [26]. The line profile was inferred from the measurements of the fringe visibility as a function of path difference in the interferometer called the visibility curves. The experimental setup used to measure the temporal coherence is schematically shown on the Figure 2 10.

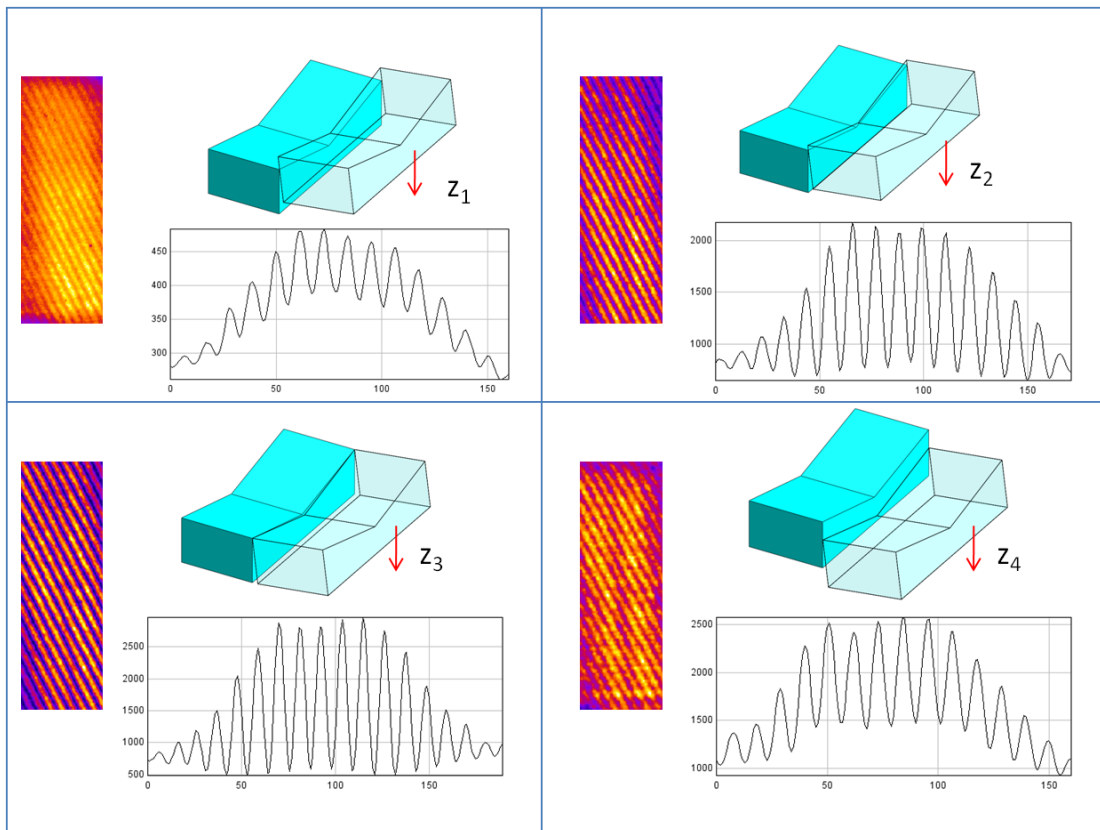


Figure 2-11. Different position of the scanning mirror resulting in different interference contrast. Insets showing relative mirror placement, interferogram and a corresponding line-out.

The optical path difference between the arms of the interferometer can be varied displacing one of the bi-mirrors in the vertical direction, as schematically shown in Figure 2-11. Different frames in the Figure 2-11 show sections of the interferogram with corresponding lineouts and schematically the bi-mirror interferometer with the mobile dihedron mirror displaced by distance indicated with z_n .

The CDL illuminates a Fresnel bi-mirror interferometer after reflecting from a pair of multilayer mirrors (Sc/SiO), with peak reflectivity at 46.9nm and 45° incidence angle. This arrangement serves in the experiment twofold. First, it allows aligning the laser beam with the optical axis of the interferometer. Second, due to the narrow reflectivity bandwidth of the multilayers, the double reflection provides extra spectral filtering at the laser wavelength. The wavefront is split at the interferometer and brought to interference at the detector plane (CCD).

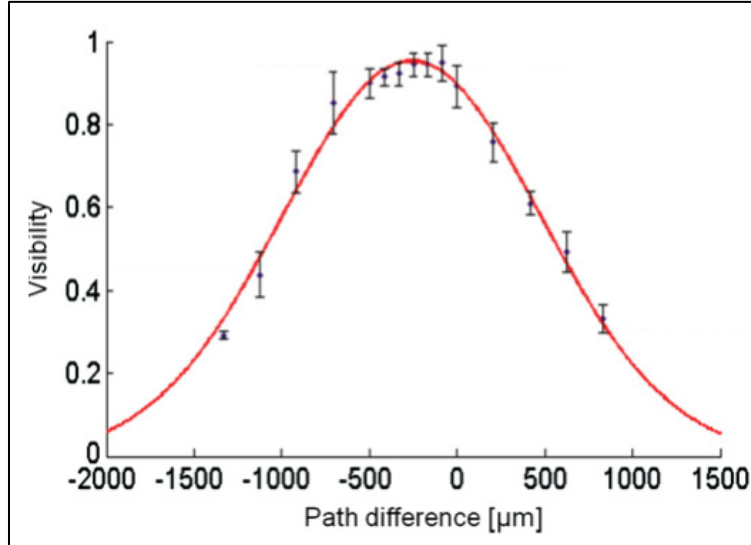


Figure 2-12. Visibility curve obtained for a single capillary length. Experimental data is accompanied by a calculated fit.

The vertical displacement of one mirror produces a change in the visibility of the interference fringes. Varying the path differences allows for the construction of the visibility curve, shown in Figure 2-12. The coherence length is obtained from the optical path difference at which the value of the Gaussian fit drops to 1/e of its maximum. From this measurement the linewidth is calculated. The results of the linewidth measurement are illustrated in the

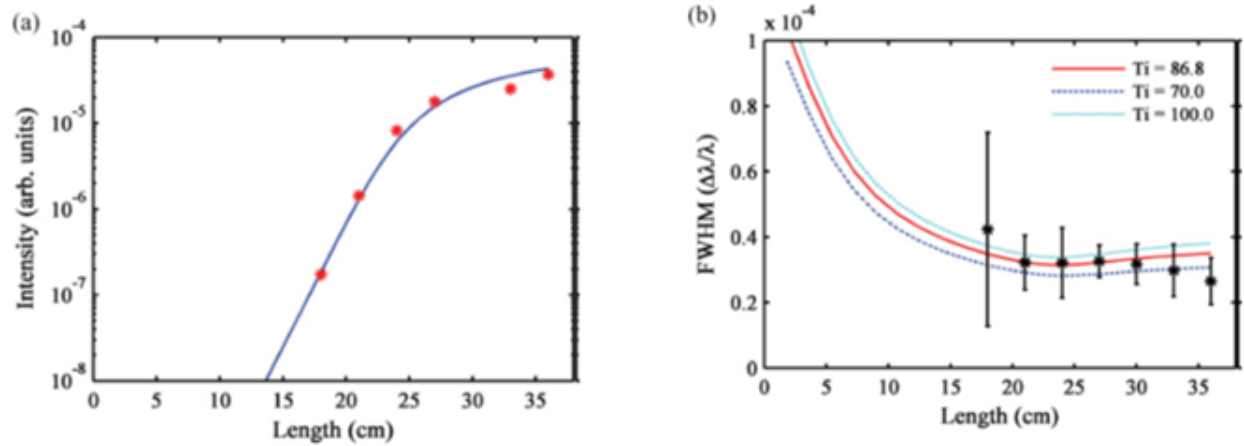


Figure 2-13. In the frame 2-13a the CDL saturation curve is shown.

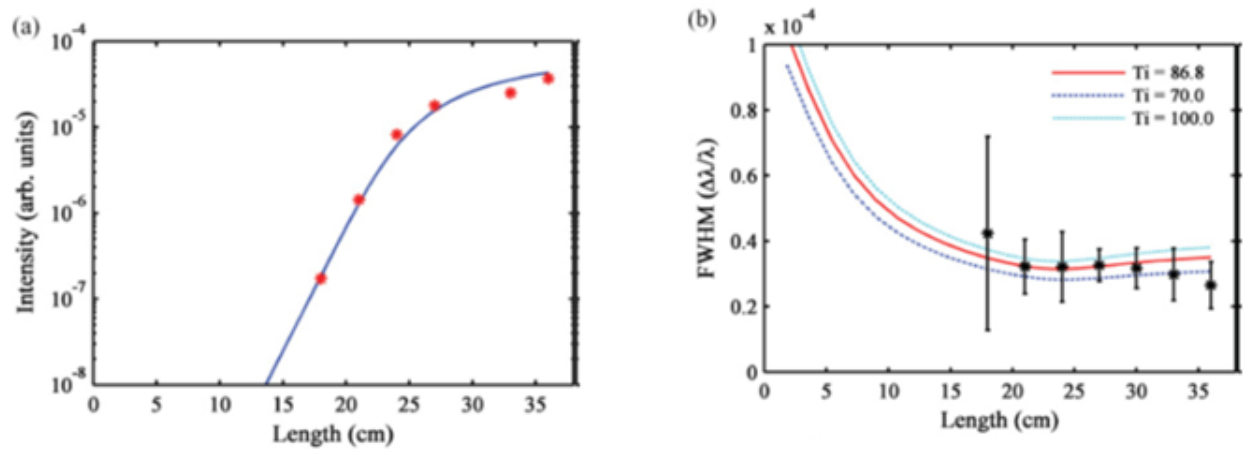


Figure 2-13. (a) Measured laser output intensity as a function of capillary discharge plasma column length. Gain saturation is observed to occur for a plasma column length of ~24 cm. (b) Measured laser linewidth as a function of discharge plasma column length.

As shown on the

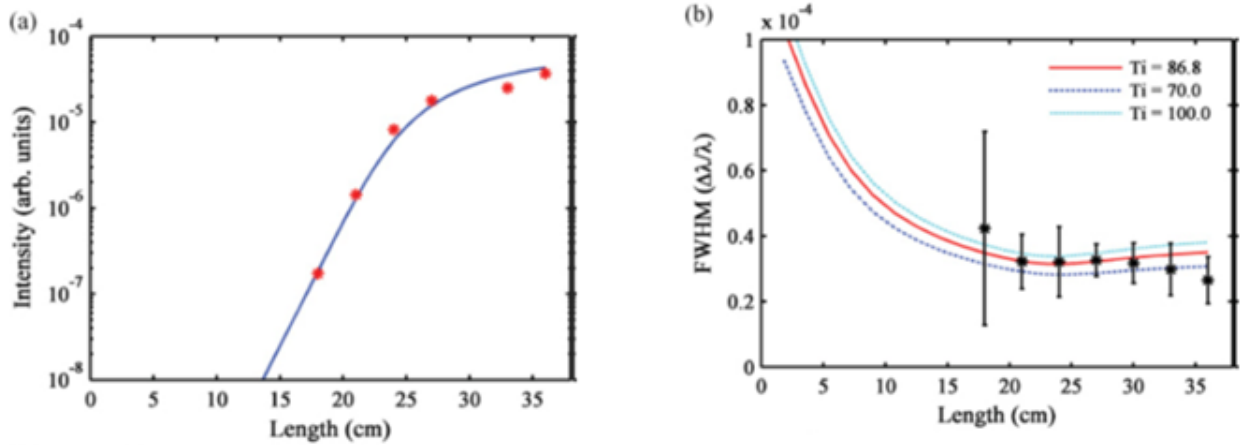


Figure 2-13b, the bandwidth decreases slowly as the plasma length increases maintaining almost constant value for long capillaries, without any significant rebroadening for the longest capillaries even though the laser was operated above saturation. This measured linewidth was ~ 16.6 mÅ, or $\Delta\lambda/\lambda = \sim 3.5 \times 10^{-5}$. Each experimental data point in Figure 2-12b corresponds to an average of 5 measurements and the error bars were selected to include all measurements. The lines show the computed linewidth assuming ion temperatures of 100, 87 and 70eV from top to bottom, respectively. The model simulates the amplification of the laser line by solving the frequency-dependent intensity and population equations accounting for Doppler and collisional broadening, gain saturation, beam refraction, and collisional redistribution. The calculations predict a weak rebroadening of the line beyond $L=24$ cm. However this effect is small compared to our experimental error bars, and no conclusive rebroadening can be derived from the experimental data. However, from the point of view of the CDL's applicability to nanopatterning, it is clear that in order to extract high intensity coherent light one should use capillaries at lengths of 27cm and above.

2.5 SUMMARY

To summarize, in this chapter, three properties crucial from the point of view of potential application of the CDL to nanofabrication have been described: the high average power, the spatial coherence and the temporal coherence. These three parameters facilitate the nanoscale printing with the CDL laser. In the applications described in the chapters 4-7, these properties set the limits on the patterning conditions, printing quality, the extent of printing area and overall method's applicability. The CDL is the only EUV tabletop laser available which is capable to provide with high average power illumination that is sufficiently coherent for nanoscale printing.

2.6 REFERENCES

- [1] *Demonstration of a discharge pumped table-top soft-x-ray laser*, J. J. Rocca, V. Shlyaptsev, F. G. Tomasel, O. D. Cortázar, D. Hartshorn, and J. L. A. Chilla, *Phys. Rev. Lett.* **73**, 2192 (1994).
- [2] *Demonstration of a high average power tabletop soft x-ray laser*, B. R. Benware, C. D. Macchietto, C. H. Moreno, and J. J. Rocca, *Phys. Rev. Lett.* **81**, 5804 (1998).
- [3] *Generation of millijoule-level soft-x-ray laser pulses at a 4-hz repetition rate in a highly saturated tabletop capillary discharge amplifier*, C. D. Macchietto, B. R. Benware, and J. J. Rocca, *Opt. Lett.* **24**, 1115 (1999).
- [4] *Dense plasma diagnostics with an amplitude-division soft-x-ray laser interferometer based on diffraction gratings*, J. Filevich, K. Kanizay, M. C. Marconi, J. L. A. Chilla, and J. J. Rocca, *Opt. Lett.* **25**, 356 (2000).
- [5] *Single-shot extreme ultraviolet laser imaging of nanostructures with wavelength resolution*, C.A. Brewer, F. Brizuela, P. Wachulak, D.H. Martz, W. Chao, E.H. Anderson, D.T. Attwood, A.V. Vinogradov, I.A. Artyukov, A.G. Ponomareko, V.V. Kondratenko, M.C. Marconi, J.J. Rocca, and C.S. Menoni, *Opt. Lett.* **33**, 518 (2008).
- [6] *Reflection mode imaging with nanoscale resolution using a compact extreme ultraviolet laser*, F. Brizuela, G. Vaschenko, C. Brewer, M. Grisham, C. Menoni, M. Marconi, J. Rocca, W. Chao, J. Liddle, E. Anderson, D. Attwood, A. Vinogradov, I. Artioukov, Y. Pershyn, and V. Kondratenko, *Opt. Express*, **13**, 3983 (2005).

- [7] *Soft x-ray laser holography with wavelength resolution*, P. W. Wachulak, M. C. Marconi, R. A. Bartels, C. S. Menoni, and J. J. Rocca, *J. Opt. Soc. Am. B*, **25**, 1811 (2008).
- [8] *Patterning of nano-scale arrays by table-top extreme ultraviolet laser interferometric lithography*, P. W. Wachulak, M. G. Capeluto, M. C. Marconi, C. S. Menoni, and J. J. Rocca, *Opt. Express*, **15**, 3465 (2007).
- [9] *Fabrication of metallic micropatterns using table top extreme ultraviolet laser interferometric lithography*, L. Ottaviano, F. Bussolotti, S. Piperno, M. Rinaldi, S. Santucci, F. Flora, L. Mezi, P. Dunne, J. Kaiser, A. Reale, A. Ritucci, and P. Zuppella, *Plasma Sources Science and Technology*, **17**, 024019 (2008).
- [10] *Nanometer-scale ablation with a table-top soft x-ray laser*, G. Vaschenko, A. Garcia Etxarri, C. S. Menoni, J. J. Rocca, O. Hemberg, S. Bloom, W. Chao, E. H. Anderson, D. T. Attwood, Y. Lu, and B. Parkinson, *Opt. Lett.* **31**, 3615 (2006).
- [11] *Ablation of organic polymers by 46.9-nm-laser radiation*, L. Juha, M. Bittner, D. Chvostova, J. Krasa, Z. Otcenasek, A. R. Präg, J. Ullschmied, Z. Pientka, J. Krzywinski, J. B. Pelka, A. Wawro, M. E. Grisham, G. Vaschenko, C. S. Menoni, and J. J. Rocca, *Appl. Phys. Lett.* **86**, 034109 (2005).
- [12] *Single photon ionization of hydrogen bonded clusters with a soft x-ray laser: HCOOH_x and $\text{HCOOH}_y(\text{H}_2\text{O})_z$* , S. Heinbuch, F. Dong, J. J. Rocca, and E. R. Bernstein. *The Journal of Chemical Physics*, **126**, 244301 (2007).
- [13] *Determination of XUV optical constants by reflectometry using a high-repetition rate 46.9-nm laser*, I.A. Artioukov, B.R. Benware, J.J. Rocca, M. Forsythe, Yu.A. Uspenskii,

- and A.V. Vinogradov, *Selected Topics in Quantum Electronics, IEEE Journal of*, **5**, 1495 (1999).
- [14] *Defect tolerant extreme ultraviolet nanoscale printing*, L. Urbanski, A. Isoyan, A. Stein, J.J. Rocca, C.S. Menoni and M.C. Marconi, *Opt. Lett.* **37**, 3633 (2012).
- [15] *Nano-scale ablation with a compact extreme ultraviolet laser*, C. S. Menoni, G. Vaschenko, H. Bravo, F. Brizuela, J. J. Rocca, W. Chao, E. H. Anderson, D. T. Attwood, O. Hemberg, B. Frazer, and S. Bloom, *Lasers and Electro-Optics Society, LEOS 2006. 19th Annual Meeting of the IEEE*, 953 (2006).
- [16] *Analysis of a scheme for de-magnified talbot lithography*, L. Urbanski, M. C. Marconi, A. Isoyan, A. Stein, C. S. Menoni, and J. J. Rocca, *J. Vac. Sci. Technol. B*, **29**, 06F504 (2011).
- [17] *Talbot lithography: Self-imaging of complex structures*, A. Isoyan, F. Jiang, Y. C. Cheng, F. Cerrina, P. Wachulak, L. Urbanski, J. Rocca, C. Menoni, and M. Marconi, *J. Vac. Sci. Technol. B*, **27**, 2931 (2009).
- [18] *Soft x-ray laser ablation mass spectrometry depth profiling with nanoscale resolution*, I. Kuznetsov, J. Filevich, F. Dong, M. Woolston, E.R. Bernstein, W. Circk D.D. Chao, E.H. Anderson, J.J. Rocca, and C.S. Menoni, *Private Communication* 2011.
- [19] *Sequential single-shot imaging of nanoscale dynamic interactions with a table-top soft x-ray laser*, S. Carbajo, I. D. Howlett, F. Brizuela, K. S. Buchanan, M. C. Marconi, W. Chao, E. H. Anderson, I. Artioukov, A. Vinogradov, J. J. Rocca, and C. S. Menoni. . *Opt. Lett.*, **37**, 2994 (2012).

- [20] *Flash EUV holography used to analyze the dynamics of nanoscale material oscillators*, E. Malm, C.G. Brown, N. Monserud, V. Putkaradze, and M.C. Marconi, *Private Communication* (2011).
- [21] *New results in the development of table-top capillary discharge soft x-ray lasers: Demonstration of high average power and realization of the first application*, J.J. Rocca, C.H. Moreno, B.R. Benware, C.D. Macchietto, M.C. Marconi, V.N. Shlyaptsev, F.G. Tomasel, K. Kanizay, J.J. Gonzalez, and M. Frati, *X-RAY LASERS*, **159**, 9 (1999).
- [22] *Discharge-Driven 46.9-Nm Amplifier with Gain-Length Approaching Saturation*, J.J. Rocca, M.C. Marconi, J.L.A. Chilla, D.P. Clark, F.G. Tomasel, and V.N. Shlyaptsev, *IEEE Journal Of Selected Topics In Quantum Electronics*, **1**, 945 (1995).
- [23] *Energy extraction and achievement of the saturation limit in a discharge-pumped table-top soft x-ray amplifier*, J.J. Rocca, D.P. Clark, J.L.A. Chilla, and V.N. Shlyaptsev, *Phys. Rev. Lett.* **77**, 1476 (1996).
- [24] *Discharge-pumped soft-x-ray laser in neon-like argon*, J.J. Rocca, F.G. Tomasel, M.C. Marconi, V.N. Shlyaptsev, J.L.A. Chilla, B.T. Szapiro, and G. Giudice. *Physics Of Plasmas*, **2**, 2547 (1995).
- [25] *Fast-Discharge Excitation Of Hot Capillary Plasmas For Soft-X-Ray Amplifiers*, J.J. Rocca, O.D. Cortazar, B. Szapiro, K. Floyd, and F.G. Tomasel, *Phys. Rev. E*, **47**, 1299 (1993).

- [26] *Spectral linewidth of a Ne-like Ar capillary discharge soft-x-ray laser and its dependence on amplification beyond gain saturation*, L. Urbanski, M. C. Marconi, L. M. Meng, M. Berrill, O. Guilbaud, A. Klisnick, and J. J. Rocca, *Phys. Rev. A*, **85**, 033837 (2012).
- [27] *Two-dimensional near-field and far-field imaging of a Ne-like Ar capillary discharge table-top soft-x-ray laser*, C.H. Moreno, M.C. Marconi, V.N. Shlyaptsev, B.R. Benware, C.D. Macchietto, J.L.A. Chilla, J.J. Rocca, and A.L. Osterheld. *Phys. Rev. A*, **58**, 1509 (1998).
- [28] *Soft X-Rays and Extreme Ultraviolet Radiation Principles and Applications*, D.T. Attwood, Cambridge University Press (2007).
- [29] *Extreme ultraviolet holographic lithography with a table-top laser*, A. Isoyan, F. Jiang, Y.-C. Cheng, P. Wachulak, L. Urbanski, J. Rocca, C. Menoni, M. Marconi, and F. Cerrina, . Proc. SPIE, **7271**, 72713O (2009).
- [30] *Measurement of the spatial coherence buildup in a discharge pumped table-top soft x-ray laser*, M. C. Marconi, J. L. A. Chilla, C. H. Moreno, B. R. Benware, and J. J. Rocca, *Phys. Rev. Lett.*, **79**, 2799 (1997).
- [31] *Achievement of essentially full spatial coherence in a high-average-power soft-x-ray laser*, Y. Liu, M. Seminario, F. G. Tomasel, C. Chang, J. J. Rocca, and D. T. Attwood, *Phys. Rev. A*, **63**, 033802 (2001).
- [32] *Statistical optics*, Joseph W. Goodman. Wiley, 1985.
- [33] *Experimental and theoretical investigation of neonlike selenium x-ray laser spectral linewidths and their variation with amplification*, J.A. Koch, B.J. MacGowan, L.B.

Da Silva, D.L. Matthews, J.H. Underwood, P.J. Batson, R.W. Lee, R.A. London, and S. Mrowka, *Phys. Rev. A*, **50**, 1877 (1994).

- [34] *Experimental study of the temporal coherence and spectral profile of the 13.9nm transient X-ray laser*, A. Klisnick, O. Guilbaud, D. Ros, K. Cassou, S. Kazamias, G. Jamelot, J.-C. Lagron, D. Joyeux, D. Phalippou, Y. Lechantre, M. Edwards, P. Mistry, and G.J. Tallents, *Journal of Quantitative Spectroscopy and Radiative Transfer*, **(1–3)**, 370 (2006).

CHAPTER 3 MASK FABRICATION

3.1 INTRODUCTION

In this chapter the process of the diffractive mask design and fabrication is explained in detail. Moreover, the materials used for the fabrication are reviewed in terms of their applicability for EUV mask production. The chapter is divided into three parts, the first one addresses the properties of materials applied for the mask fabrication. The second part features the mask design and its fabrication protocol. The third part describes the mask fabrication technique, electron beam lithography (EBL). This chapter together with appendix 2 is intended as an instruction manual for the EUV mask fabrication.

Strong resonant absorptions in the EUV region are present in all materials. This fact forces usage of diffractive instead of refractive optics in the EUV region of electromagnetic spectrum [1]. Stringent requirements on the EUV optics (masks) imposed by the properties of the EUV light necessitated application of dedicated materials, specialized design and compound techniques of fabrication. The design of the diffractive masks presented in this thesis, has obviated the possibility of having them fabricated as free standing objects. Consequently, all masks were fabricated on ultrathin supporting membranes. In order to transmit the EUV light efficiently, the materials for the membranes had to be extremely thin. On the other hand, they had to be sturdy enough to bear their own weight. The materials of choice had to enable high transmission of the supporting structure (membrane) and at the same time high opacity of the light blocking elements of the mask. The mask's smallest feature sizes necessitated dedicated fabrication technique. The process of EUV mask design and fabrication imposed many challenges that had

to be addressed. It is a pivotal part of the experimental work presented in this thesis, and will be described in detail in this chapter

3.2 MASK DESIGN

3.2.1 MATERIALS CONSIDERATIONS

The diffractive masks described in this thesis are binary. It means that the mask either absorbs the impinging light or transmits it. The situation most desired in diffractive optics design and fabrication is the maximum contrast between the opaque and transparent elements. In other words, a diffractive mask with a high contrast at $\lambda=46.9$ nm has to have its opaque parts made out of materials highly EUV absorptive, whereas the transparent parts of the mask had to be made out of materials with highest possible EUV transmission.

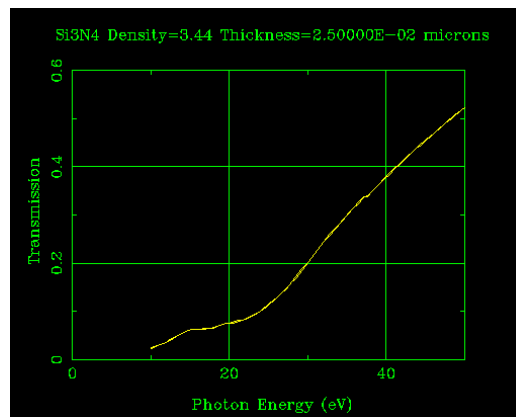


Figure 3-1. Transmission of silicon nitride membrane used for mask support. Calculation carried out at CXRO [6].

The material data base from reference [6] was used to determine the materials best suited for fabrication of a diffractive mask for 46.9 nm wavelength. Making the mask free standing was out of question due to specific mask design. Therefore the mask had to be supported by an ultrathin membrane. Such membrane is expected to provide with high transmission at the EUV wavelengths and concurrently needs to be sturdy enough to support its own weight and the weight of the diffractive mask it is carrying. In addition, a uniform, flat, large area (2.6x2.6mm²) membrane is desired. Most ultra thin membranes tend to dome, which excludes them as potential EUV mask carriers. Slightest (larger than the depth of focus) non-uniformity in the membrane's flatness would cause different parts of the diffractive mask be located at different distances from the sample. This would introduce unwanted phase components to the reconstructing wavefront. As a consequence, parts of the reconstruction would be in focus, whereas some fragments of it would appear blurred.

The requirements on membranes transmission and strength are contradictory. Namely, thinner membranes exhibit higher EUV transmission, yet they can bear less weight. Therefore the membrane fabrication presented a particular challenge. To address this issue specific materials for the membrane had to be selected. Two potential candidates were silicon rich nitride (Si₃N₄) and silicon. Both these materials are EUV transmissive and their processing techniques are well mastered. Some part of the silicon nitride membranes used for mask fabrication was fabricated at CNTech (Center for Nanotechnology at University of Wisconsin-Madison) whereas others were purchased from a commercial vendor (NORCADA). The benefit from using silicon nitride membranes for support of the diffractive mask is twofold. First, thin silicon nitride films (~25 nm) are transparent to EUV/soft X-rays (Figure 3-1). Second, silicon nitride is a low stress material, thus its mechanical properties allow fabricating extremely thin membranes of relatively

large surface area [7]. The optical transmission of a 25nm thick silicon nitride membrane is shown on the Figure 3-1. The EUV transmission of the silicon nitride was calculated using the database from the reference [6]. At the wavelength of interest: 46.9nm (~26eV), the membrane made of silicon nitride has ~13% transmission.

For comparison purposes, a single diffractive mask on a commercial silicon membrane was fabricated. The silicon membrane was ~200 nm thick. The EUV transmission of the silicon membrane was 36% at 46.9nm. Although silicon has better transmission in the EUV than the silicon nitride, its mechanical properties such as inherent tensile stress preclude it from being widely used for large area membranes. There are however reports of successful attempts to use silicon for large area (several mm²) ultrathin (less than 100 nm) membrane fabrication [8].

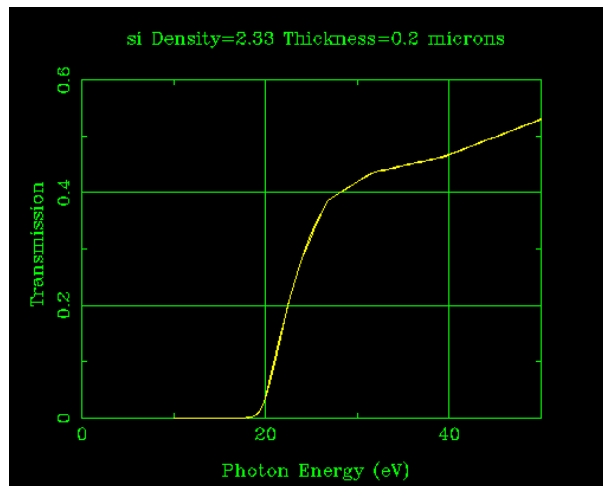


Figure 3-2. Transmission of silicon membrane used for mask support. Calculation carried out at CXRO

[6].

The material comprising the absorptive (dark) elements of the diffractive mask is supposed to block the EUV light efficiently. This time, previously mentioned high opacity of fabrication available materials is in our favor. It turned out that an electron beam cured resist will provide with absorption that is sufficient for effective EUV light blocking. This fact implies that the desired pattern as written on the membrane by means of the EBL and developed will constitute an effective EUV mask. No further processing was required, which simplified the mask fabrication process significantly. The resist of choice was hydrogen silsequioxane (HSQ). This resist allows for fine detail e-beam printing [9]. The e-beam exposed HSQ has the atomic composition similar to silicon dioxide. The transmission of 70nm thick silicon dioxide for ~26eV photons is 1.7%. as it is shown in the graph calculated using CXRO database is shown on the Figure 3-3. Thus the e-beam cured HSQ's transmission is 7.6 times lower for the case of the silicon nitride membrane and 21 times lower in the silicon membrane's case.

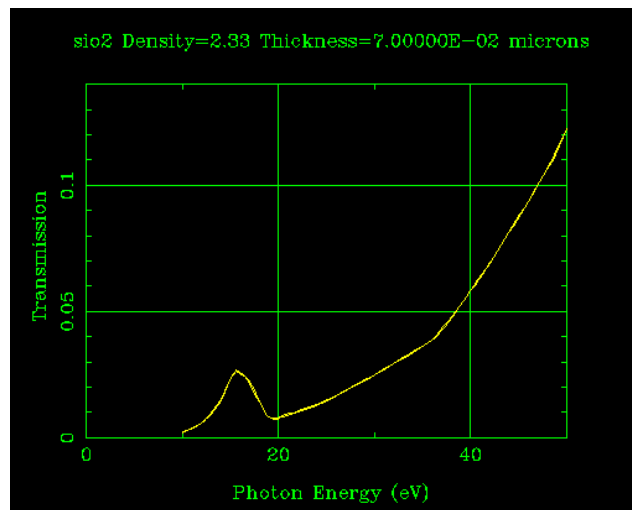


Figure 3-3. Transmission of 70nm thick silicon dioxide (exposed HSQ) used to define opaque parts of diffractive mask [6].

3.2.2 FABRICATION PROTOCOL

The supporting structure for the masks was made of both silicon and silicon nitride membranes. Those materials have ~36% and ~13% transmission for the wavelength of 46.9nm respectively. A schematic of the membrane which carries the mask can be viewed on the Figure 3-4. The membrane is supported by a frame that is made of silicon, typically $500 \pm 10\mu\text{m}$ thick. The frame size is $11 \times 11\text{mm}^2$. The membranes are made of either silicon or silicon nitride. The silicon membranes measured $5 \times 5\text{mm}$ and were 200 nm thick, whereas silicon nitride membranes measured $2.6 \text{ mm} \times 2.6 \text{ mm}$ and were ~25 nm thick. The diffractive mask is defined in a layer of HSQ resist. Depending on the experiment, the mask sizes were from $325 \times 325 \mu\text{m}^2$ to $1000 \times 1000 \mu\text{m}^2$.

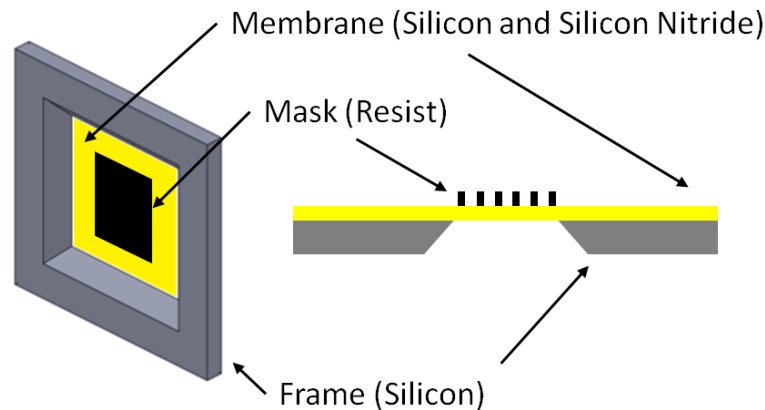


Figure 3-4. Schematic of the diffractive mask design. A silicon or silicon nitride membrane (marked with yellow) spanned on a frame supports a mask defined in HSQ by means of EBL.

Photographs of the silicon nitride membranes used in the experiment can be viewed on the Figure 3-5. The picture in the left illustrates an entire 4 inch wafer with the membranes just

before cleaving. Shown to the right on the Figure 3-5, there is a single chip containing a membrane cleaved.

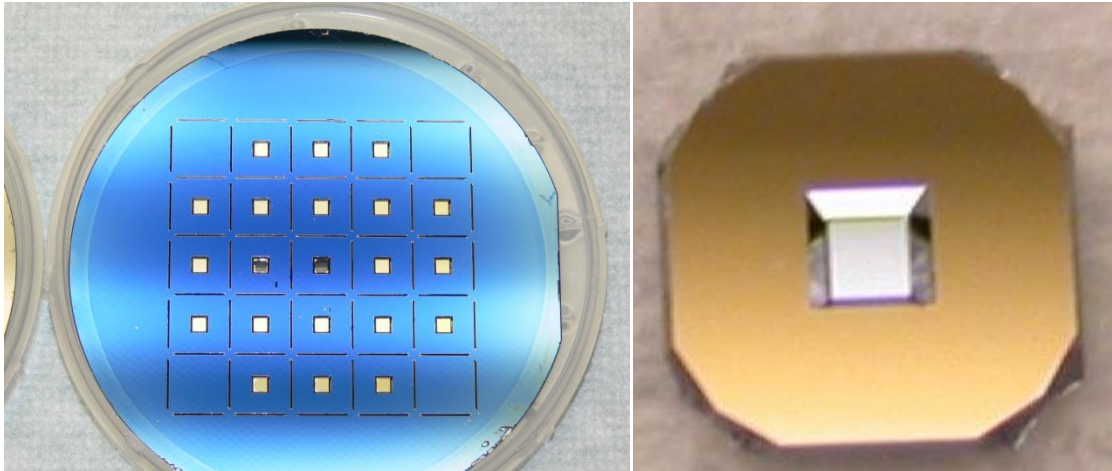


Figure 3-5. Silicon nitride membranes used to support diffractive masks.

In order to prepare the membranes for e-beam writing, they had to be cleaved off from a 4 inch wafer and subsequently rinsed with isopropyl alcohol to remove silicon debris.

Mask fabrication protocol is schematically shown on the Figure 3-6. The frames 1-6 show schematically the stages of the fabrication process. The steps are listed below:

- HSQ spin coat,
- ESPACER spin coat,
- membrane release,
- electron beam lithography,
- developing,
- rinse.

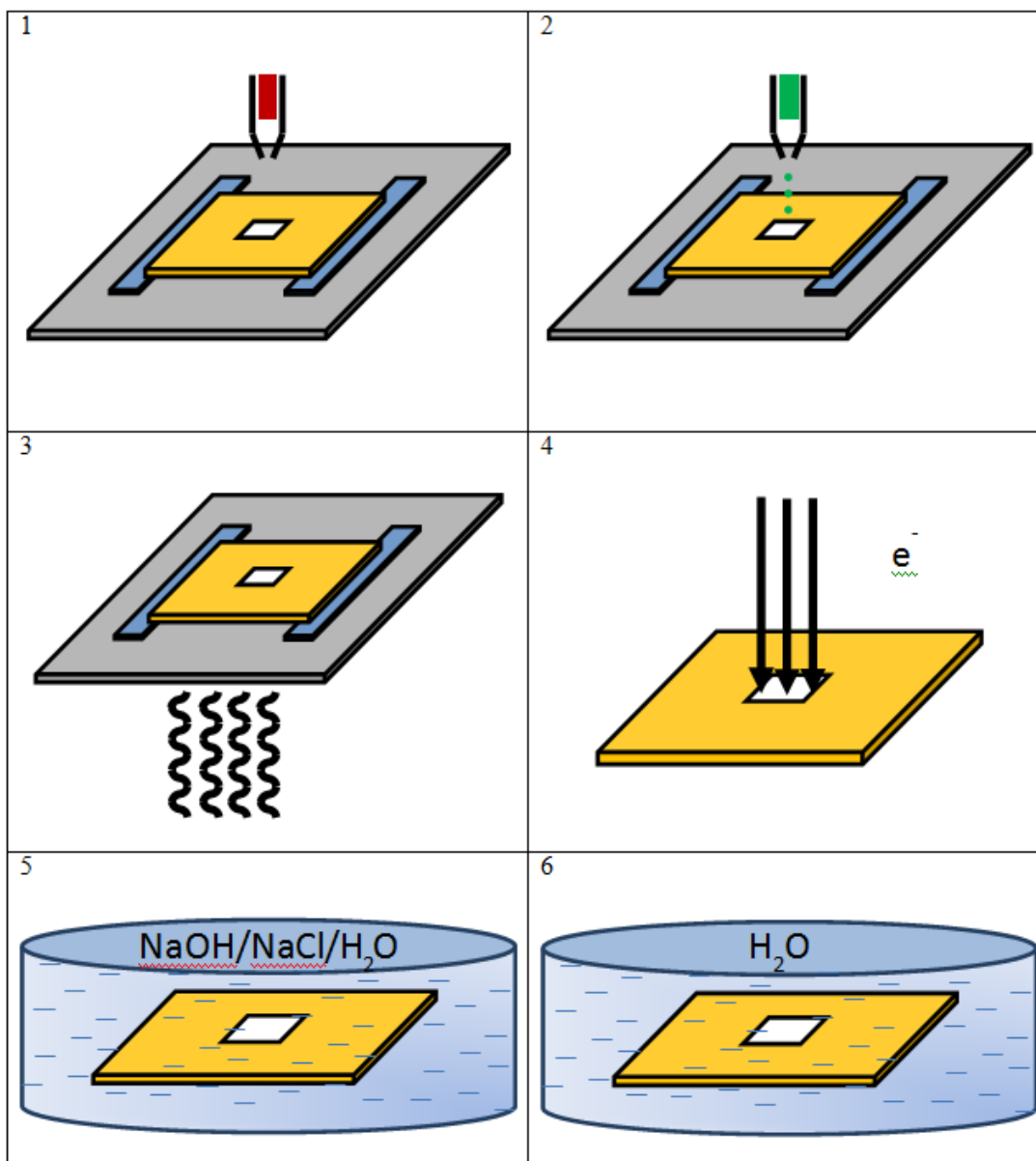


Figure 3-6. Mask fabrication protocol. Frames 1-6 illustrate consecutive fabrication stages.

To facilitate membrane handling for steps 1 and 2 of the mask fabrication protocol, it was mounted on a silicon wafer surface. The mounting was done with strips of thermal release wafer dicing tape (Nitto-Denko 3195M) [5]. The tape had two sides, regular adhesive and thermal

release side. The thermal release was occurring at $\sim 90^\circ$ Celsius. Below the graph of the adhesive strength versus the sheet surface temperature can be viewed.

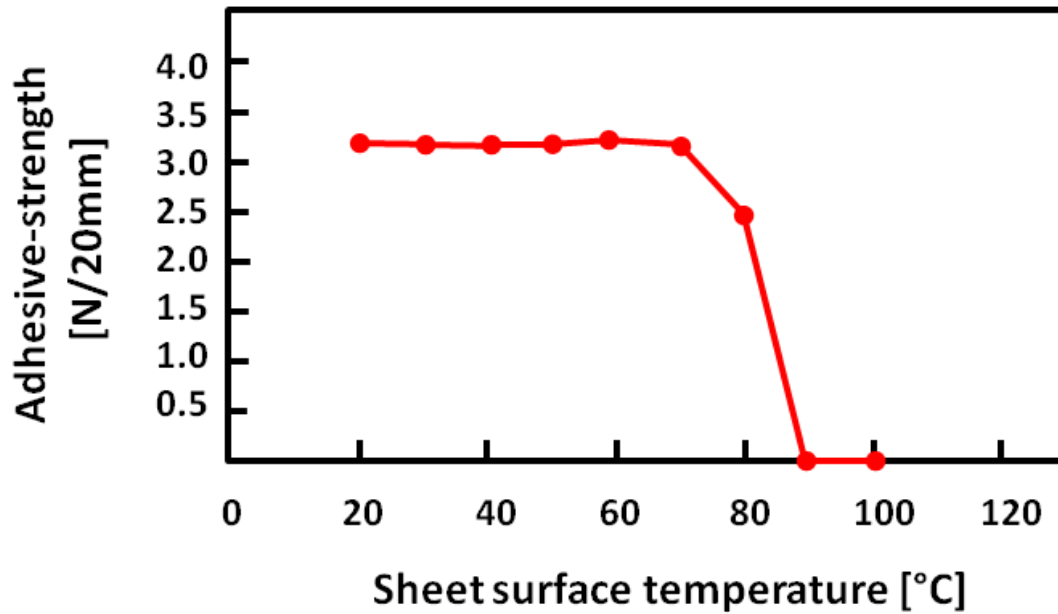


Figure 3-7. Thermal release property of the dicing tape used to mount the membrane. Plot adopted from reference [10].

The tape was oriented the thermal release side up, such that after dismounting, the strips would remain on the carrier silicon wafer and could be discarded along with it.

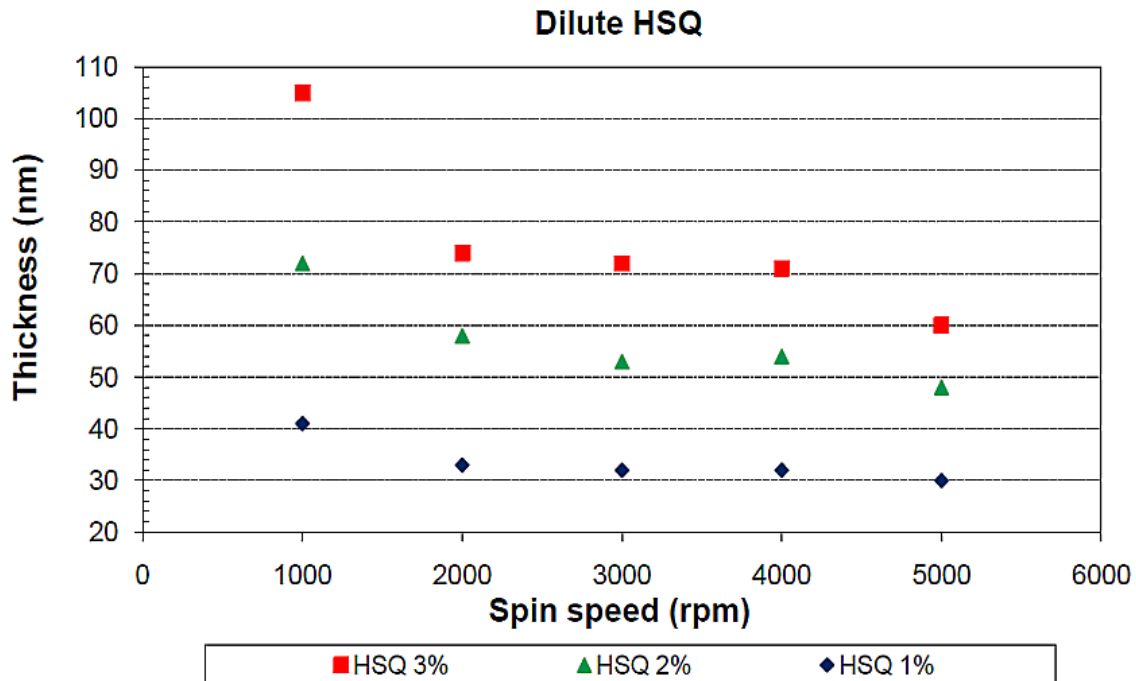


Figure 3-8. Spin curves for HSQ [adopted from http://www.nanofab.ualberta.ca/wp-content/uploads/downloads/2011/04/HSQ_Spin_Curves.pdf]

This pre-mounted membrane was then placed over the vacuum chuck of a spin coater (Carl Suss and Laurel Technologies spin coaters were used interchangeably).

At this stage HSQ resist is applied and spin coated over the membrane. HSQ resist was spun in a single step process, 1min at 1000 rpm. The HSQ resist had 2% concentration in methyl isobutyl ketone (MIBK) solvent. According to the spin curves (Figure 3-8), 1000rpm spin speed should provide a ~70nm thick layer of HSQ. Subsequently (Figure 3-6, frame 2), ESPACER solution was applied at 3000rpm. ESPACER is water-based, electrical charge dissipating material [11]. As such it will not react with the solvent of HSQ (MIBK). ESPACER is designed to drive off any electrical charge accumulated spatially over the writing region.

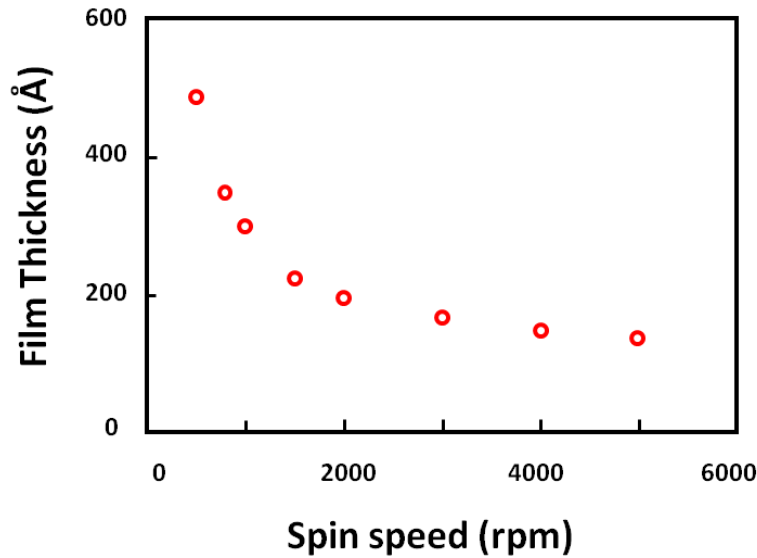


Figure 3-9. Spin curves of water-based ESPACER (Adopted from the manufacturer's specifications [11]).

This alleviates writing defects caused by local beam deflection by the space charge. In our case this is of key importance, because the membrane is made out of dielectric material and the pixel size is extremely small (50 nm). At 3000rpm spin speed, according to the manufacturer (Showa-Denko) a layer thinner than 20nm should be spun (Figure 3 9).

Once removed from the spin coater chuck, the sample was placed over a hotplate for 40 seconds, to provide thermal release for the dicing tape (Figure 3-6, frame 3). A sample prepared along this protocol was subsequently loaded into the electron beam writer and mask was defined in the resist layer. After the exposure (Figure 3-6, frame 4), the sample was developed in aqueous solution of sodium chloride and sodium hydroxide (4%, 1% respectively) for 4 minutes (Figure 3-6, frames 5 and 6, respectively). This concludes the fabrication process. From this point on the membrane can be referred to as the diffractive mask.

3.3 MASK DESIGN

In the EUV nanopatterning experiments, the resolution which the masks provide is governed by their numerical aperture. Consequently, there is a certain depth of focus (DOF) associated with each mask. The value of the DOF determines the area where resolution of the prints is only slightly degraded [1]. The DOFs for the masks used in the experiments presented in this thesis varied between 250nm and 1 μ m. The DOF imposes restrictions on the sample's placement accuracy. The opto-mechanical setup for EUV nanopatterning has been custom designed and machined. The tolerances of the opto-mechanical components and fixtures are expected to be much worse than the error margins in the positioning accuracy dictated by the DOFs of the masks. Therefore, precise placement of the recording plate (sample) with respect to the mask is a challenging task. A viable workaround to alleviate the strict placement restriction is to fabricate several masks in the same membrane that have identical design, yet the working distances of each of them differ by some value. In the cases discussed in this thesis, the artificially embedded defocus value was equal to the DOF of the diffractive masks. The quantity of defocused masks printed on the same membrane varied between 4 and 9. The defocusing can be achieved using various approaches. One of the approaches used in the research presented in this thesis was to calculate several binary masks which reconstruct at different working distances. This specific approach was used for fabrication of the computer generated hologram (chapter 4). Another strategy was to introduce the defocused working distance by changing the pixel size in the design file used by the electron beam lithography tool. Varying the pixel size results in the change of the masks' lateral size. As shown in the chapter 5, the self-imaging distance depends on the mask's period.

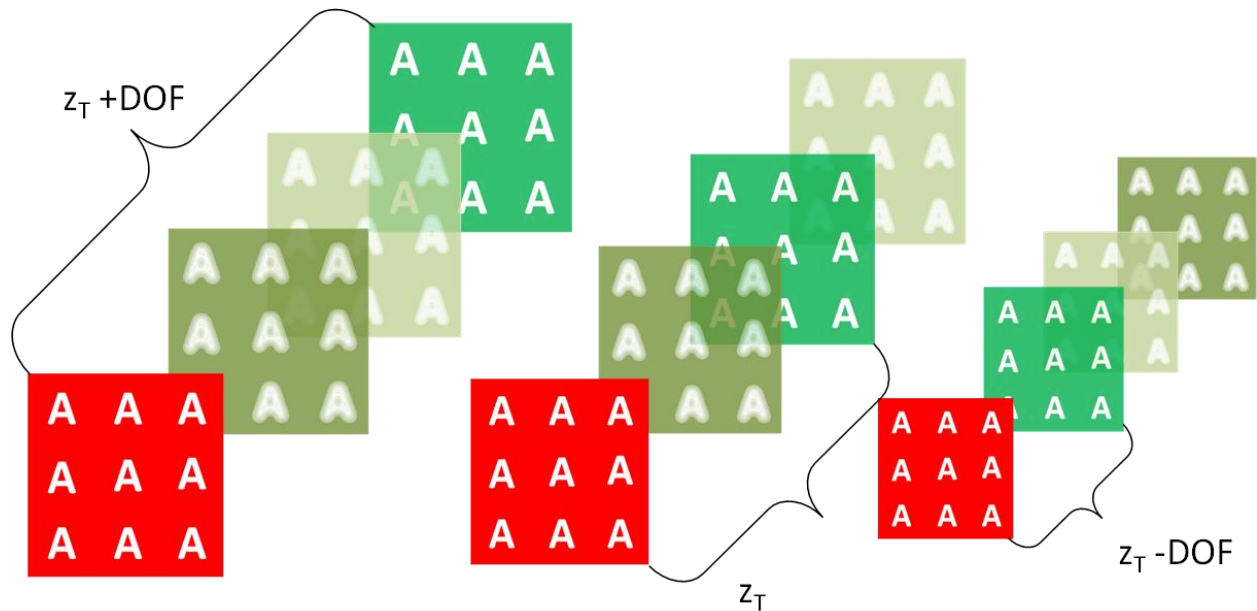


Figure 3-10. Working distance defocusing by changing the pixel size in Talbot masks. Middle inset corresponds to the original size of the Talbot mask, the insets on the left and right produce self images behind and in front of the original (middle) Talbot mask.

This approach has been applied for fabrication of defect tolerant Talbot masks, described in more detail in the chapter 7. The idea of mask defocusing is schematically shown on the Figure 3-10.

An SEM micrograph of a typical mask in low magnification is shown in the Figure 3-11. The above micrograph depicts several diffractive masks defined by the process described earlier in this chapter. The DOF's artificial extension strategy was applied. In the Figure 3-11 there are only 6 masks visible out of total of 9 printed. The field of view of the SEM at this magnification was not sufficient to subtend the entire membrane.

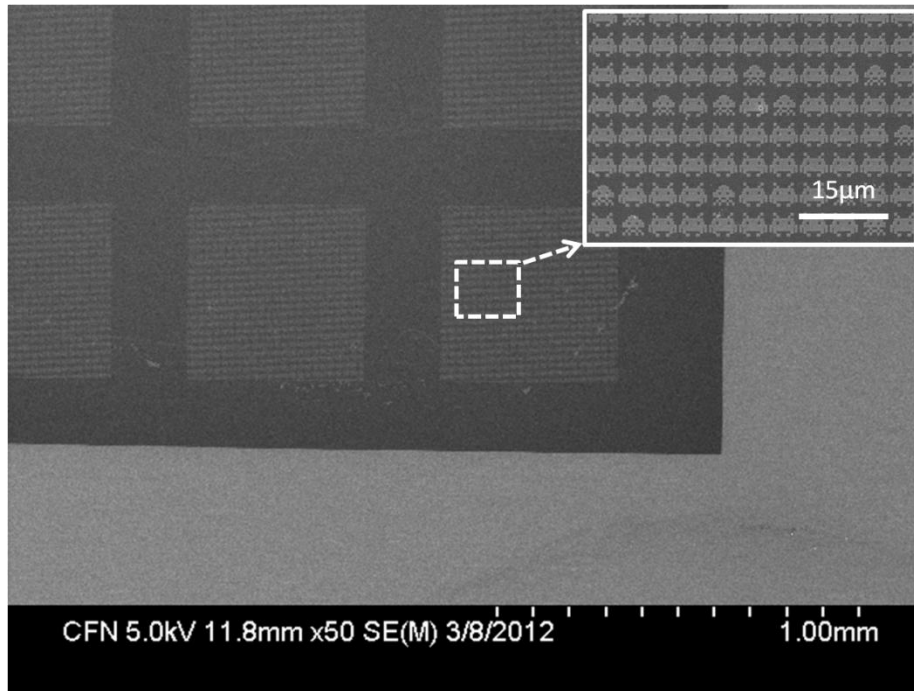


Figure 3-11. An example of several diffractive masks on a silicon nitride membrane. Part of the frame is visible as the brighter shape in lower right corner. Inset in the top right corner depicts the magnified region of a mask.

Part of the frame is visible in the lower right corner of the micrograph. The contrast of the opaque and transparent parts of the mask is well visible on the Figure 3-11.

3.4 ELECTRON BEAM LITHOGRAPHY

3.4.1 SYSTEM OVERVIEW

Most of the masks used in this thesis were printed using electron beam lithography tool at the Center for Functional Nanomaterials located at Brookhaven National Laboratory. The electron beam lithography system used to write the masks was JEOL 6300FS. This is a 100kVe-beam

tool, which enables printing with accuracy of 2nm. The total non stitched writing field area provided by the tool is 1mm². This system uses finely focused electron beam. To generate the electron beam, the JBX-6300FS uses a thermal field-emission cathode with the ZrO/W emitter. The electron beam from the emitter passes through the 4-stage focusing system and then forms the spot on the surface of the substrate. In the electron-beam writing, an electron-beam resist is applied to a substrate and then the substrate is exposed to a scanning electron beam. Both the positive and negative resists are usable. The relationship among the dose Q (C/cm²), the beam current I (A), the writing area S (cm²), and the writing time T (s) is:

$$Q=IT/S$$

For the diffractive masks described in this thesis, the applied dose value was set at 4000 $\mu\text{C}/\text{cm}^2$.

If the scan step of the electron beam is p (cm), the following equation gives the beam scanning speed F (Hz):

$$F=I/(Qp^2)$$

The value of scanning speed is inherent to a specific EBL system. In our case this value was 500MHz. The spot formed on the substrate surface scans over the pattern shapes. The system uses vector scanning by which the electron beam scans only the region where the patterns exist. This scanning method is shown schematically in the Figure 3-12. The vector scan mode of operation assumes scanning the electron beam in selected areas only (indicated by boxes in the Figure 3-12). After scanning a desired region (where the pattern is defined) the beam is blanked (or turned off). Subsequently, the beam moves to another area where the pattern is defined.

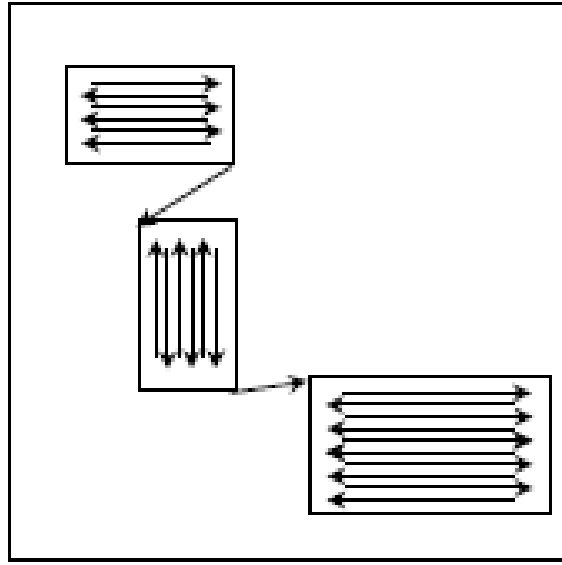


Figure 3-12. Vector scanning of the electron beam [13].

The system has a 2-stage electrostatic deflector that consists of a positioning deflector (main deflector) and a scanning deflector (sub deflector). The region that the positioning deflector scans is called the main-deflection scan region, and the region that the scanning deflector scans is called the sub-deflection scan region. During the EBL tool operation, the two deflectors play different roles. The main deflector is for high-precision positioning, and the sub deflector for high-speed beam scanning. The region that the electron beam scans using the combination of the main and the sub deflectors is called the writing field. After writing one field using the beam scanning, the system moves the substrate stage the distance equivalent to a field to write the next field. This manner of writing is called the step-and-repeat method. The system repeats field writing and stage movement until it writes over all the fields [12].

3.4.2 STAGE-POSITION DETECTION

To assure high precision positioning of the sample related to the beam a specialized interferometric system is used. As it is schematically shown in the Figure 3-13 and Figure 3-14, the stage position interferometer measures the amount of movement of the stage to pinpoint its precise position.

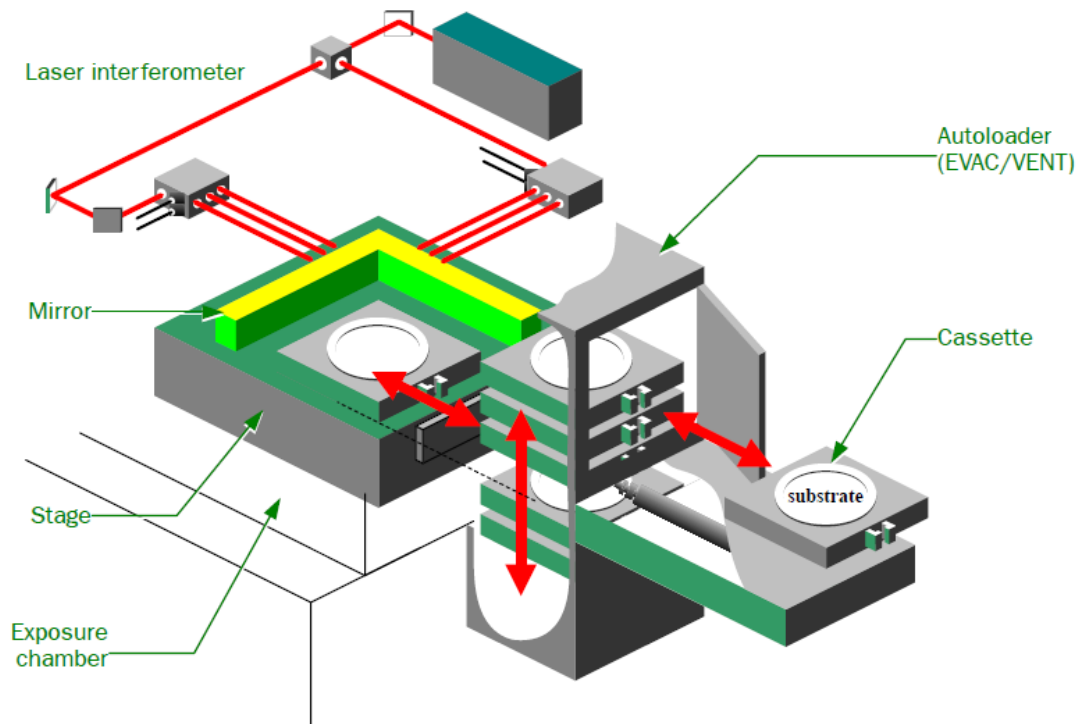


Figure 3-13. Sample handling system. Picture adopted from reference [13]

The stage is equipped with two reflectors, each for X and Y axis. The interferometer precisely measures the mirror position for each axis. The measurement resolution is $\lambda/1024$ (0.62 nm). To precisely control the substrate position in relation to the electron-beam position, the lithography system determines the difference between the substrate position obtained by the laser interferometer and the specified position, and then provides feedback on the difference as an

error to the electron-beam position, thereby writing the pattern in the correct position. This feature is called LBC (laser-beam control). Normally, the LBC feature operates for positional errors in the range $\pm 10 \mu\text{m}$.

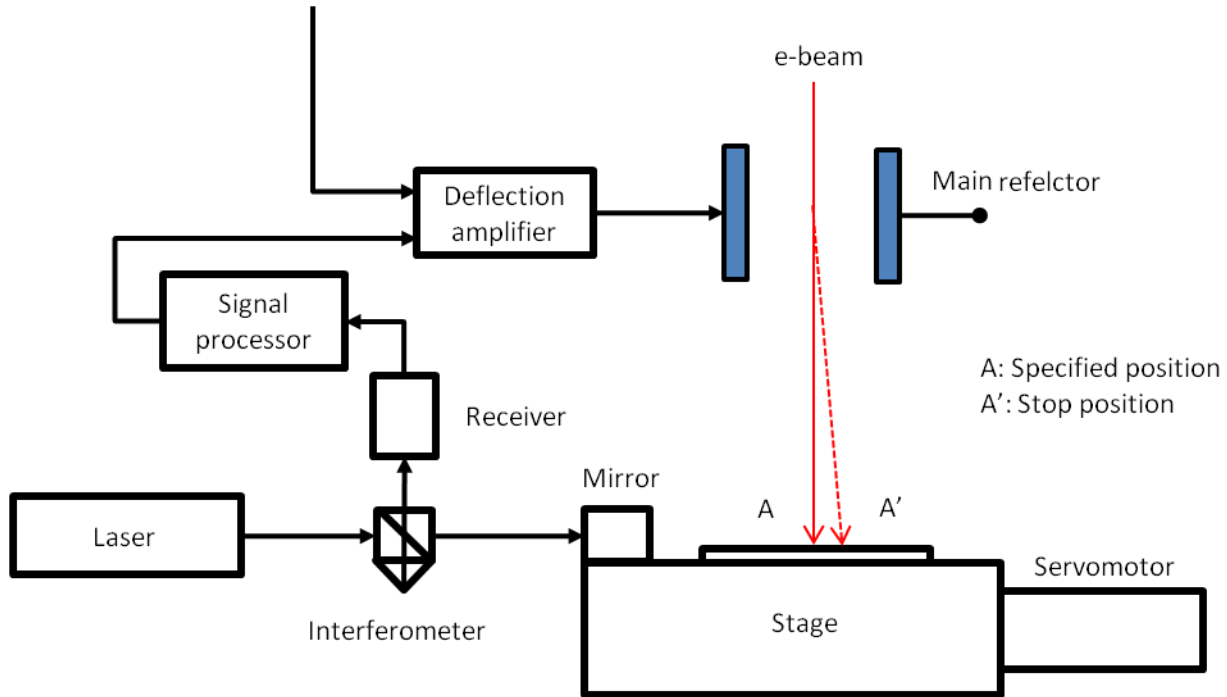


Figure 3-14. Schematic of the laser beam control [13].

3.4.3 FILES PREPARATION FOR E-BEAM LITHOGRAPHY

All masks were generated using MatLab software. The output file of MatLab routines used to generate the files was a bitmap (*.bmp file). In order to convert these files to format handled by electron beam lithography tool, software called Layout BEAMER was applied. Layout BEAMER is a comprehensive and fully integrated software package for e-beam lithography, including proximity effect correction (PEC), e-beam/process modeling, and fracturing to e-beam

machine formats. This software converted the mask file in the bitmap format to a J52 v3.0 (*.v30) file. Layout BEAMER supports different input graphic files such as bitmaps (BMP) and AutoCad drawings (GDSII, DXF). It converts the vertices corresponding to the mask features into polygons. In the conversion process, Layout BEAMER enabled various binary image operations. One of the operations used in the file preparation process was image inversion. Thus prepared file was then copied to the computer controlling electron beam lithography tool.

On the computer controlling the JEOL 6300FS, two files had to be created, namely SDF (schedule file) and JDF (jobdeck file). The JDF file contains most of the specifics about the exposure: patterns, array layout, dose, current, calibration table, etc. The SDF file supplies the information to the EBL tool about which JDF (and parts of JDF) file(s) to write and at which position. An exact description of the files necessary for EBL fabrication and commands used therein can be found in the reference manual at the Center for Functional Nanomaterials [12]. The reference manual used for guidance in the EBL tool operation can be found in [12, 13].

3.5 REFERENCES

- [1] *Soft X-Rays and Extreme Ultraviolet Radiation Principles and Applications*, D.T. Attwood, Cambridge University Press (2007).
- [2] *Talbot lithography: Self-imaging of complex structures*, A. Isoyan, F. Jiang, Y. C. Cheng, F. Cerrina, P. Wachulak, L. Urbanski, J. Rocca, C. Menoni, and M. Marconi, *J. Vac. Sci. Technol. B*, **27**, 2931 (2009).
- [3] *Extreme ultraviolet holographic lithography with a table-top laser*, A. Isoyan, F. Jiang, Y.-C. Cheng, P. Wachulak, L. Urbanski, J. Rocca, C. Menoni, M. Marconi, and F. Cerrina, . Proc. SPIE, **7271**, 72713O (2009).
- [4] *Analysis of a scheme for de-magnified talbot lithography*, L. Urbanski, M. C. Marconi, A. Isoyan, A. Stein, C. S. Menoni, and J. J. Rocca, *J. Vac. Sci. Technol. B*, **29**, 06F504 (2011).
- [5] *Defect tolerant extreme ultraviolet nanoscale printing*, L. Urbanski, A. Isoyan, A. Stein, J.J. Rocca, C.S. Menoni and M.C. Marconi, *Opt. Lett.* **37**, 3633 (2012).
- [6] *Center for x-ray optics database* (2009).
- [7] *Influence of deposition conditions on mechanical properties of low-pressure chemical vapor deposited low-stress silicon nitride films*, Y. Toivola, J. Thurn, R.F. Cook, G. Cibuzar, and K. Roberts, *J. App. Phys.* **94**, 6915 (2003).
- [8] C. Constancias, B. Dalzotto, P. Michallon, J. Wallace, and M. Saib. Fabrication of large area ultrathin silicon membrane: Application for high efficiency extreme ultraviolet diffraction gratings, *J. Vac. Sci. Technol. B*, **28**, 194 (2010).

- [9] *Comparison of hydrogen silsesquioxane development methods for sub-10 nm electron beam lithography using accurate linewidth inspection*, D. S. Macintyre and S. Thoms, *J. Vac. Sci. Technol. B*, **29**, 06F307 (2011).
- [10] *Revaptha tapes product technical information*, Nitto-Denko USA (2012).
- [11] *ESPACER 300 technical data sheet*, Showa Denko.
- [12] *JEOL JBX6300-FS basic operating procedure*, A. Stein, Rev. 1.1, 12/14/2010.
- [13] *Reference manual JBX-6300 series operation JEB6300FS-OP-3a*, JEOL 06110562 (2007).

CHAPTER 4 HOLOGRAPHIC LITHOGRAPHY

4.1 INTRODUCTION

In this chapter extreme ultraviolet holographic lithography is discussed. Methods of design and fabrication of computer generated holograms (CGHs) are presented. Numerical simulations are conducted in order to calculate the reconstructed pattern. For the experimental verification two CGHs with different designs were fabricated and reconstructed using extreme ultraviolet light (EUV). The CGH fabrication process is identical in all instances and is presented in detail in chapter 3 of this thesis. The experimental results obtained are summarized and discussed in a section concluding this chapter.

Holography is a technique in optics used for both amplitude and phase information recording. It was introduced by Gabor in 1948 as a new microscopic principle [1]. In classical photography, only the intensity of the optical signal is being registered. As a result, information loss occurs and three dimensional objects are perceived as two dimensional. With the use of a reference wave along with an image wave it is possible to encode the missing phase information. Gabor's original setup for inline holography has gained little attention when presented in 1948. It was some 15 years after the initial Gabor's discovery when holography started gaining interest, due mainly to the development of coherent light sources at different wavelengths that procured the advancement in holography [2]. The main limitation of the original Gabor's in line hologram is the inconvenient placement of the conjugated images (both on the optical axis, symmetric with respect to the hologram), which makes the reconstruction cumbersome. The issue was finally addressed by Leith and Upatnieks with the implementation of the "off-axis holography" [3].

A derivation of the classical holography, where the classically recorded hologram (out of an existing object) is substituted with computer-calculated diffractive structure that recreates the object wave is subjected to detailed analysis in this chapter. Such object is called computer generated hologram. An obvious advantage of this method as compared to classical holography is the fact that the object, out of which the CGH is generated, doesn't require physical existence.

4.2 CGH DESIGN

The design and fabrication of a CHG is a multistep process. The diagram on the Figure 4-1 illustrates the steps of generation of a CHG. Each step from the diagram is explained in detail in the section to follow.

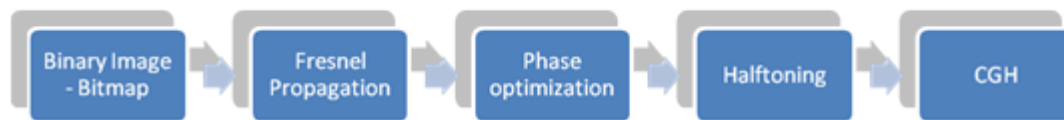


Figure 4-1. Computer generated hologram calculation process.

4.2.1 *Fresnel Propagation*

The first step taken in order to obtain a CGH is the computation of the light distribution at the hologram plane. For the computations fully coherent, monochromatic and collimated illumination has been assumed. Since the spectral linewidth of the light source used is $\Delta\lambda/\lambda = 3 \times 10^{-5}$ [4], the light is fully spatially coherent [5], and the divergence radius is small ($\sim 5\text{mrad}$) [6, 7], all the afore mentioned assumptions are valid. Inline geometry is assumed for calculation as shown in Figure 4-2. Two different sets of coordinates associated with both planes are used.

The object plane is described with (ξ, η) coordinates and the hologram or diffraction plane with (x, y) . The spacing between the object and diffraction planes is further referred to as the working distance. The Fresnel-Kirchhoff diffraction integral is applied for calculation of the optical intensity distribution at a specific distance away from the diffracting object.

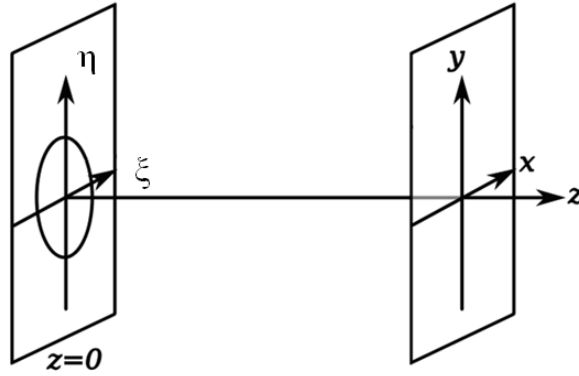


Figure 4-2. The geometry for Fresnel-Kirchhoff integral calculation

With the coordinates systems shown in Figure 4-2 the Fresnel-Kirchhoff integral takes the following expression

$$U(x, y) = \frac{i}{\lambda d} \exp(-i \frac{2\pi d}{\lambda}) \times \int_{-\infty}^{\infty} \int_{-\infty}^{\infty} U(\xi, \eta) \cdot \exp\left\{-\frac{i\pi}{\lambda d} [(x-\xi)^2 + (y-\eta)^2]\right\} \quad (2)$$

Where d is the working distance, $U(x, y)$ and $U(\xi, \eta)$ are complex amplitudes which correspond to the field distributions at the object and the diffraction planes respectively. The function $U(\xi, \eta)$ is sampled on a rectangular raster of $N \times N$ points, with steps $d\xi$ and $d\eta$ along the (ξ, η) coordinates. Since the functional forms $U(x, y)$ and $U(\xi, \eta)$ are related via non-degenerated kernel operator (similar in its form to the Fourier transform) the following relations hold true (3).

$$dx = \frac{1}{Nd\xi}; \quad dy = \frac{1}{Nd\eta} \quad (3)$$

The discrete form of the Fresnel-Kirchhoff integral (2) can be then rewritten as follows (4).

$$U(m, n) = \frac{i}{\lambda d} \exp(-i \frac{2\pi d}{\lambda}) \exp \left[-i\pi\lambda d \left(\frac{m}{N^2 d \xi^2} + \frac{n}{N^2 d \eta^2} \right) \right] \times \sum \sum U(k, l) \cdot \exp \left\{ -\frac{i\pi}{\lambda d} (k^2 \xi^2 + l^2 d \eta^2) \right\} \exp \left\{ i2\pi \left(\frac{km}{N} + \frac{ln}{N} \right) \right\} \quad (4)$$

In formula (4) indices m, n, k, l identify the points corresponding to a rectangular raster of $N \times N$ points and can be considered as pixel coordinates in the digitized space. The equation 4 in the form presented is called the discrete Fresnel transform, which can be calculated using FFT algorithm representation in the following way [8].

$$U(m, n) = IFFT \left\{ FFT \{ U(k, l) \} \times FFT \left[\exp \left[-\frac{i\pi}{\lambda d} (k^2 d \xi^2 + l^2 d \eta^2) \right] \right] \right\} \quad (5)$$

Where IFFT denotes inverse fast Fourier transform.

Using a computational server equipped with 64xUltraSPARC-T2 (1.165GHz) with 32GB RAM was possible to calculate the Fresnel-Kirchhoff diffraction integral within tens of seconds on multi megabyte images. The hologram's transmittance is then represented in the form [8].

$$H(m, n) = \text{Re}\{U(m, n)\} = \frac{1}{2} (U(m, n) + U^*(m, n)) \quad (6)$$

In order to verify if the hologram was successfully calculated, one can back-propagate it down to the object plane.

4.2.2 Phase optimization

As formerly stated, the goal of holography is to retrieve the complete amplitude and phase information of an object. Formula (6) in an explicit manner illustrates how part of the phase information is discarded. In the hologram's reconstruction, the information loss manifests itself in a degradation of the resolution. In order to compensate for the lost phase information, a special algorithm is required. The algorithm was first presented by Grechberg and Saxton in 1972 [9]. It is a computational method for determining the rigorous solution (both in amplitude and phase) of the field distribution at the diffraction plane, based upon the intensity distributions at the object and diffraction planes. The method depends on the Fourier transform relation between the complex amplitudes at these two planes. The method was originally meant for use in the electron microscopy and crystallography.

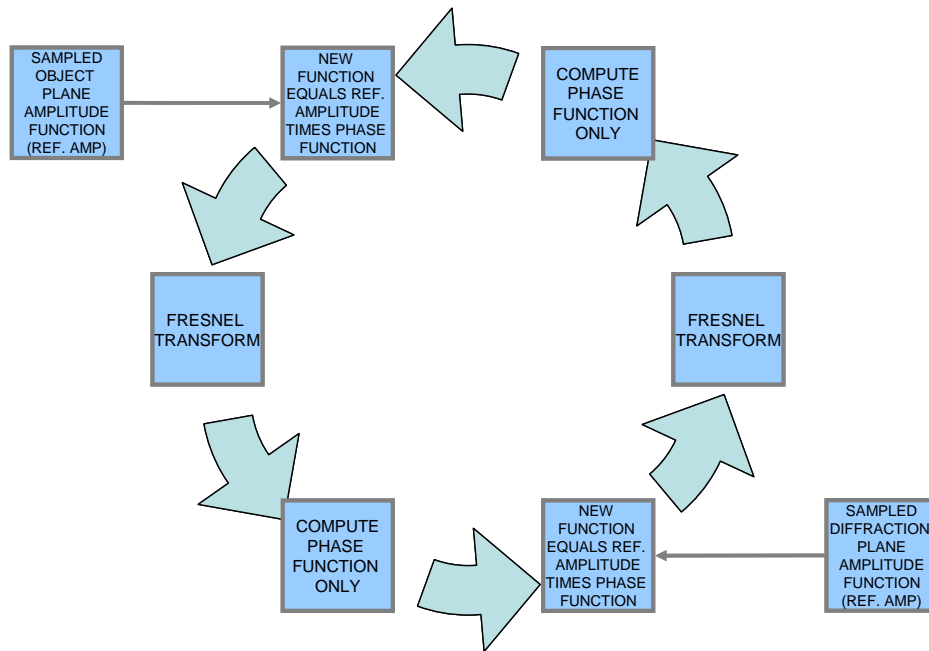


Figure 4-3. Schematic drawing of Grechberg-Saxton algorithm [9].

The Grechberg-Saxton algorithm is an iterative procedure which is shown schematically in the Figure 4-3. The input data to the algorithm are the amplitudes at the mask (object) plane (the CGH) and the reconstruction (diffraction) plane. Both amplitudes are accessed once per iteration. In the first step of the iteration, randomly generated phase with values in the interval $[-\pi, \pi]$ is substituted as the calculated phase. This random phase is used in the first iteration exclusively. The mask's amplitude is then multiplied by the phase function and propagated over the working distance of choice using the Fresnel-Kirchhoff diffraction integral (denoted on the graph as the Fresnel transform). Only the phase of the Fresnel transform is kept, while the amplitude information is discarded. The calculated phase is multiplied by the amplitude of the desired reconstruction image and back-Fresnel transformed over the working distance. At this point, the amplitude is again discarded and a new function is synthesized by multiplying the calculated phase with the amplitude of the mask. At this point one full cycle of the algorithm finishes. The output of the algorithm is the complex representation of the mask (amplitude and phase) [9]. In the case of the CGH presented, the number of iterations was ~ 100 .

4.2.3 *Halftoning*

This section describes the design step of CGHs called halftoning. Given the wavelength, layout, and working distance the diffraction pattern is calculated by numerically solving the two-dimensional Fresnel-Kirchhoff integral. A hologram that can be used in the EUV is limited to be composed of transparent and opaque pixels only. This is because the fabrication techniques and materials which are compatible with the EUV laser wavelength only support binary design. This is explained in more detail in the chapter 3. Therefore, it is not possible for the moment to encode a phase mask in the hologram. This fact imposes very strict limitations on the reconstruction quality. The full information can be only retrieved from a grayscale hologram

(further referred to as the fulltone). Though the information loss is obvious, steps can be undertaken in order to mitigate it by a well know technique called the halftoning. By the definition, halftoning is the process of converting a continuous tone image into a binary pattern of printed and not printed dots [10]. In this work two methods have been applied in order to convert a gray scale image to an equivalent binary form, hard thresholding and dithering.

4.3 HARD THRESHOLD DESIGN

The motif of the first set of CGH masks was a standard lithographic resolution test pattern composed of $1.54\mu\text{m}$ lines and spaces. The field size of CGH masks was approximately $102.9\mu\text{m} \times 102.9\mu\text{m}$. The holograms were calculated for a working distance of $500\mu\text{m}$. The patterns were up-sampled by insertion of a void pixel into every other line in the x and y directions (Figure 4-4a and 4c). The pixel size of the CGH mask was set at 140nm . A single line is 12 pixels wide. The CGH was fabricated in an identical manner as described in chapter 3, in a thin layer of HSQ resist supported by a 25 nm thick silicon nitride membrane. The fabrication technique was electron beam lithography. This set of holograms was binarized using hard thresholding technique. In this method, each pixel of the gray scale image is compared with a threshold value. Depending on whether the pixel value is smaller or larger than the threshold; a binary value (either 0 or 1) is assigned to the pixel. The operation of hard thresholding is described with the following formula.

$$\text{For each pixel in } I(k,l), \text{ set } O(k,l) = \begin{cases} 1, & \text{if } I(k,l) \geq T, \\ 0, & \text{otherwise} \end{cases} . \quad (7)$$

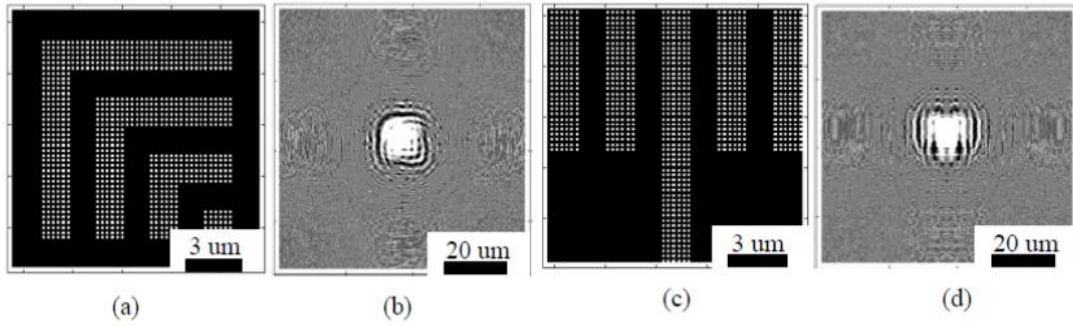


Figure 4-4. CGH input pattern representation of target pattern using half-tone mode (a,c) and calculated CGHs (b,d).

The input is the desired image (Figure 4-4a and Figure 4-4c). A scanning electron microscope (SEM) image of the CGHs masks obtained with applying hard threshold is shown in Figure 4-5 and Figure 4-6.

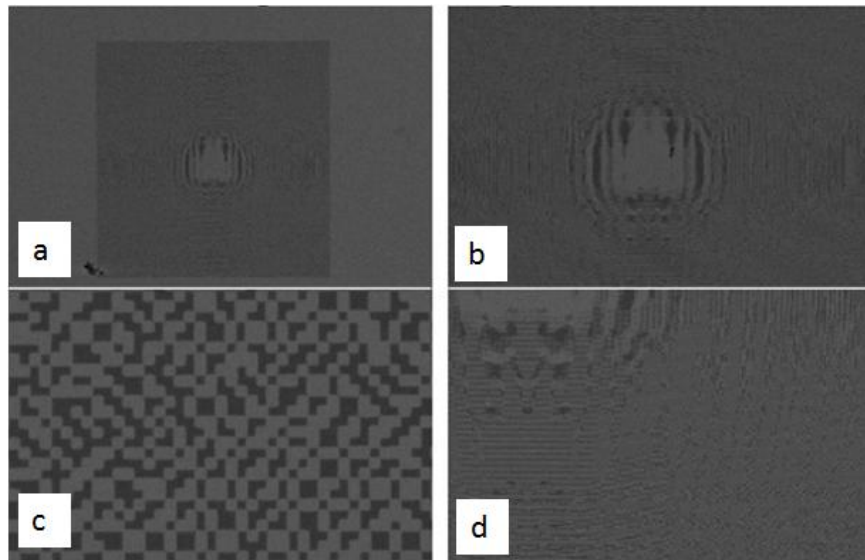


Figure 4-5. Electron micrograph of a CGH mask printed in ~60nm layer of HSQ resist. Four insets show the same hologram observed at different magnifications. The values of the magnification on the micrographs shown in *a, b, c, d* frames are: ~220×, ~450×, ~17,000× and ~2,300× respectively.

The difference between the CGHs showed in the Figure 4-5 and Figure 4-6 lays in different object design. The CGH shown on the Figure 4-5 is set of lines, whereas the CGH shown on the Figure 4-6 is set of elbows. Both these masks are printed on the same membrane.

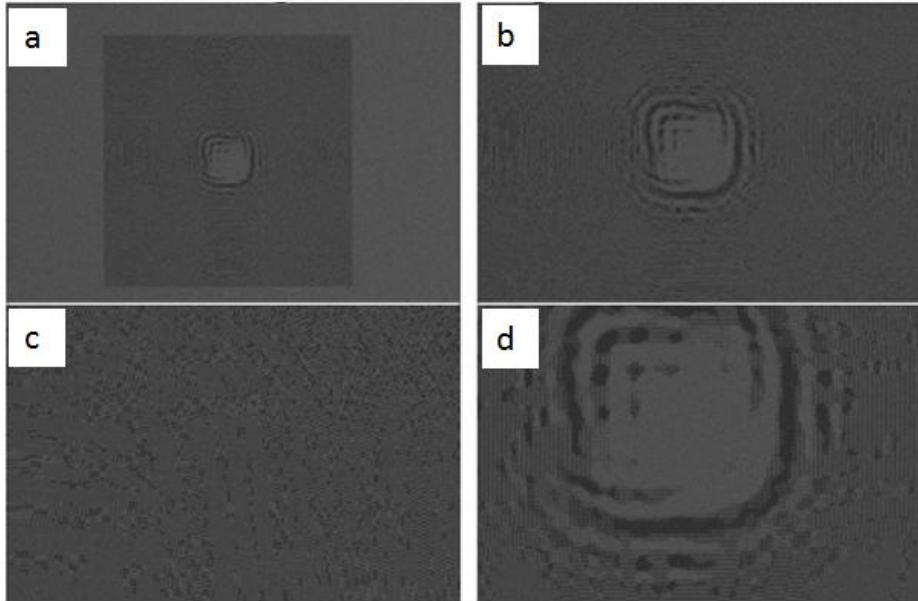


Figure 4-6. Electron micrograph of a CGH mask printed in ~60nm layer of HSQ resist. The four frames show the same hologram observed at different magnifications indicated in the insets. The values of the magnification on the micrographs shown in a,b,c,d frames are: ~220 \times , ~450 \times , ~3,700 \times and ~2,700 \times respectively.

4.4 DITHERING DESIGN

To compare the performance of the CGH binarized with different methods, another binary hologram was designed. In this case, the object was also a standard lithographic resolution test. A set of elbows (Figure 4-8). The pixel size in this mask was 50nm, with two-pixel lines; the width of a single line was 100nm. The total size of the pattern is ~700x700nm².

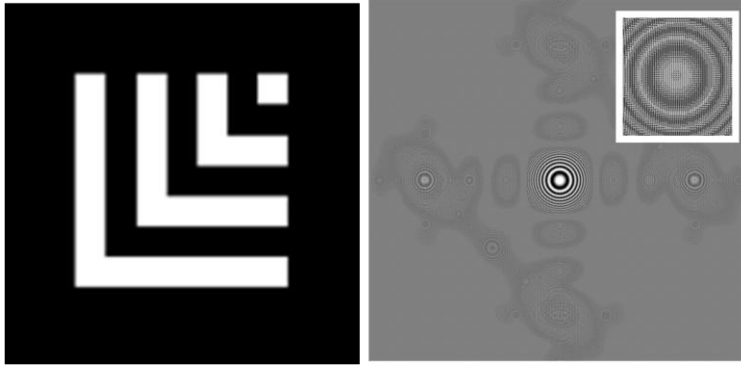


Figure 4-7. The object for CGH generation (left) and a hologram binary mask calculated (left).

The halftoning method used to binarize the second hologram is the screening algorithm also known as dithering. Screening algorithm is a process of representing varying shades of gray by a regular grid of dot clusters that vary in shape and size. A gray scale ramp converted to halftone by the screening algorithm will result in an ensemble of monochromatic dots shown on Figure 4-7.

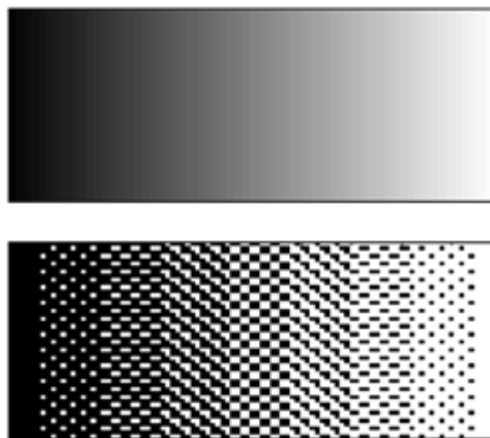


Figure 4-8. Gray scale ramp and its halftone equivalent

The dithering (screening) algorithm can be mathematically described by the following equation:

$$\text{For each pixel in } I(k,l), \text{ set } O(k,l) = \begin{cases} 1, & \text{if } I(k,l) \geq A(k \bmod N, l \bmod N), \\ 0, & \text{otherwise} \end{cases} \quad (8)$$

Where, $O(k,l)$ is the output halftone image, $I(k,l)$ continuous tone image, A is the screen.

A binary mask obtained by application of the dithering method was printed with an electron beam writer. The pattern was defined in a layer of $\sim 70\text{nm}$ of hydrogen silsequioxane resist on top of a silicon nitride membrane as explained in more detail in chapter 3.

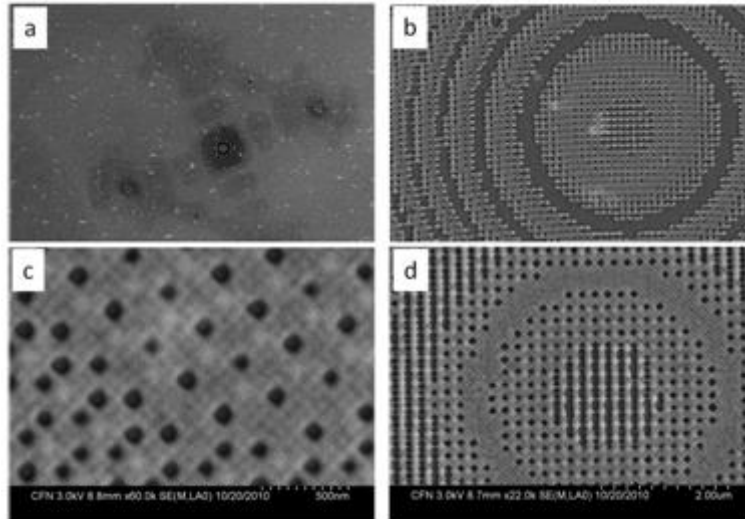


Figure 4-9. Electron micrograph of a CGH half toned using dithering method. The mask is printed in $\sim 60\text{nm}$ layer of HSQ resist. Four frames show the same hologram observed at different magnifications. The values of the magnification on the micrographs shown in the frames a, b, c, d are: $\sim 600\times$, $\sim 11,000\times$, $\sim 60,000\times$ and $\sim 22,000\times$ respectively.

SEM micrographs at different magnification of the CGH can be viewed on the frames of Figure 4-9. Some resist scumming effects can be observed on the low magnification picture (Figure 4-9a). It should be stressed at this point, the pixel size in the case of dithered hologram, was 9 times smaller than the one used to print thresholded hologram. As such it enables printing with better resolution.

4.5 NUMERICAL RECONSTRUCTION

In order to obtain a first order approximation of the reconstructed hologram, a numerical reconstruction was conducted. The hologram was propagated over the reconstruction distance using the Fresnel-Kirchhoff-diffraction integral given by:

$$U(x, y) = \frac{e^{ikz}}{i\lambda z} \int_{-\infty}^{\infty} \int_{-\infty}^{\infty} U(\xi, \eta) \exp\left\{i \frac{k}{2z} [(x - \xi)^2 + (y - \eta)^2]\right\} d\xi d\eta \quad (9)$$

Where $U(x, y)$, $U(\xi, \eta)$ are amplitudes of light in the hologram and reconstruction planes respectively, z is the propagation distance, k is the wave number. In short notation, the equation 9 can be reduced to the form of equation 10, which makes the code implementation more straightforward, namely:

$$U(x, y) = \frac{e^{ikz}}{i\lambda z} \text{FFT}^{-1} \left\{ \text{FFT} \{U(\xi, \eta)\} \text{FFT} \left\{ \exp \left\{ i \frac{k}{2z} [\xi^2 + \eta^2] \right\} \right\} \right\} \quad (10)$$

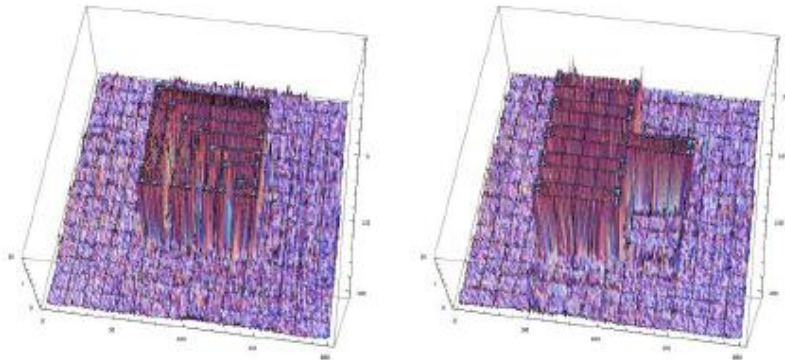


Figure 4-10. Numerical reconstructions of a computer generated holograms. Top view upper images, perspective - lower images. Courtesy of Dr. A. Isoyan.

In Figure 4-10 numerical reconstructions of the computer generated holograms are shown. A good resemblance to the original images can be observed. Using the same reconstruction method the reconstruction of the hologram binarized by the dithering method was calculated. The results are shown on the Figure 4-11.

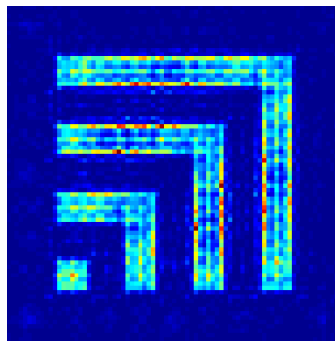


Figure 4-11. Numerical reconstruction of the hologram binarized by the dithering method.

The two methods for CGHs binarization produce results which vary greatly. The criterion used for gauging the reconstruction quality was the peak of the normalized cross correlation function. The cross correlation was computed for the binary object and its numerical reconstruction. The

bound values of the cross correlation function are -1 and +1. The upper bound value of the cross correlation function indicates that two images are identical. The lower bound indicates that the images are complementary to one another. The value zero of the cross correlation function indicates no resemblance between the images. The cross correlation between two images is a standard approach to feature detection [11]. The peak value of the normalized cross correlation function used to quantify the image quality is given by equation 11.

$$\gamma(u, v) = \left| \frac{\sum_{x,y} [r(x, y) - \bar{r}_{u,v}] [o(x-u, y-v) - \bar{o}]}{\left\{ \sum_{x,y} [r(x, y) - \bar{r}_{u,v}]^2 \sum_{x,y} [o(x-u, y-v) - \bar{o}]^2 \right\}^{0.5}} \right|_{\max} \quad (11)$$

Where: $r(x,y)$ is the reconstructed image, o -object, \bar{o} - mean of the object, $\bar{r}_{u,v}$ - is the mean of the reconstructed image under the region subtended by o .

The maximum value of the cross correlation function is used as the object-reconstruction similarity criterion. In the case of the thresholded CGH, the peak value of the cross correlation between the binary object and its numerical reconstruction was $\gamma_T=0.24$. For the case of the dithered CGH this value was $\gamma_D=0.93$. The presented analysis favors the design of the dithered hologram over the hard thresholded one.

4.6 EXPERIMENTAL SETUP AND RESULTS

In this section the results of extreme ultraviolet holographic lithography (EUV-HL) using a compact table top extreme ultraviolet laser are presented. Two CGHs were reconstructed on the surface of a sample coated with resist. One of them was synthesized using hard threshold application; the other using dithering method. Holograms masks with smallest features at 140 nm and 50 nm pixel size were reconstructed with a capillary discharge EUV laser. The images of

CGHs reconstructed in the surface of the photoresist were acquired with an atomic force microscope.

A schematic of the experimental setup is shown on Figure 4-12. A relatively simple arrangement consisting of the holographic mask and the resist coated sample was used. The illumination source in this experiment was the capillary discharge laser (CDL) described in chapter 2. The capillary discharge laser equipped with a 27cm long capillary illuminates the CGH mask that is placed ~ 2.5 m away from the capillary exit. This relative placement of the CDL and the CGHs assures that the beam coherence radius is larger than the size of the single CGH mask. A PMMA coated sample was placed at the calculated working distance (WD) of the CGH mask, equal to $500\mu\text{m}$ in one case and $\sim 250\mu\text{m}$ in the other.

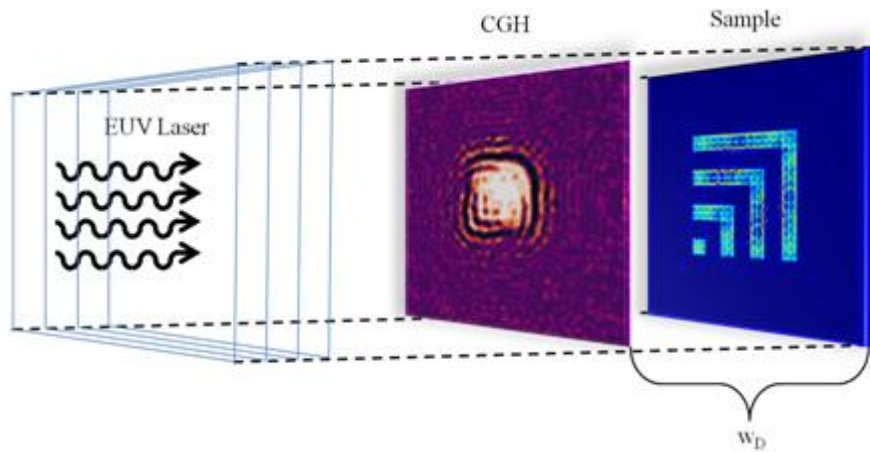


Figure 4-12. Schematic of the CGH reconstruction experimental setup.

In the case of the dithered hologram, the depth of focus (DOF) was only $\sim 155\text{nm}$, thus there were 4 masks, each of which was reconstructing at a plane displaced by a DOF of the original hologram. In this way the effective DOF was artificially extended 4 times. This approach is

discussed in detail in the chapter 3 that treats about the diffractive mask design. The reconstructed CGHs were recorded in the photoresist.

The precise sample positioning was provided by an x - y translation stage driven remotely by vacuum compatible actuators (Thorlabs). On top of that, a piezoelectric stage (Physik Instrumente) has been used to control the working distance. Additionally, the distance from the sample to the mask was measured with a sensor (Mitutoyo - IDC112EB), providing a readout accuracy of $1\mu\text{m}$. The photograph of the experimental set up is shown in Figure 4-13.

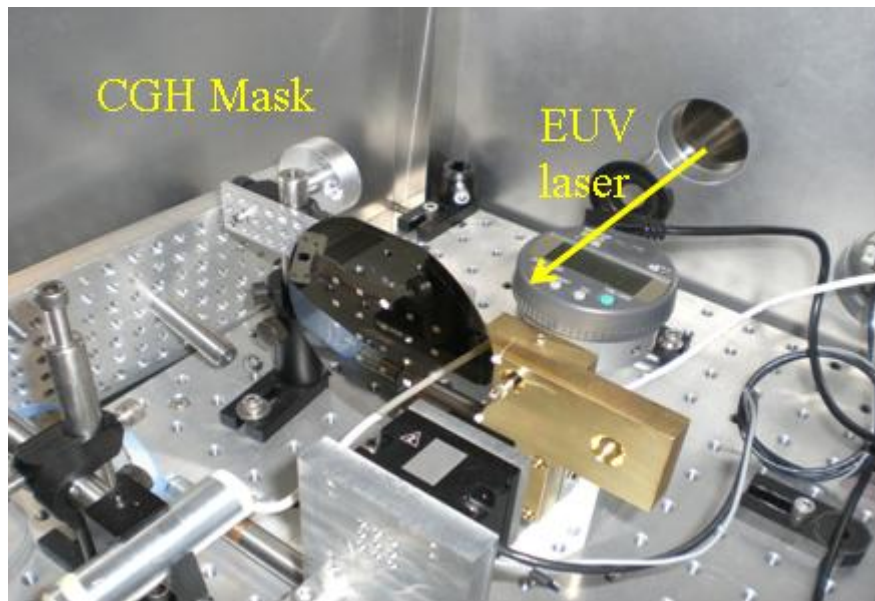


Figure 4-13. A photograph of the experimental setup.

The yellow arrow indicates the direction from which the illumination impinges on the CGH. Downstream the sample is placed (removed in this picture for clarity). In the fabrication process, the carrier membranes were fabricated in a 4 inch wafer, which was subsequently patterned in the electron beam lithography process. In the case of hard threshold CGHs, the wafer was not

cleaved into individual chips from the transportation safety purposes. Thus in the Figure 4-13 the entire 4 inch wafer was used in the experiment.

The results of hard threshold CGHs reconstructions can be illustrated on the Figure 4-14.

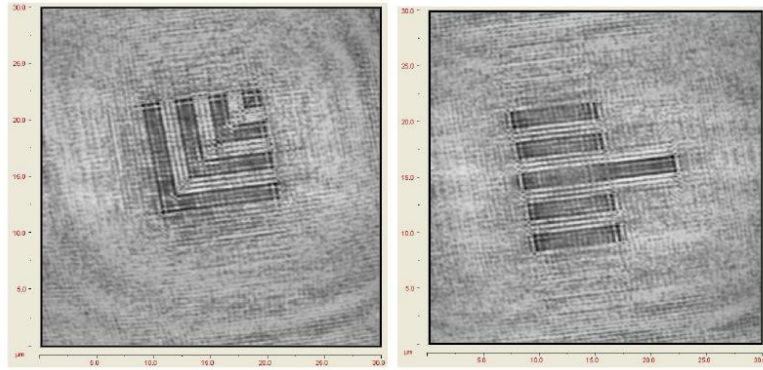


Figure 4-14. AFM micrographs of CGHs reconstructions in resist.



Figure 4-15. AFM micrograph of a CGH reconstructed in PMMA with a lineout showing the ablation crater below.

In the case of the CGH calculated with dithering technique, the reconstructed feature size was over an order of magnitude smaller than the in hard threshold case. The linewidth of the test pattern measured 100 nm. This particular hologram was designed in order to achieve resolution of 52 nm. For that purpose, the holograms filed had to measure $\sim 325 \mu\text{m}$ across and the working

distance had to be equal to $\sim 250 \mu\text{m}$. The numerical aperture is then $\text{NA}=0.55$. Thus, the light collected from an area of $325 \times 325 \mu\text{m}^2$ was focused to the size of $\sim 700 \times 700 \text{nm}^2$. Such an area reduction causes the light focused on the sample surface to ablate the resist instead of exposing it. This phenomenon manifests itself in the shape of reconstruction. The resist is ablated throughout its entire thickness ($\sim 70 \text{nm}$). There is a crater observable, measuring $\sim 700 \times 700 \text{nm}^2$. At the bottom of the ablation crater, there is an indication of the reconstruction as can be seen on the Figure 4-15. The issue of ablation can be addressed in several ways. The most straightforward one is by simply changing resist to one with higher ablation threshold. It was verified experimentally that perhaps the most viable candidate is SU-8 resist. Another possible solution could be attenuation of the illumination. This can be achieved by injecting an inert gas (argon) to the vacuum system downstream the capillary exit. This however has to be done in a controlled manner. The main disadvantage of the workarounds mentioned before (different resist, attenuation) is that the exposure is extremely hard to observe at the developed sample. The AFM used to examine the samples has scanning field of $80 \mu\text{m}$. Moreover the AFM's design does not allow for indexed field stitching with accuracy better than $500 \mu\text{m}$. This makes the search of a $\sim 700 \times 700 \text{nm}^2$ feature extremely cumbersome. Another way of addressing the ablation issue in the reconstruction would be to calculate a CGH with an additional linear phase term encoded, such that, the main feature reconstructs laterally displaced with respect to the center of the hologram's field. This however would require another mask fabrication process. Even after applying the aforementioned solutions, the CDL's shot-to-shot variation of $\sim 8\%$ [7] prevents from reliable printing. The light source in the configuration presented imposes a conceptual limitation of CGH technique used as potential printing technique.

4.7 SUMMARY

In this chapter an account of CGH design, fabrication and reconstruction was presented. The multistep process of hologram calculation was shown in detail. Different techniques of continuous tone hologram binarization were discussed in detail. Binary CGHs were designed. Numerical reconstruction of the binary CGHs, which is a section of this chapter, has proved the effectiveness of this particular hologram generation process. A set of holographic masks designed accordingly was fabricated by the means of the electron beam lithography. The CGHs were reconstructed in experimental setup using EUV laser.

In summary, the holographic projection lithography enables printing of arbitrary, non periodic patterns [11]. Its obvious advantage is the simplicity of the optical setup. The holographic projection lithography relies solely on the physical principles of diffraction and free-space propagation. A single diffractive element is used to print arbitrary shape. This approach, although very minimalistic, greatly complicates once the printed feature size decreases. Smaller feature size implies higher CGH's numerical aperture. The light collected from the entire CGH's aperture is focused into a very small region. This causes the resist in this region to undergo ablation instead of a controlled exposure. Several techniques were mentioned in this chapter, which could potentially alleviate the ablation issue. Yet, still the light source intensity fluctuations preclude the GTI technique from being a reliable technique for nanopatterning. In comparison to the patterning techniques based on the generalized Talbot imaging (GTI), the holographic projection lithography has very little to offer. The printed field size is small compared to the GTI techniques, the hologram's mask is prone to the errors arisen in the fabrication process, and most importantly, it is extremely sensitive to the light source intensity

fluctuations. These issues render the holographic projection lithography method impractical for reliable nanopatterning.

4.8 REFERENCES

- [1] *A New Microscopic Principle*, D. Gabor, *Nature*, **161**, 777 (1948).
- [2] *Optics*, E. Hecht, Addison-Wesley (1998).
- [3] *Progress In Holography*, E.N. Leith, J. Upatniek, *Physics Today*, **25**, 28 (1972).
- [4] *Spectral Linewidth Of A Ne-Like Ar Capillary Discharge Soft-X-Ray Laser And Its Dependence On Amplification Beyond Gain Saturation*, L. Urbanski, M. C. Marconi, L. M. Meng, M. Berrill, O. Guilbaud, A. Klisnick, and J. J. Rocca, *Phys. Rev. A*, **85**, 033837 (2012).
- [5] *Achievement of essentially full spatial coherence in a high-average-power soft-x-ray laser*, Y. Liu, M. Seminario, F. G. Tomasel, C. Chang, J. J. Rocca, and D. T. Attwood, *Phys. Rev. A*, **63**, 033802 (2001).
- [6] *Demonstration of a high average power tabletop soft x-ray laser*, B. R. Benware, C. D. Macchietto, C. H. Moreno, and J. J. Rocca, *Phys. Rev. Lett.* **81**, 5804 (1998).
- [7] *Generation of millijoule-level soft-x-ray laser pulses at a 4-hz repetition rate in a highly saturated tabletop capillary discharge amplifier*, C. D. Macchietto, B. R. Benware, and J. J. Rocca, *Opt. Lett.*, **24**, 1115 (1999).
- [8] *Digital holography digital hologram recording, numerical reconstruction, and related techniques*, U. Schnars and W. Jueptner, Verlag-Springer (2005).
- [9] *Practical Algorithm For Determination Of Phase From Image And Diffraction Plane Pictures*, R.W. Gerchberg, and W.O. Saxton. *Optik*, **35**, 237 (1972).

- [10] *Modern digital halftoning*, D.L. Lau and G.R. Arce, *M. Dekker* (2001).
- [11] *Pattern classification and scene analysis*, R.O. Duda and P.E. Hart, *Wiley* (1973).
- [12] *Extreme ultraviolet holographic lithography with a table-top laser*, A. Isoyan, F. Jiang, Y.-C. Cheng, P. Wachulak, L. Urbanski, J. Rocca, C. Menoni, M. Marconi, and F. Cerrina, *Proc. SPIE*, **7271**, 72713O (2009).

CHAPTER 5 GENERALIZED TALBOT IMAGING

5.1 INTRODUCTION

In this chapter a promising method to generate periodic arrays of nano-structures with EUV light based on self-imaging will be described. A succinct historical introduction is provided, which is then followed by an analytical description of self-imaging phenomenon. Further in this chapter, the results of a numerical simulation of self-imaging are presented in order to corroborate the analytical description. An experimental verification of the theoretical considerations is carried out. The results of the experiment are presented together with a description and analysis. The chapter is concluded with a brief summary.

5.2 HISTORICAL BACKGROUND

Self-imaging is an effect that occurs once a periodic object is illuminated with coherent light. Across the history of optics, self-imaging phenomena were strongly attracting the attention of the scientists. It was first observed by Henry Fox-Talbot in 1836. He has communicated his findings in *Philosophical Magazine*. In the case presented by Talbot, a diffraction grating (made by Fraunhofer) was producing its replicas (or self-images) at a certain distance and its integral multiples, called the Talbot distances. Talbot noticed the self-images in the form of what he described as "numerous bands or lines having green and red color having their direction parallel to the lines of grating" [1]. This phenomenon was called Talbot effect in his honor. For almost half a century after its discovery, self-imaging was rather a mere scientific curiosity without any particular application. The situation was changed by Lord Rayleigh in 1881 [2]. He derived an approximate formula for the Talbot distance using sound propagation theory [3]. The popularity of self-imaging effect peaked in the 1950-1960s. There are multiple publications from that time

period treating about different aspects of self-imaging. One of the most comprehensive ones is a series of three journal articles by Cowley and Moodie [4-6]. A more general view to the self-imaging effects is given by Montgomery in [7]. In his article about self-imaging of infinite aperture objects Montgomery claims that the necessary condition for self-imaging of arbitrary objects is a specific shape of its spatial frequency spectrum. Reference [7] establishes that if the spatial frequency spectrum of any object lays on the series of radially symmetric rings (spaced similarly as in a zone plate), it produces self-images once illuminated. Periodicity of the mask is but a sufficient condition for self-imaging. An experimental verification of Montgomery's prediction is proposed by Indebetouw and Jahns in [8-10]. Among the vast number of applications of self-imaging effect, there is one which deserves special attention, as being the closest to the one presented in this chapter. In reference [11] an approach to nanopatterning called coherent diffraction lithography was reported. In the cited source, self-imaging effect was used to copy ~ 300 nm diameter holes arranged into a hexagonal array with 583 nm period.

The experimental approach to nanopatterning described in this chapter uses the phenomenon called generalized Talbot imaging (GTI). It was first reported by Isoyan in [12]. The generalization in this particular case refers to the pattern itself. Whilst in the case of classical Talbot effect the mask rendering self-images was a diffraction grating, in the case of the GTI, the mask has a form of arbitrarily designed cells arranged into a periodic lattice.

5.3 ANALYTICAL DESCRIPTION

In this section, the analytical description for the original Talbot effect will be presented. The departure point is the theory of diffraction proposed by Kirchhoff incorporating former

postulations made by Fresnel. Using Fresnel-Kirchhoff diffraction integral together with the assumption of paraxial propagation, the condition for self imaging will be derived. The derivation presented here is following closely the one contained in reference [13].

Self imaging phenomena can be described by means of the classical theory of diffraction introduced by Kirchhoff. There are two regimes of diffraction set by the distance from a diffracting structure at which the light intensity is being analyzed, the size of aperture and the wavelength of illumination. The regime, where the light intensity is being calculated is far from the diffracting structure is called Fraunhofer or far field diffraction. When the calculation takes place right after the diffracting structure, the regime is called the Fresnel or near field diffraction. Usage of both cases can be formalized according the value of the Fresnel number, defined as:

$$N_F = \frac{a^2}{\lambda L} \quad (1)$$

Where: a denotes the aperture size, L is the distance between the aperture and the observation plane and λ is the wavelength of illumination. When the Fresnel number is $\ll 1$, the case is referred to as the far field diffraction [14]. Otherwise we are in the near field diffraction regime. The latter case is of interest to us.

The most convenient way to describe Talbot imaging is using the spatial frequency domain. Let us depart from the description of a diffraction grating in the spatial domain.

$$g = \text{Rect}(x) \otimes \sum_{n=1}^N \delta(x - np) \quad (2)$$

Where the *Rect* function is defined as:

$$Rect(x) = \begin{cases} 1 & |x| < \frac{1}{2} \\ \frac{1}{2} & |x| = \frac{1}{2} \\ 0 & otherwise \end{cases} \quad (3)$$

and p denotes the period and is related to the characteristic spatial frequency via:

$$p = \frac{1}{\nu_0} \quad (4)$$

Transfer to the spatial frequency domain is realized by applying Fourier transform.

$$\tilde{g}(\nu) = F\{Rect(x)\} \times F\left\{\sum_{n=1}^N \delta(np)\right\} \quad (5)$$

To the form given by the following equation:

$$\tilde{g}(\nu) = sinc(\nu) \times \sum_{n=1}^N \delta(n\nu_0) \quad (6)$$

The propagation by a distance z of a wave impinging on this periodic structure in the spatial frequency domain is equivalent to a multiplication by a quadratic term, if the paraxial approximation is assumed

$$\exp(-i\pi\lambda z \nu^2) \quad (7)$$

This leads to the form given by the equation 8

$$\tilde{g}(v) = \text{sinc}(v) \times \sum_{n=1}^N \delta(nv_0) \exp(-i\pi\lambda z v^2) \quad (8)$$

The sifting property of Dirac delta function leads to the form:

$$\tilde{g}(v) = \text{sinc}(v) \times \sum_{n=1}^N \exp(-i\pi\lambda z n^2 v_0^2) \quad (9)$$

The spatial frequency spectrum of the grating is represented by the first term in the eq. 9. It is conserved only if the phase term is equal 1, or the exponent is equal to integral multiples of 2π .

$$(-i\pi\lambda z n^2 v_0^2) = 2m\pi \quad m = 1, 2, 3, \dots \quad (10)$$

This leads to the condition of self imaging in the following relation.

$$z = 2 \frac{Mp^2}{\lambda} \quad M = 1, 2, 3, \dots \quad (11)$$

The above derivation yields the condition for self imaging for a binary diffraction grating. The replicas of the grating appear at equidistant planes referred to as the Talbot planes. It is important to notice, that the $Rect(x)$ function in equation 2, which represents the shape of single grating groove, can be substituted by any transmittance function. It is also noticeable that at the fractional Talbot distances, when M is a rational number, sub images also appear. These are referred to as the Talbot sub images. The main characteristic of Talbot sub images is their multiplication in spatial frequency. This feature is readily visible in numerical calculations of the intensity distribution along the axis of propagation and will be one of the subjects of the next section.

5.4 NUMERICAL SIMULATION

This section describes the numerical calculation of the light intensity distribution after the periodic mask. Numerical simulations are of key significance, as they allow assessing the experimental result at the mask preproduction stage. Knowing the light intensity distribution at the grating (or any other periodic mask) plane, it is possible to calculate the light intensity distribution at any distance behind it by means of Fresnel-Kirchhoff diffraction integral. The calculation is done using MATLAB. The Fresnel-Kirchhoff integral in its discrete form is calculated using series of Fourier transforms. This has been shown in the chapter 4. In the simulation presented, the intensity distribution is calculated for a 1-D object at a discrete value of the propagation distance (z) from a given interval. Each "slice" is a solution to one dimensional Fresnel-Kirchhoff integral of the object calculated at different distance away from the mask.

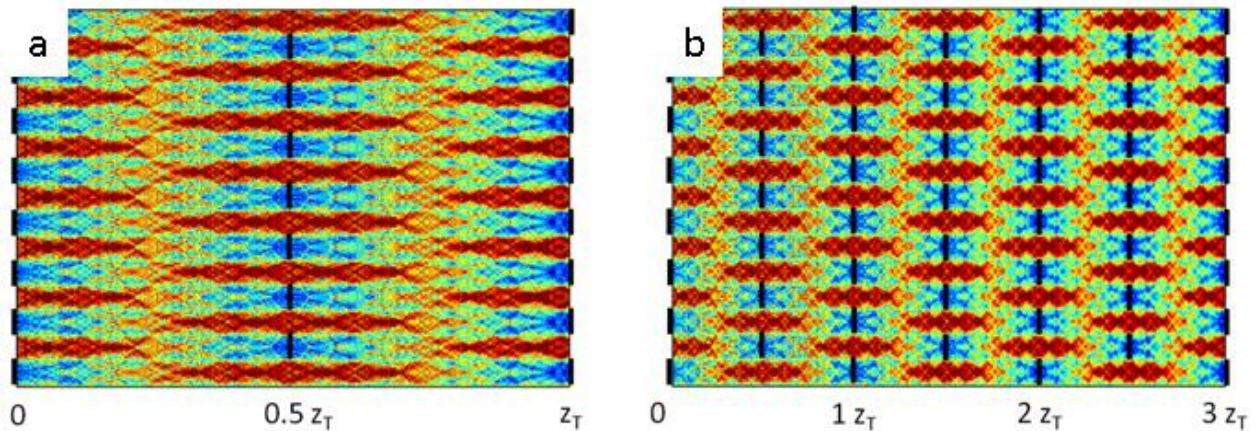


Figure 5-1. Talbot carpets calculated for a grating-like structure. Insets a, b are different instances differing with longitudinal distance of propagation (a - single Talbot distance, b - 3 Talbot distances). The binary diffracting grating is repeated at the integral and fractional Talbot distances.

Such an arrangement presented in pseudo-color is sometimes referred to as the Talbot carpet owing to its picturesque appearance. The abscissa axis in the Talbot carpets presented on the

Figure 5-1 corresponds to the direction of propagation; the ordinate is the lateral distance across the mask grating and the intensity is plotted using a color scale. In the case presented on the Figure 5-1, the calculations are conducted for different propagation distances. In the frame 1a the Talbot carpet corresponds to one Talbot distance propagation. Frame 1b shows Talbot carpet for propagation by 3 Talbot distances. The fact, that the periodic mask creates its own replicas at discrete, equally spaced distances is indicated by the black dashed lines on the Figure 5-1.

5.5 GENERALIZED TALBOT EFFECT

In this section, the concept of GTI is introduced and then followed by a numerical example. A structure of arbitrary design composed into a periodic array exhibits self imaging behavior when it is illuminated by coherent light. From the analytical derivation shown previously, the sufficient condition for the Talbot effect to occur, is the periodic character of the diffracting object. It can be noticed that the object of interest has a general form. Namely, in the spatial domain, it is a convolution of a certain function (representing a single cell) with a summation of Dirac delta functions spaced by a specific period (also known as Dirac comb or Shah [14]). For example in the case of a diffraction grating a *Rect* function (single groove) is convoluted with a Dirac comb function with certain period (equations 2, 3). From the analytical standpoint, in the spatial frequency domain the Dirac comb function acts on the propagating term (equation 7) by sifting it at the spatial frequency corresponding to the grating's period [ibid.].

Let us now consider generalization to the previous case when the single cell has a form of an arbitrary function. After a similar derivation as for the diffraction grating, the same conclusion can be drawn (equations 12-14). Namely, the periodic mask will create replicas of

itself at the Talbot distances. By denoting the generalized function describing a single cell by $G(x)$ one obtains the expression for the arbitrary mask:

$$g = G(x) \otimes \sum_{n=1}^N \delta(np) \quad (12)$$

Now by propagating it similarly as in the example with a diffraction grating one obtains:

$$\tilde{g} = \text{sinc}(v) \times \sum_{n=1}^N \exp(-i\pi\lambda z n^2 v_0^2) \quad (13)$$

Again, when the second term is equal to one, the self-imaging condition is fulfilled. This only happens when:

$$z = 2 \frac{Mp^2}{\lambda} \quad M = 1, 2, 3, \dots \quad (14)$$

It is shown by the following numerical example. Let the mask have a profile illustrated on Figure 5-2.

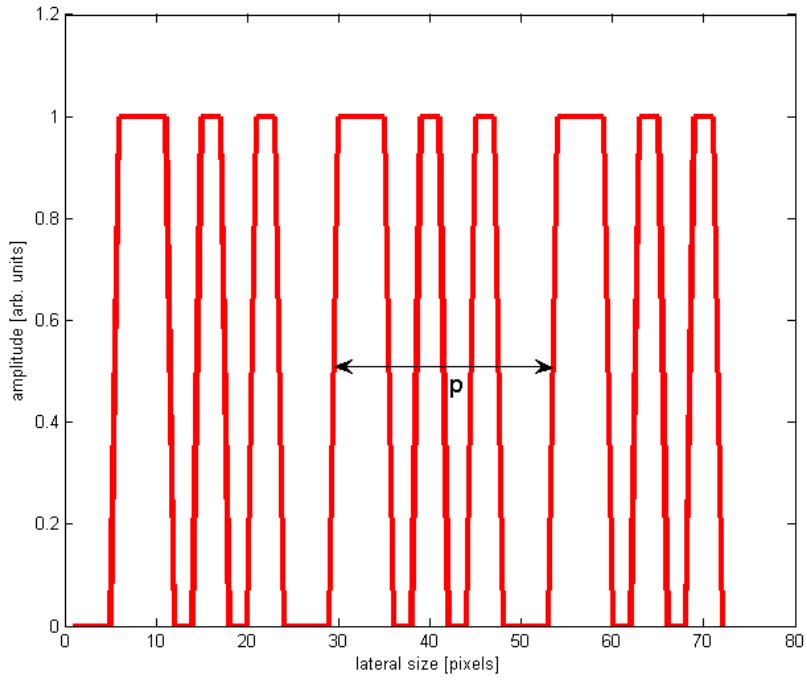


Figure 5-2. Profile of an arbitrary shaped diffracting structure tiled periodically. The period is indicated by the arrow and denoted by letter p .

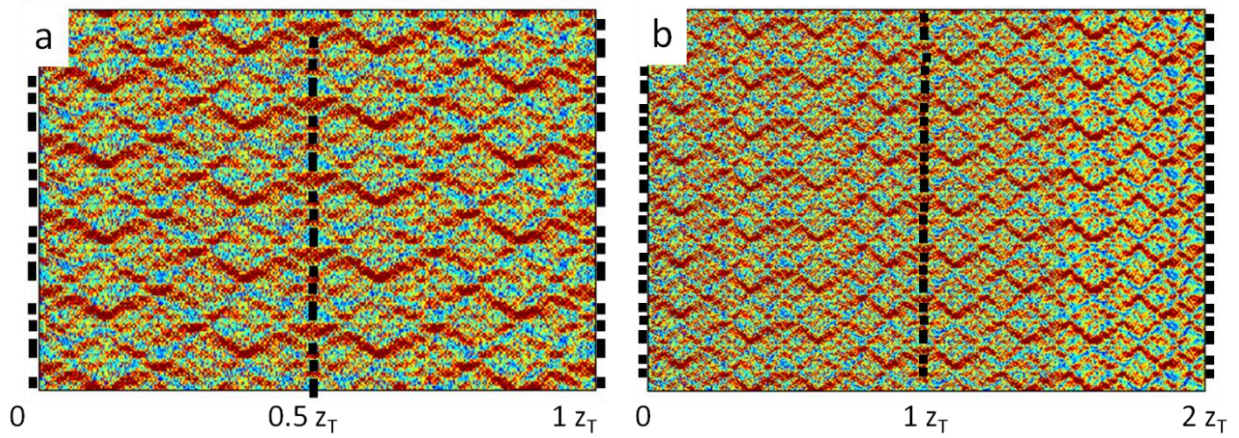


Figure 5-3. Talbot carpets for arbitrary structure arranged in a periodic array. Inset a) shows blown up region of inset b).

The results presented in the Figure 5-3 show the Talbot carpets calculated for different distances of propagation ($1z_T$, $2z_T$). For clarity, the black dashed lines depict the loci of the replicas emergence. Both figures show Talbot carpets for the same structure shown in the Figure 5-2. In the frame Figure 5-3a, the half Talbot distance is shown. The characteristic of the replica at this distance is half period lateral shift with respect to the original.

5.6 APPLICATION OF GENERALIZED TALBOT IMAGING TO NANOPATTERNING

As originally proposed by Rayleigh, self imaging can be successfully applied to copy periodic structures. Rayleigh, in late nineteenth century copied diffraction gratings by simply recording their self images on the glass plates coated with photographic emulsion [2]. In the work by Zanke et.al, reported in [11], the self-imaging effect was used to print square and hexagonal arrays of pillars. This technique was called “coherent diffraction imaging” and was applied in manufacturing photonic crystal structures.

A novel high resolution patterning approach capable of patterning large area periodic structures of arbitrary content with nanoscale resolution has been reported by Isoyan et. al. in [12]. It is based on self-imaging extended to the GTI. The general idea of GTI was explained in the previous section: a periodic object forms highly accurate real images of itself at distances that are integer multiples of a fundamental unit, the Talbot distance. At these locations the interference of the waves diffracted by the periodic structures recreates the image of the object without the necessity of any optics (equations 10 and 13). Clearly GTI is an extension of the classical self-imaging originally described by Talbot. Interestingly, this more general aspect of Talbot imaging has received only very little attention over almost 180 years which have elapsed

since the original discovery by Talbot. This can be attributed to the difficulty of creating high-resolution periodic patterns, a topic of little, if any interest until the advent of the semiconductor industry, and to the concomitant need for highly coherent sources. In addition, the development of excellent imaging optics did obviate the need for exploiting the properties of self-imaging objects except for the few areas where no optical system can be easily built. X-ray and EUV are two such regions of great interest for imaging and nanofabrication. The experiment described here, demonstrates that the combination of a coherent illumination source with a nanofabricated Talbot mask allows for the extension of nanolithography in a relatively simple setup. The Talbot template embodies both the information to be written in the exposure field and the image formation system. An advantage of this technique is that any defect on the original mask object is averaged over the entire imaging field, and since the defect/image ratio is in general small, the formed image is defect free. The property of defect tolerance of GTI is elaborated in greater detail in the chapter 7. Another favorable characteristic of the method is that the focal or working distance between mask and wafer is very large in comparison to the features size. In its simplicity, GTI opens the door to novel application of nanolithography of periodic patterns, such as high-density memories or magnetic media, where a regular pattern is repeated over certain area. The ability to form a projected self-image of a complex periodic object has great interest in semiconductor and device fabrication if one could extend the imaging to the nanometer region. In this section of the chapter the results of an initial demonstration of GTI using coherent EUV illumination source are shown.

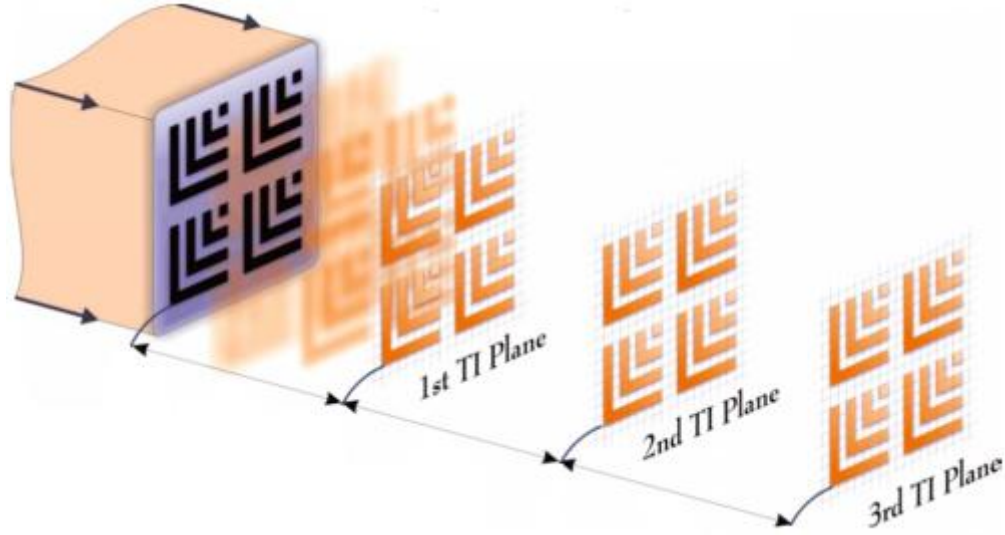


Figure 5-4. Schematic arrangement for GTI.

Figure 5-4 shows schematically the experimental setup. The mask has the form a periodic array of elbows. In the experiment, the mask is illuminated with coherent EUV light and creates replicas at the Talbot distances. The analysis of the case of a simple linear grating system assumes that the grating is infinite. In practice, one must consider the effect of the finite size of the mask due to the fabrication and other experimental limitations. The questions which arise are: 1) what is the optimal size of the mask that should be designed for GTI and 2) what is the resolution that is attainable with such an imaging system in realistic conditions of finite partial coherence. A simple argument helps to provide the answers. Let $2W$ be the lateral size of the Talbot mask template. The angle subtended by the template at the sample position, i.e., at a distance z_T , is then given by:

$$\sin(\alpha) = W / \sqrt{W^2 + z_T^2} = 1 / \sqrt{1 + (z_T / W)^2} = NA \quad (15)$$

This is the numerical aperture of an equivalent image forming optical system, converging with angle α to the sample. In this case it is a “virtual” NA, since no optics exists to limit the angle.

Alternatively, we can note that the size of the Talbot mask determines how many diffraction orders can illuminate the center of the image, and thus the resolution. If λ is the wavelength of illumination, then the diffraction limit for resolution is given by

$$\Delta = 0.61 \frac{\lambda}{NA} = 0.61\lambda \sqrt{1 + \left(\frac{z_T}{W}\right)^2} \quad (16)$$

i.e., the resolving power is proportional to the size of the mask, and inversely proportional to the Talbot distance. Further simplifying the relation, we obtain an expression for the resolution for the Talbot image of order n :

$$\Delta_n = 0.61\lambda \sqrt{1 + \left(\frac{2np^2}{\lambda W}\right)^2} \quad (17)$$

Showing how the resolution improves for smaller periods, larger widths of the mask, and smaller Talbot distances. As follows from equation 17 the number of cells in the mask for n -th Talbot imaging plane can be written as

$$M = \frac{4np}{\sqrt{((2\Delta_n)^2 - \lambda^2)}} \quad (18)$$

Also we can clearly see that the theoretical resolution limit of the GTI equals 0.61λ . As in all imaging systems, the depth of focus depends on the resolution and on the numerical aperture of the system. For a diffraction limited system, we have:

$$DOF = \frac{\lambda}{NA^2} = \lambda \left[1 + \left(\frac{2np^2}{\lambda W}\right)^2 \right] \quad (19)$$

Where: the *DOF* refers to the section along the optical axis symmetrical with respect to the focal spot where the intensity of light decreases by 20 per cent [15].

The design of the mask is relatively simple. The elementary cell pattern is repeated with identical periods in the x and y directions. For a given wavelength and desired Talbot distance the corresponding period of the two-dimensional array was calculated. The actual fabrication process of the mask is based on one of the standard processes developed at the Center for Nanotechnology at University of Wisconsin (CNTech) for EUV optics. The mask fabrication details along with the corresponding recipes are exhaustively described in chapter 3 and appendix 2. A ~25nm thick silicon nitride (SiNH_3) membrane with a transmission $T = 13.5\%$ at 46.9nm wavelength was used [16] as the support. The Talbot mask plate was patterned using standard electron-beam lithography in a ~70nm thick hydrogen silsesquioxane photoresist (HSQ). This film efficiently absorbs the radiation at 46.9 nm, with a transmission of approximately 3% [17]. The electron micrographs of the GTI mask can be viewed on the Figure 5-5. The insets show different motifs printed along with a magnified image of the elementary cell (upper right corner of each frame).

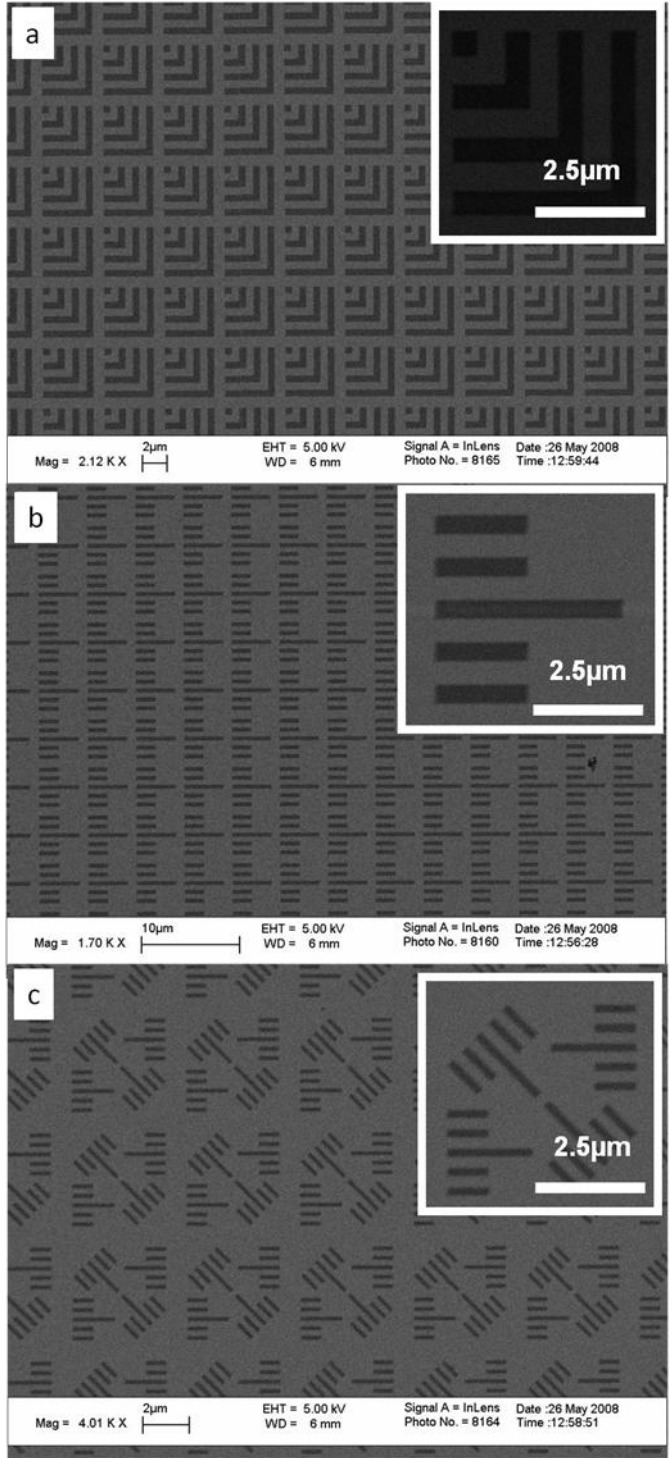


Figure 5-5. Electron micrographs of mask fabricated on thin silicon nitride membrane. Top right insets in figures 5-5a, 5-5b and 5-5c show the elementary cell of different motifs (courtesy of Dr. Artak Isoyan – Synopsys Inc.).

The field size of the mask is approximately $600 \times 600 \mu\text{m}^2$ at a distance of 1 mm for the first Talbot plane. The period of the patterns in the mask was $4.845 \mu\text{m}$, and the pixel size was defined as 140nm.

The masks were illuminated with coherent EUV light from the tabletop capillary discharge laser described in detail in chapter 2 and references [17, 18].

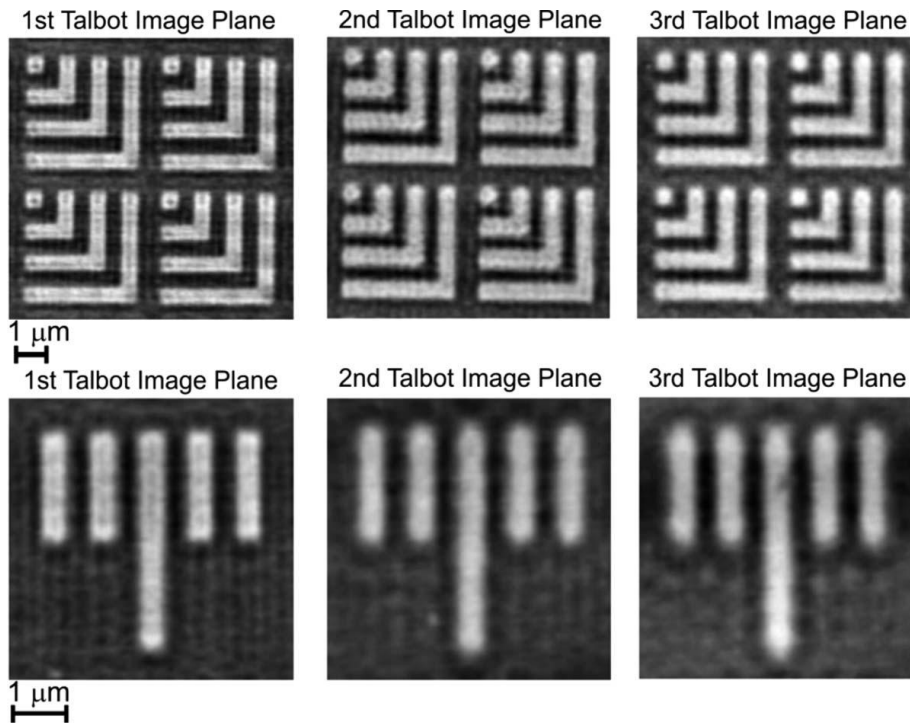


Figure 5-6. AFM images of test patterns recorded at several Talbot planes in 70 nm thick PMMA.

The reconstruction was recorded in a polymethyl-metacrylate (PMMA) resist coated sample. The sample was placed at calculated Talbot distance (~ 1 mm) away from the mask. Typical patterns obtained with an atomic force microscope (AFM) are shown in Figure 5-6. The GTI technique yields consistent images as far as 3mm away from the mask, as shown on the Figure 5-6. There is an observable loss of the resolution with the Talbot order which is due to two effects. First is progressively decreasing the NA of the mask (the working distance increases

at consecutive Talbot orders). The second is the finite value of temporal coherence of the EUV laser. A precise account of the influence of temporal coherence of the light source on the resolution of the self-images can be found in [29].

The self-images were printed up to the 6th Talbot order, which yielded a total mask-sample stand-off distance equal to 6mm. The fidelity of printing can be viewed on the Figure 5-7. Figure 5-7b shows the capability of the technique to print high resolution over large areas.

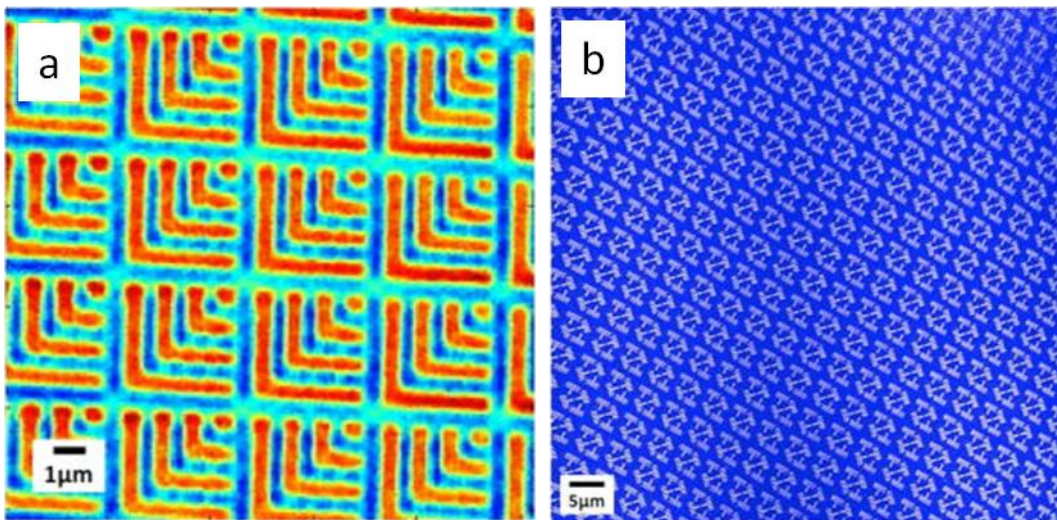


Figure 5-7. AFM scan of Talbot images of the reconstructions. Inset 7a is the reconstruction at the sixth Talbot distance (6 mm away from the mask). Inset 7b shows GTI technique capability of high fidelity printing over large areas.

In order to explore the printing resolution dependence on the mask's width (equation 17) another mask with an identical design was fabricated. In this case, the mask was printed over a ~200nm thick silicon membrane, which provided with ~36% transmission at 46.9nm wavelength. The mask width was $1 \times 1 \text{mm}^2$. Compared to the mask printed over a silicon nitride membrane ($600 \times 600 \mu\text{m}^2$). The mask fabrication process was kept the same (chapter 3). The experimental conditions (dose and developing) in both cases were identical. The dose in both cases was 300

laser shots, while the developing time was 45 seconds in 25% solution of MIBK in isopropanol. The SEM micrographs of the masks along with the AFM micrographs obtained in the reconstruction are shown in the Figure 5-8.

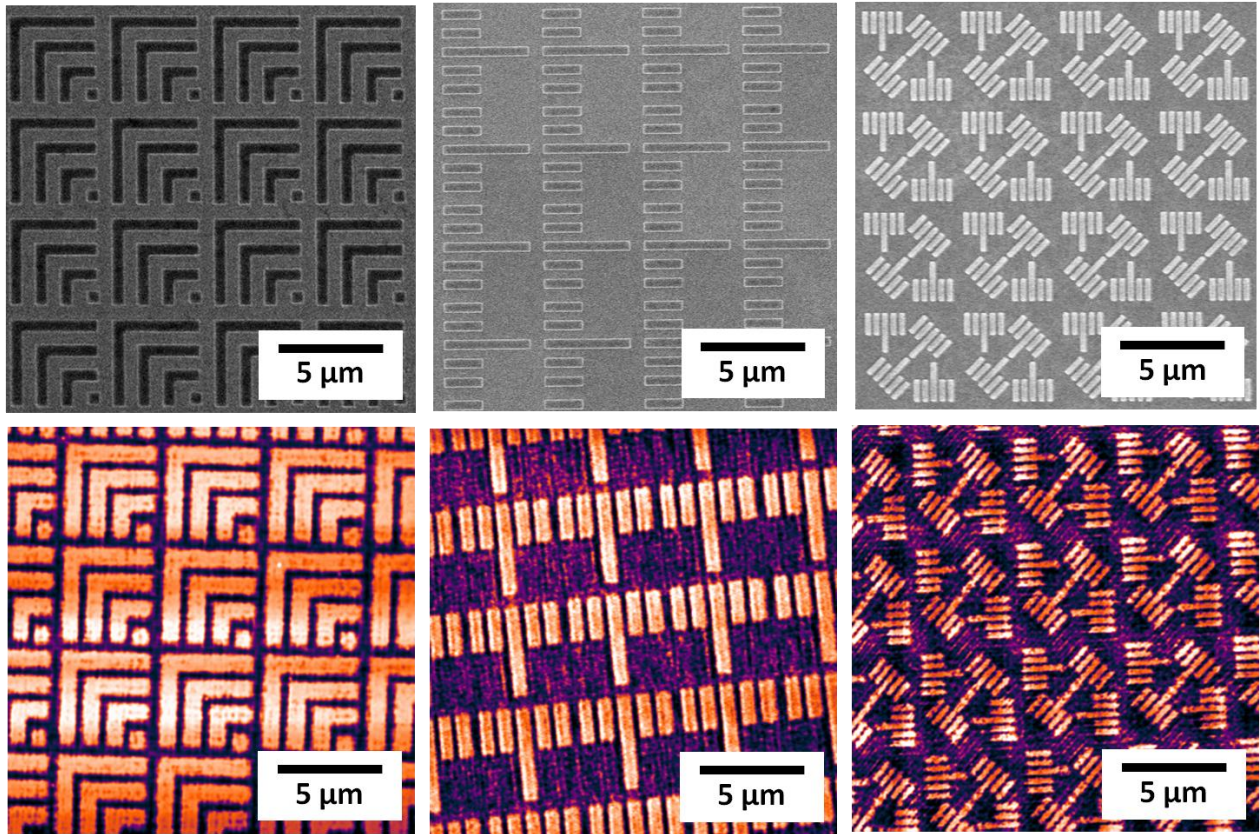


Figure 5-8. SEM micrographs of the diffractive Talbot masks (first row) accompanied by the corresponding AFM micrographs of the reconstructions (second row).

The measured resolution in the complex patterns (third column in Figure 5-8) is 126nm. The reconstruction quality is comparable with the one presented in the previous case. In the case with the mask over silicon membrane there was no observable increase in the resolution compared to the mask printed on a silicon nitride membrane. A plausible explanation to this effect is that the region of spatial coherence ($R_c=550\mu\text{m}$) is smaller than the lateral mask size in the case of both masks ($600 \times 600\mu\text{m}^2$ and $1 \times 1\text{mm}^2$). This implies that the effective region on the mask that contributes to the Talbot image creation

is limited to the area set by the coherence radius of the illumination source. In both cases, the mask area is larger than the coherence radius; consequently it does not influence the resolution of the print.

5.7 SUMMARY

In this chapter an account of self-imaging as a nanopatterning technique was provided. A theoretical treatment backed with an experimental verification was presented. The results are in very good correspondence with both analytical and numerical calculations. A comparative study of printing resolution of six masks printed on two different membranes (silicon nitride and silicon) was performed. The parameter that was varied in the analysis was the mask's lateral width. No apparent difference in the printing resolution was observed in between the mentioned cases. This is attributed to the fact that the main factor limiting the effective area that contributes to the self image is the coherence radius of the illumination. It was also expected that the silicon membranes would provide with better transmission and thus better mask contrast at the 46.9 nm wavelength. Consequently, a lower EUV exposure dose would be required for printing in the case of mask on silicon membrane. However, none such behavior was observed. This may be attributed to laser intensity variation in the two experiments.

The potential of the GTI technique lays in the advent of high average power coherent EUV and soft X-ray lasers operating at shorter wavelengths [30, 31].

5.8 REFERENCES

- [1] *Facts relating to optical science*, H.F. Talbot, *Philos. Mag.* **9**, 401 (1836).
- [2] *On copying of diffraction gratings, and on some phenomena connected therewith*, F.R.S Rayleigh, Lord, *Philos. Mag.* **11**, 196 (1881).
- [3] *The theory of sound*, F.R.S Rayleigh, Lord, and R. B. Lindsay, *Dover* (1945,1894).
- [4] *Fourier images: II - the out-of-focus patterns*, J.M. Cowley and A.F. Moodie, *Proc. Phys. Soc. B*, **70**, 497 (1957).
- [5] *Fourier images: III - finite sources*, J.M. Cowley and A.F. Moodie, *Proc. Phys. Soc. B*, **70**, 50, (1957).
- [6] *Fourier images: I - the point source*, J.M. Cowley and A.F. Moodie, *Proc. Phys. Soc. B*, **70**, 486 (1957).
- [7] *Self-imaging objects of infinite aperture*, W. D. Montgomery, *J. Opt. Soc. Am.* **57**, 772 (1967).
- [8] *Montgomery self-imaging effect using computer-generated diffractive optical elements*, J. Jahns, H. Knuppertz, and A.W. Lohmann, *Opt. Commun.* **225**, 13 (2003).
- [9] *Polychromatic self-imaging*, G. Indebetouw, *J. Mod. Optic.* **35**, 243 (1988).
- [10] *Quasi-self-imaging using aperiodic sequences*, G. Indebetouw, *J. Opt. Soc. Am. A*, **9**, 549 (1992).

- [11] Large-area patterning for photonic crystals via coherent diffraction lithography, C. Zanke, M. Qi, and H.I. Smith, *J. Vac. Sci. Technol. B*, **22**, 3352 (2004).
- [12] Talbot lithography: Self-imaging of complex structures, A. Isoyan, F. Jiang, Y. C. Cheng, F. Cerrina, P. Wachulak, L. Urbanski, J. Rocca, C. Menoni, and M. Marconi, *J. Vac. Sci. Technol. B*, **27**, 2931 (2009).
- [13] Fractional montgomery effect: a self-imaging phenomenon, A.W. Lohmann, H. Knuppertz, and J. Jahns. *J. Opt. Soc. Am. A*, **22**, 1500 (2005).
- [14] *Introduction to Fourier optics*, J.W. Goodman, McGraw-Hill (1996).
- [15] *Principles of Optics: Electromagnetic Theory of Propagation, Interference and Diffraction of Light*, M. Born, E. Wolf, A.B. Bhatia, P.C. Clemmow, D. Gabor, A.R. Stokes, A.M. Taylor, P.A. Wayman, and W.L. Wilcock, Cambridge University Press (1999).
- [16] *Center for x-ray optics database* (2009).
- [17] Demonstration of a high average power tabletop soft x-ray laser, B. R. Benware, C. D. Macchietto, C. H. Moreno, and J. J. Rocca, *Phys. Rev. Lett.*, **81**, 5804 (1998).
- [18] Generation of millijoule-level soft-x-ray laser pulses at a 4-hz repetition rate in a highly saturated tabletop capillary discharge amplifier, C. D. Macchietto, B. R. Benware, and J. J. Rocca, *Opt. Lett.* **24**, 1115 (1999).
- [19] Reflection mode imaging with nanoscale resolution using a compact extreme ultraviolet laser, F. Brizuela, G. Vaschenko, C. Brewer, M. Grisham, C. Menoni, M. Marconi, J. Rocca,

W. Chao, J. Liddle, E. Anderson, D. Attwood, A. Vinogradov, I. Artioukov, Y. Pershyn, and V. Kondratenko, *Opt. Express*, **13**, 3983 (2005).

[20] *Nanometer-scale ablation with a table-top soft x-ray laser*, G. Vaschenko, A. Garcia Etxarri, C. S. Menoni, J. J. Rocca, O. Hemberg, S. Bloom, W. Chao, E. H. Anderson, D. T. Attwood, Y. Lu, and B. Parkinson, *Opt. Lett.* **31**, 3615 (2006).

[21] *Patterning of nano-scale arrays by table-top extreme ultraviolet laser interferometric lithography*, P. W. Wachulak, M. G. Capeluto, M. C. Marconi, C. S. Menoni, and J. J. Rocca, *Opt. Express*, **15**, 3465 (2007).

[22] *Dense plasma diagnostics with an amplitude-division soft-x-ray laser interferometer based on diffraction gratings*, J. Filevich, K. Kanizay, M. C. Marconi, J. L. A. Chilla, and J. J. Rocca, *Opt. Lett.* **25**, 356 (2000).

[23] *Determination of XUV optical constants by reflectometry using a high-repetition rate 46.9-nm laser*, I.A. Artioukov, B.R. Benware, J.J. Rocca, M. Forsythe, Yu.A. Uspenskii, and A.V. Vinogradov, *Selected Topics in Quantum Electronics, IEEE Journal of*, **5**, 1495 (1999).

[24] *Demonstration of a desk-top size high repetition rate soft x-ray laser*, S. Heinbuch, M. Grisham, D. Martz, and J. J. Rocca, *Opt. Express*, **13**, 4050 (2005).

[25] *Single photon ionization of hydrogen bonded clusters with a soft x-ray laser: HCOOH_x and $\text{HCOOH}_y(\text{H}_2\text{O})_z$* , S. Heinbuch, F. Dong, J. J. Rocca, and E. R. Bernstein . *The Journal of Chemical Physics*, **126**, 244301 (2007).

[26] *Soft x-ray laser holography with wavelength resolution*, P. W. Wachulak, M. C. Marconi, R. A. Bartels, C. S. Menoni, and J. J. Rocca, *J. Opt. Soc. Am. B*, **25**, 1811 (2008).

- [27] *Single-shot extreme ultraviolet laser imaging of nanostructures with wavelength resolution*, C.A. Brewer, F. Brizuela, P. Wachulak, D.H. Martz, W. Chao, E.H. Anderson, D.T. Attwood, A.V. Vinogradov, I.A. Artyukov, A.G. Ponomareko, V.V. Kondratenko, M.C. Marconi, J.J. Rocca, and C.S. Menoni, *Opt. Lett.* **33**, 518 (2008).
- [28] *Spectral linewidth of a Ne-like Ar capillary discharge soft-x-ray laser and its dependence on amplification beyond gain saturation*, L. Urbanski, M. C. Marconi, L. M. Meng, M. Berrill, O. Guilbaud, A. Klisnick, and J. J. Rocca, *Phys. Rev. A*, **85**, 033837 (2012).
- [29] *Achromatic spatial frequency multiplication: A method for production of nanometer-scale periodic structures*, H.H. Solak and Y. Ekinici, *J. Vac. Sci. Technol. B*, **23**, 2705 (2005).
- [30] *Gain-saturated 10.9 nm tabletop laser operating at 1 hz repetition rate*, D. Alessi, D.H. Martz, Y. Wang, M. Berrill, B.M. Luther, and J.J. Rocca, *Opt. Lett.* **35**, 414 (2010).
- [31] *Demonstration of a 100 Hz repetition rate gain-saturated diode-pumped table-top soft x-ray laser*, B. Reagan, K. Wernsing, A. Curtis, F. Furch, B. Luther, D. Patel, C. Menoni, and J. Rocca, *Opt. Lett.* **37**, 3624 (2012).

CHAPTER 6 DEMAGNIFIED TALBOT IMAGING

6.1 INTRODUCTION

As it was shown in the chapter 5, GTI has a spectrum of properties that proves it as a viable approach to nanofabrication of periodic nanostructures. It has been identified as an optical, high resolution, noncontact and defect tolerant method that renders high fidelity copies of the original mask. It should be emphasized that it is possible to extend the range of attributes of the GTI even more, by introducing the size scalability of the printed features. This is achieved by adding a mirror that changes the wavefront of the illumination. In the case presented in this chapter the wavefront shaping element was a concave multilayered mirror that provides a converging beam for the diffractive mask illumination.

The size scalability in self-imaging was subject to numerous publications proposed by, among others, Cowley and Moodie, Joyeux and Cohen-Sabban [1-4]. But it was rather about adding a magnification than a demagnification system. The working principle of numerous applications, mostly for very accurate measurement of large distances, is based on the magnified self-image rendered by a periodic mask illuminated by a diverging light beam [5-7]. None of the applications described in the above references involved patterning.

This chapter describes a nanopatterning technique based on the GTI with the size scalability feature. It is defined as “demagnified generalized Talbot imaging” (DGTI), and inherits all the characteristics of the GTI mentioned in former chapters. A concise analytical description of the DGTI is provided based on the Fresnel-Kirchhoff diffraction integral. This calculation is followed by a numerical computation of the light intensity distribution behind a

periodic mask illuminated by a converging wave. Finally an experimental verification of the theoretical investigations was conducted and the results were presented and analyzed. Also the limitations of the DGTI as a patterning technique are discussed.

6.2 ANALYTICAL DESCRIPTION

Figure 6-1 shows the schematic of the DGTI set up. A collimated illumination impinges a convergent spherical mirror with a focal distance f at an angle α . In the converging beam the Talbot mask is placed at a distance s from the mirror. A photoresist coated sample is placed at the first Talbot distance, z_T from the Talbot mask. The distance from the Talbot plane and the mirror's focal plane is denoted with z .

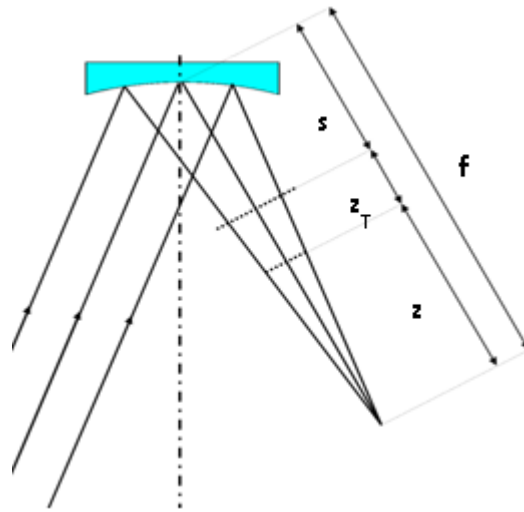


Figure 6-1. Schematic of imaging system in the DGTI experiment.

In order to provide an analytical description of the imaging system, an operator notation was used. This formalism renders results in relatively straightforward calculations. The operator notation is based on several fundamental operations from Fourier optics. Each operation is

represented by a specific "operator". The operators of interest from the standpoint of DGTI are [8, 9]:

- $Q[c]$: multiplication by a quadratic phase exponential
- $V[b]$: scaling by a constant
- $R[d]$: free space propagation.

All operators have parameters that depend on the geometry of the optical system under analysis. Parameters are included within square brackets following the operator. The operators act on the quantity in the curly brackets $\{ \}$. Let us assume a light wave with an amplitude $U(x)$ propagating from left to right. The operators on the function $U(x)$ are defined as follows:

Multiplication by a quadratic-phase exponential.

$$Q[c]\{U(x)\} = e^{i\frac{k}{c}x^2} U(x) \quad (1)$$

Where c is the wavefront curvature, x is the coordinate in lateral direction, k is the modulus of the wave vector defined as $k=2\pi/\lambda$, λ is the wavelength of illumination.

Scaling by a constant b .

$$V[b]\{U(x)\} = |b|^{1/2} U(bx) \quad (2)$$

Free-space propagation of a distance d .

$$R[d]\{U(x_1)\} = \frac{1}{\sqrt{i\lambda d}} \int_{-\infty}^{\infty} U(x_1) e^{i\frac{k}{2d}(x_2-x_1)^2} dx_1 \quad (3)$$

These operators are sufficient for analyzing the optical system applied for DGTI. Their utility arises from some simple properties and certain relations between them, which are showed below [9].

$$R[d] \cdot Q[c] = Q[(c^{-1} + d)^{-1}] \cdot V[(1 + cd)^{-1}] \cdot R[(d^{-1} + c)^{-1}] \quad (4)$$

And

$$\left\{ V[t] \cdot R[d] = R\left[\frac{d}{t^2}\right] V[t] \right\} \quad (5)$$

Let the operator S denote the entire transformation represented by the optical system. From the Figure 6-1, it can be seen, that in the operator notation, there is a quadratic phase term gained upon the reflection from the mirror (operator $Q[1/z]$), and a free space propagation by the distance $z_T=f-s-z$ (operator $R[f-s-z]$). The Operator S then takes the following form:

$$S = R[f-s-z] \cdot Q\left[\frac{1}{z}\right] \quad (6)$$

After applying the relation given by equation 4, we can rewrite equation 6 in the following form:

$$S = Q\left[\frac{1}{(f-s)}\right] \cdot V\left[\frac{z}{(f-s)}\right] \cdot R\left[\frac{(f-s-z)z}{(f-s)}\right] \quad (7)$$

Now, by applying relation 5 to equation 7, one obtains:

$$S = Q\left[\frac{1}{(f-s)}\right] R\left[\frac{(f-s-z)z(f-s)^2}{(f-s)z^2}\right] V\left[\frac{z}{(f-s)}\right] \quad (8)$$

After a couple of reductions equation 8 becomes:

$$S = Q\left[\frac{1}{(f-s)}\right] R\left[\frac{(f-s-z)(f-s)}{z}\right] V\left[\frac{z}{(f-s)}\right] \quad (9)$$

By applying definitions of the operators introduced originally we obtain:

$$S = \sqrt{\frac{z}{f-s}} \frac{z}{i\lambda(f-s-z)(f-s)} e^{i\frac{k}{z}x_2^2} \cdot \int_{-\infty}^{\infty} U\left(x_1 \frac{z}{f-s}\right) \exp\left[-ik \frac{z(x_2-x_1)^2}{(f-s-z)(f-s)}\right] dx_1 \quad (10)$$

The first term in the equation 10 does not contribute to the spatial profile of the light intensity distribution and serves as normalizing factor. The integrand can be then viewed as two terms: the first one is responsible for demagnification in the image. The aforementioned quantity depends on the mirror-mask distance s . The second term describes the propagation with the phase acquired by reflection from a concave mirror. From equation 10 one can calculate the Talbot distance in the following way:

$$z_T = \frac{(f-s-z)(f-s)}{z} = 2 \frac{Mp^2}{\lambda} \quad (11)$$

After some algebraic transformation (see Appendix 1), equation 11 can be reduced to the following form:

$$z_T = \frac{2Mp^2(f-s)}{2Mp^2 + (f-s)\lambda} \quad (20)$$

Equation 20 defines the Talbot distance in the demagnified Talbot imaging configuration. One can see that there is a correction factor, which takes into consideration the mirror-mask distance. This factor is of little significance as long as the mirror-mask distance is smaller than focal length of the mirror. This can be observed calculating the limit of this rational function of $(f-s)$ at infinity

$$\lim_{(f-s) \rightarrow \infty} \frac{2Mp^2(f-s)}{2Mp^2 + (f-s)\lambda} = \frac{2Mp^2}{\lambda} \quad (21)$$

This simple calculation shows that far from the focus, when $f \gg s$, the DGTI Talbot distance reduces to the same relation obtained in the classical Talbot imaging. However, once the mirror-mask distance is comparable with the focal length of the mirror, the Talbot distance decreases fast to zero with increasing $(f-s)$. This fact is the main limitation of the maximum demagnification achievable in the system and also its diffraction limited resolution. A detailed discussion of these limitations will be presented later in this chapter.

6.3 NUMERICAL SIMULATION

Using an approach similar to the one described in the chapter 5, the light intensity distribution behind a periodic structure illuminated with a convergent beam can be numerically calculated by solving the Fresnel-Kirchhoff integral behind the diffractive mask. Practically this is completed by applying fast Fourier transforms. The solution is calculated in the y - z plane. The abscissa axis marks the distance along the propagation axis z whereas the ordinate axis y marks the lateral dimension of the diffractive mask. The light intensity is plotted in pseudo-color scale. As explained in the chapter 5, such intensity plot is often referred to as the Talbot carpet.

In the case of GTI, the numerical solution is calculated for a plane wave. Whereas in the case of DGTI a quadratic phase term is added in order to represent an extra phase gained upon the reflection from a curved mirror. The case of a Talbot carpet calculated numerically for DGTI is shown in Figure 6-2. The lateral periodicity of the light distribution behind the periodic mask can be readily seen on the plot. As the light converges towards the focus, the spacing between adjacent Talbot planes decreases causing them to blur completely at the focus. A transformation from near field to far field imaging is observed once the light wave arrives to the focal point. At the focal plane the far field image of the diffracting mask appears in the form of diffracted

orders. It should be emphasized, that the shape of the Talbot planes changes along the optical axis. Closer to the focus, the Talbot planes become rather Talbot surfaces. This behavior is a limiting factor in the printing process.

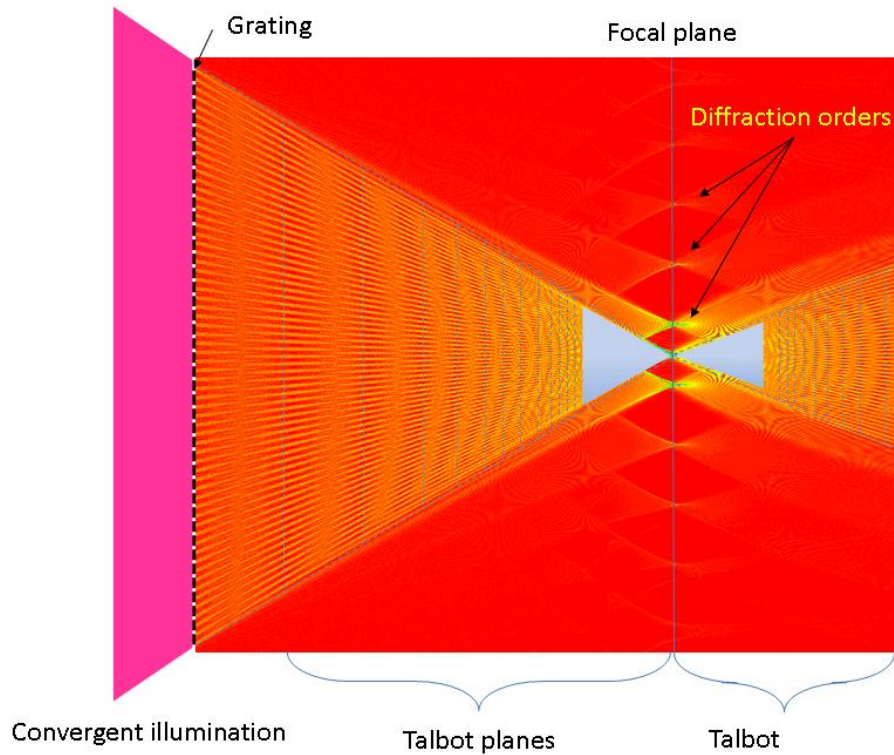


Figure 6-2. Numerically calculated Talbot carpet for the case of a periodic structure illuminated with a converging beam. On the left, the diffractive mask is indicated by the black dashed line, the Talbot planes are indicated by blue dashed lines.

6.4 DGTI EXPERIMENT

An experimental verification of the analytical and numerical calculations was performed. In the Figure 6-3, there is a schematic (6-3a) and a picture (6-3b) of the actual setup. In this experiment, coherent extreme ultraviolet (EUV) light at 46.9nm was used for illumination. The light source was a capillary discharge, table-top laser [10, 11]. More detailed description of the light source,

its working principle and light parameters is included in the chapter 2. The EUV laser impinges on a spherical multilayered mirror that focuses the beam and simultaneously provides an extra spectral filtering. The mirror has a reflectivity of approximately 40% at the incidence angle of 18° .

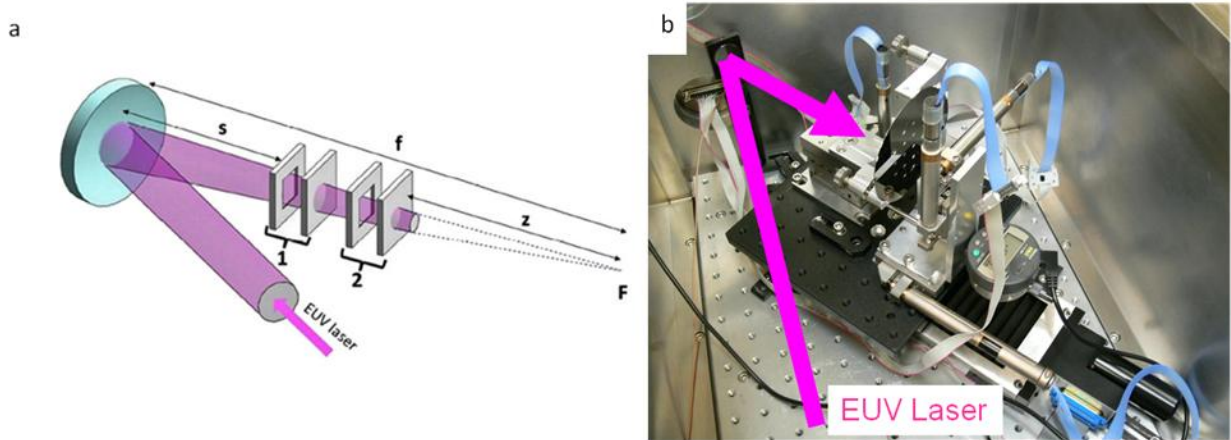


Figure 6-3. Scheme and picture of the experimental set up. Frame a) shows the set mask-sample is placed at different distances (s), from the focusing mirror. Solidly moving these two elements along the optical axis of the mirror (positions 1 and 2 in the Figure 6-3a) allows for printing with different demagnification factors. Figure 6-3b is the picture of actual setup used.

After the mirror, the Talbot mask and the sample coated with photoresist were placed in a translation stage which allows for moving the set mask-sample along the optical axis of the mirror. The relative distance between the mask and the sample was actuated using an optical stage. Moreover, the stage where the sample was mounted on had the possibility to move in x - y plane, providing for multiple exposures on one sample. The distance between the Talbot mask and the sample was adjusted for the first Talbot plane, in this case $\sim 1000 \mu\text{m}$. The sample was a 0.5 mm thick silicon wafer covered with $\sim 100 \text{ nm}$ thick layer of poly-methyl-methacrylate

(PMMA) resist. The resist was deposited by spin coating. The recording of the resist required an exposure of approximately 300 shots. The laser was set to operate at 1 Hz, yielding an exposure time of 5 min in order to record a single image.

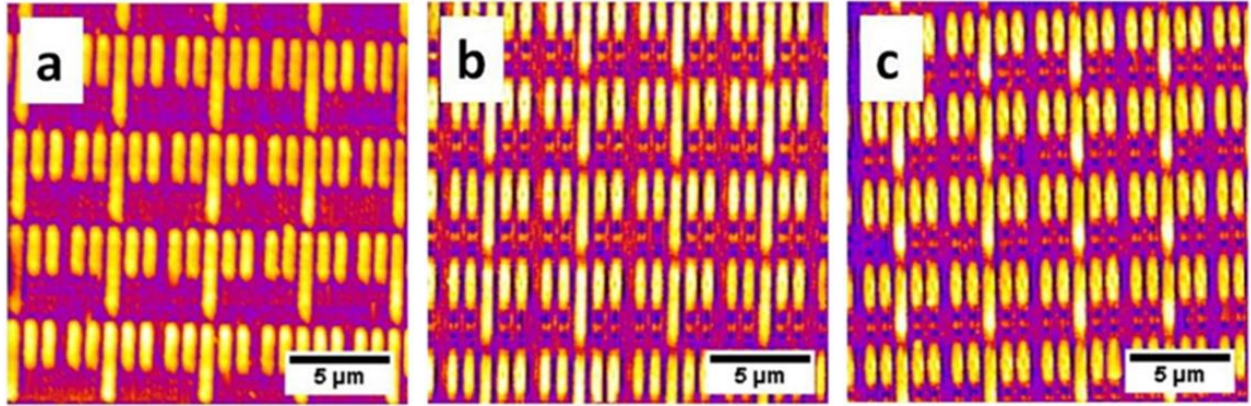


Figure 6-4. AFM scans of the prints obtained at different distances from the focusing mirror. The period decreases when the set mask-sample moves towards the focus. The de-magnification factors and distances measured from the focusing mirror are: (a) $\delta_{M1} = 0.97$, $d_1 = 22$ cm, (b) $\delta_{M2} = 0.89$, $d_2 = 24.4$ cm, and (c) $\delta_{M3} = 0.87$, $d_3 = 24.5$ cm.

After exposure, the samples were post processed in accord with the description provided in the appendix 2. Figure 6-4 shows the images of the prints obtained at different positions along the optical axis of the mirror. The set mask-sample was solidly moved along the path of the converging beam to distances of $d_1 = 22$ cm, $d_2 = 24.4$ cm, and $d_3 = 24.5$ cm from the mirror. The demagnification factor, δ is the ratio of the period of the printed structure to the mask period. These distances yield calculated de-magnification factors of $\delta_1 = 0.96$, $\delta_2 = 0.85$, and $\delta_3 = 0.82$, respectively. The scan size of all images is $20 \times 20 \mu\text{m}^2$. From the AFM images, the period of the structures was measured to be $p_1 = 4.69 \mu\text{m}$, $p_2 = 4.35 \mu\text{m}$, and $p_3 = 4.24 \mu\text{m}$, yielding to measured de-magnification factors, $\delta_{M1} = 0.97$, $\delta_{M2} = 0.89$, and $\delta_{M3} = 0.87$, respectively.

Table 6-1 summarizes the results of this experiment, comparing the calculated and measured demagnification factors

Table 6-1. Summary of the calculated measured values of demagnification

<i>Calculated Demagnification</i>	<i>Measured Demagnification</i>
0.96	0.980
0.86	0.887
0.82	0.865

The discrepancy between the measured and calculated demagnification values may stem from three facts. One of them being the measurement error of the s distance, that in our set up was estimated to be (± 1 mm). This source of error is the most prominent in the case presented. As can be inferred from the Figure 6-5, one millimeter of variation in the distance corresponds to very dramatic change in the demagnification factor ($\sim 10\%$). Another, less significant source of error is due to the variation in the effective focal length of the mirror. This effect is the consequence of the natural divergence of the illumination beam (~ 5 mrad), which gives ~ 30 μm of the focus displacement and thus contributes another $\sim 0.3\%$ to the absolute variation in the demagnification factor. The third possible source of error are the variable conditions of scanning the prints in photoresist with the AFM. The AFM is extremely susceptible to the ambient conditions such as acoustic and electromagnetic noise, building vibrations, temperature, atmospheric pressure and humidity. The contribution of this error to the absolute value of the measured δ is of the order of 0.01% . The scans were also taken with different probes, which although from the same batch

differ in the resonance frequency and tip radii. Considering these three factors, the calculated and measured values are within the experimental errors.

Figure 6-5, illustrates two prints in resist obtained using the GTI and the DGTI configurations for comparison purposes. The frame 5a shows reconstruction of a periodic mask in GTI setup. As mentioned in chapter 5, this scheme for nanopatterning uses illumination with a plane wavefront. Frame 5b, shows the same mask reconstructed using the DGTI technique. The demagnification factor for this case is $\delta=0.8$.

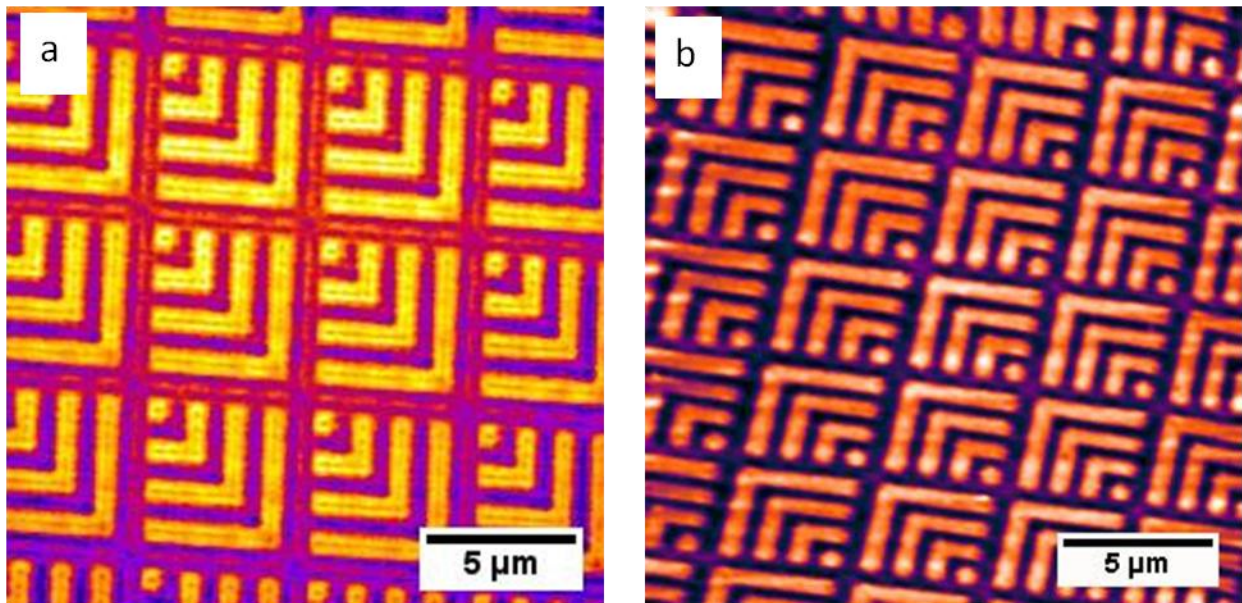


Figure 6-5. Comparison of reconstruction obtained using GTI, shown in the inset 8a and DGTI (Figure 6-5b). Image distortion observable due to mirror's spherical aberration. Figure 6-5 is adopted from [12].

In the print illustrated in the Figure 6-5b, there is a slight image distortion observed. This is attributed to artifacts introduced by the AFM.

The dependence of the demagnification with the distance from the mirror can be derived from equation 10. As the first term of the integrand in equation 10 indicates, the demagnification of the original periodic structure is:

$$\delta = \frac{z}{f-s} = \frac{f-s-z_T}{f-s}. \quad (22)$$

Substituting the expression for the Talbot distance in DGTI (equation 20) one obtains:

$$\delta = \frac{f-s - \frac{2Mp^2(f-s)}{2Mp^2 + (f-s)\lambda}}{f-s} = 1 - \frac{2Mp^2}{2Mp^2 + (f-s)\lambda} \quad (23)$$

It can be seen from equation 23 that the value of demagnification changes very rapidly when $f-s$ approaches 0, or in other words, the mirror-mask distance is approaching the focal length.

The dependence of the demagnification factor as a function of normalized mirror-mask distance is shown in the Figure 6-6. The solid curve is the analytical expression; the red circles are the experimental data points.

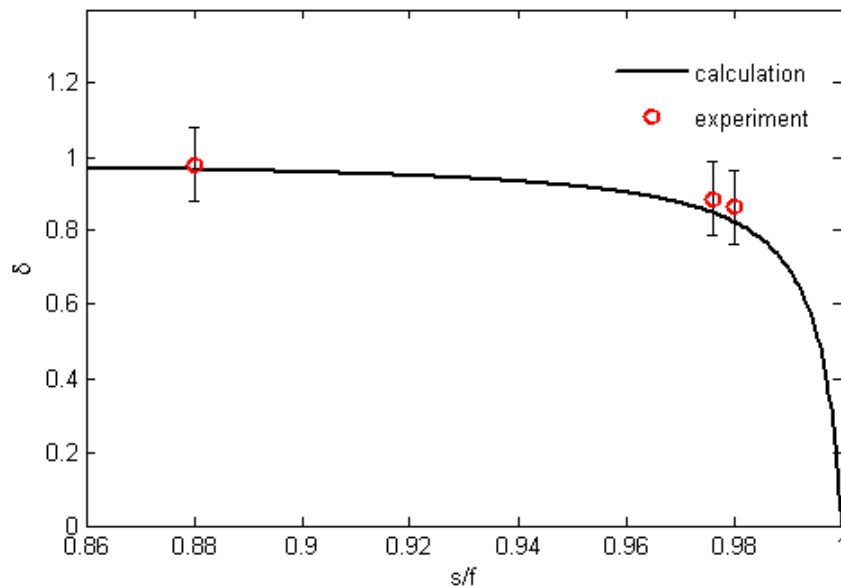


Figure 6-6. Demagnification factor, δ , as a function of the normalized distance, s/f . The solid curve corresponds to the predicted values according to the Fresnel-Kirchhoff theory and the red circles correspond to the measured values.

The graph shows that the demagnification changes very little throughout almost all of the range of s , and only very close to the focus ($s/f = 1$), does the dependence become more pronounced.

6.5 LIMITATIONS

The limitation on the printing resolution comes from the fact that the Talbot distance is dependent on the mirror-mask distance. Its influence can be understood from the expression of the NA in the case of the DGTI. As in any optical system the resolution of the image is limited by the optical system's NA

Using the expression for the numerical aperture (derived in the chapter about the GTI):

$$NA = \left(\sqrt{1 + \left(\frac{Mz_T}{W} \right)^2} \right)^{-1} \quad (24)$$

By substituting the expression for the Talbot distance given by equation 20 into equation 24 one obtains:

$$NA = \left[\sqrt{1 + \left(\frac{2(f-s)p^2Mf}{(2p^2M + \lambda(f-s))(f-d-s)W} \right)^2} \right]^{-1} \quad (25)$$

Equation 25 is the expression for the numerical aperture in demagnified Talbot imaging.

Using the relation for diffraction limited resolution:

$$\Delta = 0.61 \frac{\lambda}{NA} \quad (26)$$

And substituting the expression for NA, derived in equation 25 one obtains:

$$\Delta = 0.61\lambda \left[\sqrt{1 + \left(\frac{2(f-s)p^2Mf}{(2p^2M + \lambda(f-s))(f-d-s)W} \right)^2} \right] \quad (27)$$

In the Figure 6-7 a plot of the resolution as a function of normalized mirror-mask distance (equation 25) is illustrated. It shows the resolution Δ as a function of the normalized mirror-mask distance s/f . Each curve represents the calculation for a different Talbot order indicated in the legend.

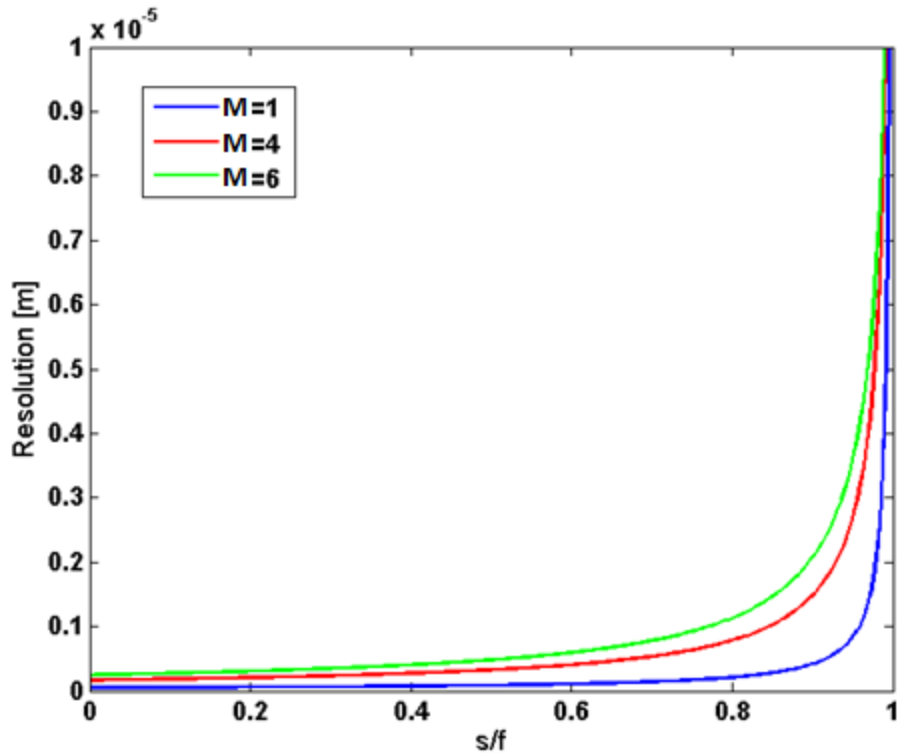


Figure 6-7. Diffraction limited resolution in DGTI printing as a function of normalized mirror-mask distance s/f .

From the plot in the Figure 6-7 it is also evident that the resolution also degrades with increasing the Talbot order. Figure 6 8 shows simultaneously the plots of the demagnification factor and the resolution as the functions of normalized mirror-mask distance. The purpose of this graph is to show, the trade-off between the demagnification factor and the resolution. If one extends the mirror-mask distance in order to achieve high demagnification, the size of the smallest printable feature increases rapidly (or the resolution worsens). The intersection of the characteristics shown in the Figure 6 8 determines the optimum working conditions, i.e. maximum possible demagnification with best possible resolution. In DGTI, the highest resolution attainable is set by

the diffraction limit. It is resultant from the periodic mask's NA and illumination wavelength (equation 26).

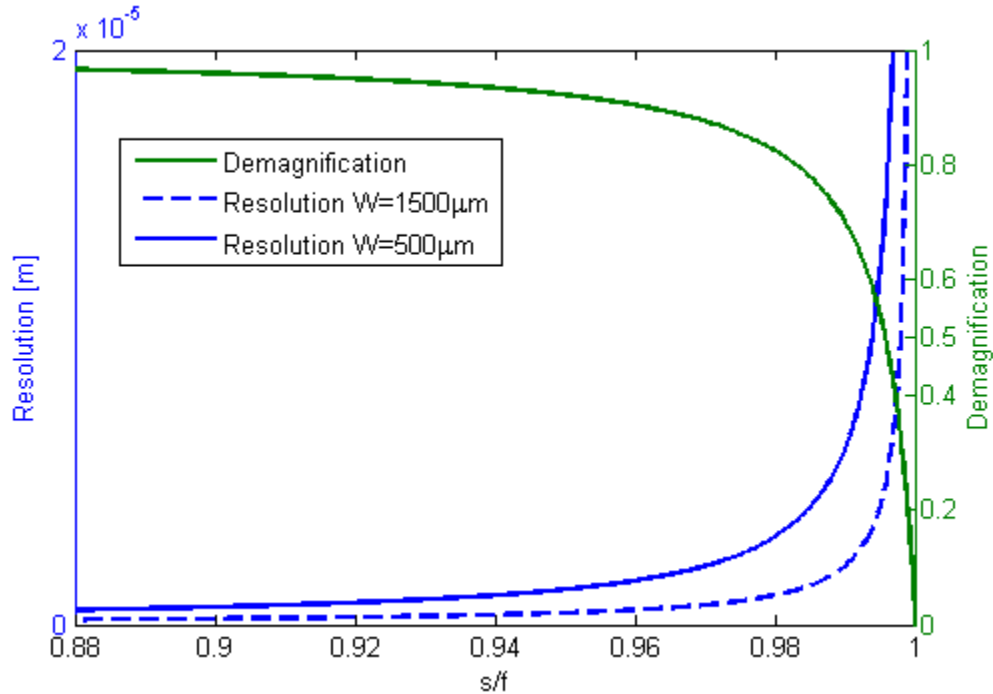


Figure 6-8. Resolution and demagnification in DGTI experiment plotted together.

In the case from the experimental arrangement, the value of diffraction limited resolution is 67nm. However, this resolution can be achieved when the values of s/f are small (i.e. the mask-sample set is placed far away from the focus). Thus at the loci where the resolution is the best, (i.e. far away from the focal point), the demagnification factor is close to 1, meaning no practical demagnification. The mentioned argument, which follows from the Figure 6-8, shows that the DGTI method is self limiting.

One possible way to improve this situation is to fabricate a diffractive mask providing with high numerical aperture (small elementary cell repeated over large area, *conf.* equation 24).

This wouldn't change the overall behavior of the resolution and demagnification factor as the functions of the normalized mirror-mask distance, however, the absolute value of the minimum printable feature (resolution), at which the intersection occurs, would be smaller. This situation is presented on the Figure 6-8, where resolution for two different mask lateral sizes (and consequently NAs) is plotted. Supposedly, there are two masks with different areas; one occupies a $500\mu\text{m} \times 500\mu\text{m}$ square, the other $1500\mu\text{m} \times 1500\mu\text{m}$. The dashed line in the Figure 6-8 represents the resolution for the smaller mask, whereas the solid blue line on the same figure is a plot of resolution for the larger mask. The plot of the demagnification factor (solid green curve) is identical for both cases, as it does not depend on the mask size. It can be readily noticed, that the intersection of the resolution plotted for those two instances occurs at different demagnification values. For the case of $500\mu\text{m} \times 500\mu\text{m}$ mask the absolute values of resolution and demagnification are $8\mu\text{m}$ and 65% respectively. In the case of $1500\mu\text{m} \times 1500\mu\text{m}$ mask, the values of resolution and demagnification are $6\mu\text{m}$ and 40% respectively. Thus, it can be seen that increasing the mask's area helps to provide for better resolution and smaller maximum demagnification factor simultaneously.

6.6 SUMMARY

In summary, in this chapter the DGTI technique was analyzed. The analytical description for the DGTI scheme was provided, which was later corroborated with numerical computation. An analytical expression for the light intensity distribution after a diffractive mask was calculated using Fresnel-Kirchhoff diffraction integral employing elements of the operator notation. Independently, a numerical computation of the light intensity distribution behind the Talbot mask was carried out. The numerical result was obtained by solving the Fresnel-Kirchhoff integral on the y - z plane at each point behind a diffractive mask illuminated by a converging

wave. The calculations were followed by an experimental verification. In the experimental arrangement the DGTI method utilizes only a periodic mask and a focusing mirror, which makes the setup practical and simple to implement at EUV wavelengths. The main advantage of the DGTI technique lays in the feasibility to seamlessly tune the pitch of the printed pattern. This feature is favorable in fabrication of nanostructures such as metamaterials [13], as it allows for the analysis of their properties as a function of their continuously variable size. The demagnification factors attainable are however modest (maximum obtained experimentally: ~15%). There is a tradeoff between the system's resolution and demagnification factor, which is inherent to the imaging scheme and limits the maximal demagnification obtained. One possible approach to solve this problem is to use large NA diffractive mask that provides with high resolution. The experimental work together with part of the analytical description, presented in this chapter were published in [14].

6.7 REFERENCES

- [1] *Fourier images: I - the point source*, J.M. Cowley and A.F. Moodie, *Proc. Phys. Soc. B*, **70**, 486 (1957).
- [2] *Fourier images: II - the out-of-focus patterns*, J.M. Cowley and A.F. Moodie, *Proc. Phys. Soc. B*, **70**, 497 (1957).
- [3] *Fourier images: III - finite sources*, J.M. Cowley and A.F. Moodie, *Proc. Phys. Soc. B*, **70**, 50, (1957).
- [4] *High magnification self-imaging*, D. Joyeux and Y. Cohen-Sabban, *Appl. Opt.* **21**, 625 (1982).
- [5] *Novel method for testing the long focal length lens of large aperture*. C.L. Hou, J. Bai, X.Y. Hou, C. Sun, and G.G. Yang. *Opt. Laser. Eng.* **43**, 1107 (2005).
- [6] *Range Measurement Using Talbot Diffraction Imaging Of Gratings*, P. Chavel and T.C. Strand. *Appl. Opt.* **23**, 862 (1984).
- [7] *The Self-Imaging Phenomenon And Its Applications*, K. Patorski, *Prog. Optics*, **27**, 3 (1989).
- [8] *Fourier optics described by operator algebra*, M. Nazarathy and J. Shamir, *J. Opt. Soc. Am*, **70**, 150 (1980).
- [9] *Introduction to Fourier optics*, J.W. Goodman, *McGraw-Hill series in electrical and computer engineering*. McGraw-Hill (1996).

- [10] *Demonstration of a high average power tabletop soft x-ray laser*, B. R. Benware, C. D. Macchietto, C. H. Moreno, and J. J. Rocca, *Phys. Rev. Lett.*, **81**, 5804 (1998).
- [11] *Generation of millijoule-level soft-x-ray laser pulses at a 4-hz repetition rate in a highly saturated tabletop capillary discharge amplifier*, C. D. Macchietto, B. R. Benware, and J. J. Rocca, *Opt. Lett.* **24**, 1115 (1999).
- [12] *Talbot lithography: Self-imaging of complex structures*, A. Isoyan, F. Jiang, Y. C. Cheng, F. Cerrina, P. Wachulak, L. Urbanski, J. Rocca, C. Menoni, and M. Marconi, *J. Vac. Sci. Technol. B*, **27**, 2931 (2009).
- [13] *Ultrasmooth Patterned Metals for Plasmonics and Metamaterials*, P. Nagpal, N.C. Lindquist, S.H. Oh, and D. J. Norris, *Science*, **325**, 594 (2009).
- [14] *Analysis of a scheme for de-magnified talbot lithography*, L. Urbanski, M. C. Marconi, A. Isoyan, A. Stein, C. S. Menoni, and J. J. Rocca, *J. Vac. Sci. Technol. B*, **29**, 06F504 (2011).

CHAPTER 7 DEFECT TOLERANT GENERALIZED TALBOT IMAGING

7.1 INTRODUCTION

In this chapter the defect tolerance property of the generalized Talbot imaging (GTI) is studied. GTI is a technique based on the self-imaging effect that occurs when a periodic semi-transparent mask is illuminated with coherent light [1]. A detailed discussion of the GTI nanopatterning technique is found in chapter 5. The concept of defect tolerance was introduced by Dammann in [2]. In his work he proved that a defect deliberately introduced to a periodic mask will disappear at the copy rendered by self-imaging. In his paper a periodic mask (originally a vidicon device) was scratched and subsequently illuminated by coherent light. The replica resultant due to self-imaging effect was devoid of the presence of defect. A similar case was presented by Lohmann in [3]. He was testing the defect influence on the self-images produced by Ronchi gratings used as array illuminators.

In the case presented in this chapter, a study of the image quality in GTI as a function of the defect density was conducted. The extent of defect tolerance was examined by means of an analytical description. Further it was corroborated with a numerical simulation. Ultimately, the degree of defect tolerance in the GTI technique was experimentally verified. To explore the extent of defect tolerance, masks with different defect layouts and concentration were designed. The cell shape was chosen to be arbitrary, for this test we selected a motif from the classic videogame “The Space Invaders”. The defect was of the form of an alien cell introduced as an impostor of the native one. The experimental results are in good agreement with theoretical analysis.

7.2 ANALYTICAL DESCRIPTION

One convenient way to describe the Talbot effect is in the spatial frequency domain. The derivation presented here follows closely Lohmann's [10]. The derivation is similar to the one carried out in chapter 5 for the GTI description.

Let us introduce a periodic structure with a transmission function given by $U_T(x)$. This is a general prescription for a mask composed of arbitrary shape arranged periodically. For brevity, the analysis is done for only one dimension; however it can easily be extended to a plane.

$$U_T(x) = U_T(x+p) = \sum_m A_m \exp\left(2\pi i m \frac{x}{p}\right). \quad (1)$$

Where A_m is the m -th order Fourier series coefficient, p is the period of the mask and x is the spatial coordinate in the direction transverse to the direction of propagation. The corresponding spatial frequency spectrum can be calculated using the Fourier transform and is given by:

$$\int U_T(x) \exp(-2\pi i \nu x) dx = \tilde{U}_T(\nu) = \sum_m A_m \delta(\nu - m\nu_0). \quad (2)$$

Where the frequency ν_0 is the inverse of the period of the mask.

$$\nu_0 = \frac{1}{p}. \quad (3)$$

Immediately behind the mask, the field can be described by:

$$U(x,0) = U + \sum_{m \neq 0} A_m \exp(2\pi i m x \nu_0) = A_0 + u(x,0). \quad (4)$$

For convenience, the 0-order term denoted by U is dealt with separately. Consequently, the spatial frequency spectrum will take the form:

$$\tilde{U}(\nu,0) = A_0 \delta(\nu) + \sum_{m \neq 0} A_m \delta(\nu - m\nu_0) = A_0 \delta(\nu) + u(\nu, z=0). \quad (5)$$

The space propagation of the spatial frequency spectrum is equivalent to a multiplication by a quadratic phase term, which in the paraxial approximation takes the following form:

$$\exp(-i\pi\lambda z v^2) = \exp(-i\pi\lambda z m^2 v_0^2), \quad (6)$$

Where z denotes the direction of propagation. Substituting equation 6 into equation 5 yields:

$$\begin{aligned} \tilde{U}(v, z) &= A_0\delta(v) + \sum_{m \neq 0} A_m \exp(-i\pi\lambda z m^2 v_0^2) \delta(v - m v_0) \\ &= A_0\delta(v) + u(v, z). \end{aligned} \quad (7)$$

A simple substitution in equation 8 defines the Talbot distance z_T

$$-i\pi\lambda z m^2 v_0^2 = -2i\pi m^2 \frac{z}{z_T}, \quad z_T = \frac{2}{\lambda v_0^2} = \frac{2p^2}{\lambda}. \quad (8)$$

Equation 5 can be then rewritten to the following form:

$$\tilde{U}(v, z) = A_0\delta(v) + \sum_{m \neq 0} A_m \exp\left(-2i\pi m^2 \frac{z}{z_T}\right) \delta(v - m v_0). \quad (9)$$

Equation 9 is transformed back to spatial domain to obtain:

$$U(x, z) = A_0 + \sum_{m \neq 0} A_m \exp\left[-2i\pi\left(mv_0x - m^2 \frac{z}{z_T}\right)\right] = U(x, z + Nz_T) \quad (10)$$

From this equation it can be seen that the field distribution has a periodic character also along the z direction.

In the case of a diffracting periodic mask with a defect, similar analysis can be done.

Introducing $D(x)$ as the contribution from a defect, the total field amplitude will be:

$$U_{TOT}(x) = D(x) + \sum_m A_m \exp\left(2\pi i m \frac{x}{p}\right). \quad (11)$$

Using the same Fourier formalism described before, immediately after the mask the field is equal to:

$$\begin{aligned}\tilde{U}_{TOT}(\nu, z=0) &= d(\nu, z=0) + A_0\delta(\nu) + \sum_{m \neq 0} A_m\delta(\nu - m\nu_0) \\ &= d(\nu, z=0) + A_0\delta(\nu) + u(\nu, z=0).\end{aligned}\quad (12)$$

Where $d(\nu, z=0)$ is the spatial frequency spectrum of the defect. By analogy to equations 7-9, the resulting intensity distribution in the spatial frequency domain can be rewritten to the following form:

$$\tilde{U}_{TOT}(\nu, z) = d(\nu, 0) + A_0\delta(\nu) + \sum_{m \neq 0} A_m \exp\left(-2i\pi m^2 \frac{z}{z_T}\right) \delta(\nu - m\nu_0). \quad (13)$$

Thus transferring it to the spatial domain, we obtain:

$$\begin{aligned}U_{TOT}(x, z) &= D(x, z) + \sum_{m=0} A_m \exp\left[-2i\pi\left(m\nu_0 x - m^2 \frac{z}{z_T}\right)\right] \\ &= D(x, z) + U(x, z + Nz_T).\end{aligned}\quad (14)$$

In equation 14, the first and second term can be identified as contributions from the defect and the intact part of the mask respectively. Equation 14 addresses the question of defect tolerance twofold. First, a localized defect in the mask does not have periodic character along the axis of propagation. The light emerging from the defect doesn't undergo periodic revivals, rather decreases with the propagation distance. Secondly, the contribution from the defect is an additive term that can be assumed proportional to the ratio of areas of the defect to the entire mask. Thus, the area of the defect being small compared to the area of the entire mask will result in excluding

the defect at the reconstruction plane. If there is a local defect in the mask, the diffracted field contributing from it will be of relatively small input to the total intensity distribution at the Talbot plane. Thus, the defect will not be apparent at the reconstruction plane.

7.3 NUMERICAL SIMULATION

To corroborate the analytical solution numerical simulations were realized. A detailed description of the discrete Fresnel-Kirchhoff integral and its numerical solution is presented in the chapter 4. The input to the numerical model is the file that was used to fabricate the actual mask. The periodic mask was created by tiling 10^4 cells in a square lattice. The cell was chosen to be a completely arbitrary motif, in our case the profile of a "Space Invader", a character from a classic video game. The defect embedded in the periodic mask was of a form of another (alien) species of "Space Invader" that replaces the native one. The mask with these characteristics was used to calculate the self-image formed at the first Talbot plane. Figure 7-1 shows the output of the simulation. Frame 1a pictures the central part of the mask where a single cell was replaced by a defect (impostor cell). The image in the frame 1b is the calculated intensity distribution at the first Talbot plane. Likewise, frame 1c pictures the central part of the mask where the middle row of cells was replaced by a row of defects. The image in the frame 1d is the resultant intensity distribution at the first Talbot plane. In both cases, the defects are not present in the reconstruction.

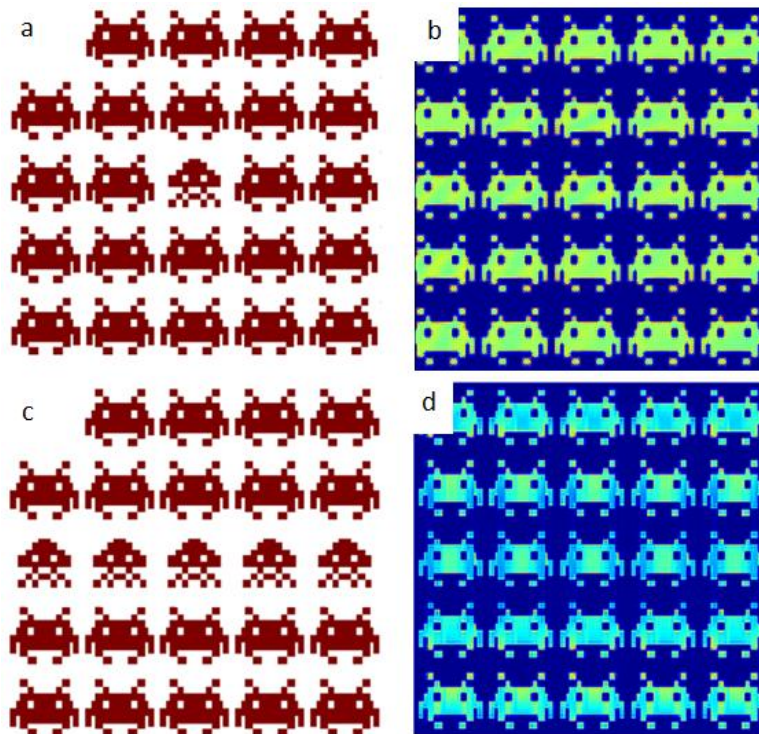


Figure 7-1. Numerical simulation of the defect tolerant generalized Talbot imaging. a) Central section of a mask composed of 100×100 cells with arbitrary motif in which a “defect” (a single cell with different motif). b) Reconstruction of a at the first Talbot plane. Inset c) - central section of a mask with entire row of impostor cells, d) – numerical reconstruction of c).

This calculation shows that the reconstruction of the mask with a defect will be rendered defect free at the Talbot planes. This characteristic of the Talbot imaging is of significance when GTI is applied to nanopatterning, because the mask copying process is error tolerant.

7.4 EXPERIMENTAL VERIFICATION OF DEFECT TOLERANCE

This section of the chapter describes the experimental verification of the defect tolerance in the GTI. The design of the masks with controlled amount of defects, the experimental setup and the experimental results are discussed in this section of the chapter.

7.4.1 MASK DESIGN

Five Talbot masks with different defect concentration and layout were fabricated using electron beam lithography. The details on the mask fabrication can be found in the chapter 3 and appendix 2. A significant question to address is: what is influence of the amount of defect in a mask and its location in the mask on the self-image deterioration. All mask designs used in the experiment are summarized in the table 7-1.

Table 7-1. Defect tolerant mask design summary

<i>Mask number</i>	<i>Defect layout</i>	<i>Defect concentration</i>	<i>Defect quantity</i>
1	Localized - center	0.01%	1
2	Localized - middle row	1%	100
3	Random	5%	500
4	Random	10%	1000
5	Random	20%	2000

The mask was designed as a periodically tiled set of arbitrary shaped cells in a square lattice. The primitive cell size is $5 \times 5 \mu\text{m}^2$ resulting in a Talbot distance of 1mm for the wavelength of illumination of 46.9nm. The entire mask is formed by of 100×100 cells. The defects were planted by substituting the native motif by a completely different one. To investigate on the extent of defect tolerance, five different arrangements of defects were applied. In the first case, a single impostor cell was planted in the middle of the mask, yielding the size ratio of the defect to the entire mask of 0.01%. In the second case, an entire row of native cells was replaced by a row of the impostor motif yielding the defect to mask ratio of 1%. In the cases from 3 to 5 impostor cells were distributed randomly across the mask with the following concentrations: 5%, 10% and 20%.

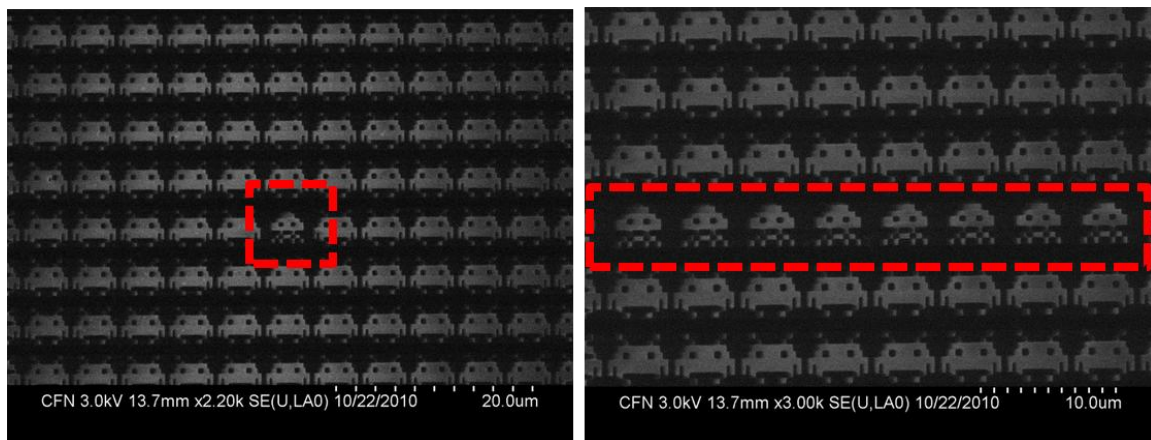


Figure 7-2. Talbot masks with 0.01% (left) and 1% (right) defect.

This high density of defects however unrealistic in the practical lithography arrangement gives an account of the extent of defect tolerance in GTI based printing. In the Figure 7-2, the SEM micrographs of masks 1 and 2 are depicted. The defects are framed for better visibility. SEM

images of masks (3-5) containing randomly distributed defects at different concentrations are illustrated on Figure 7-3 (right column).

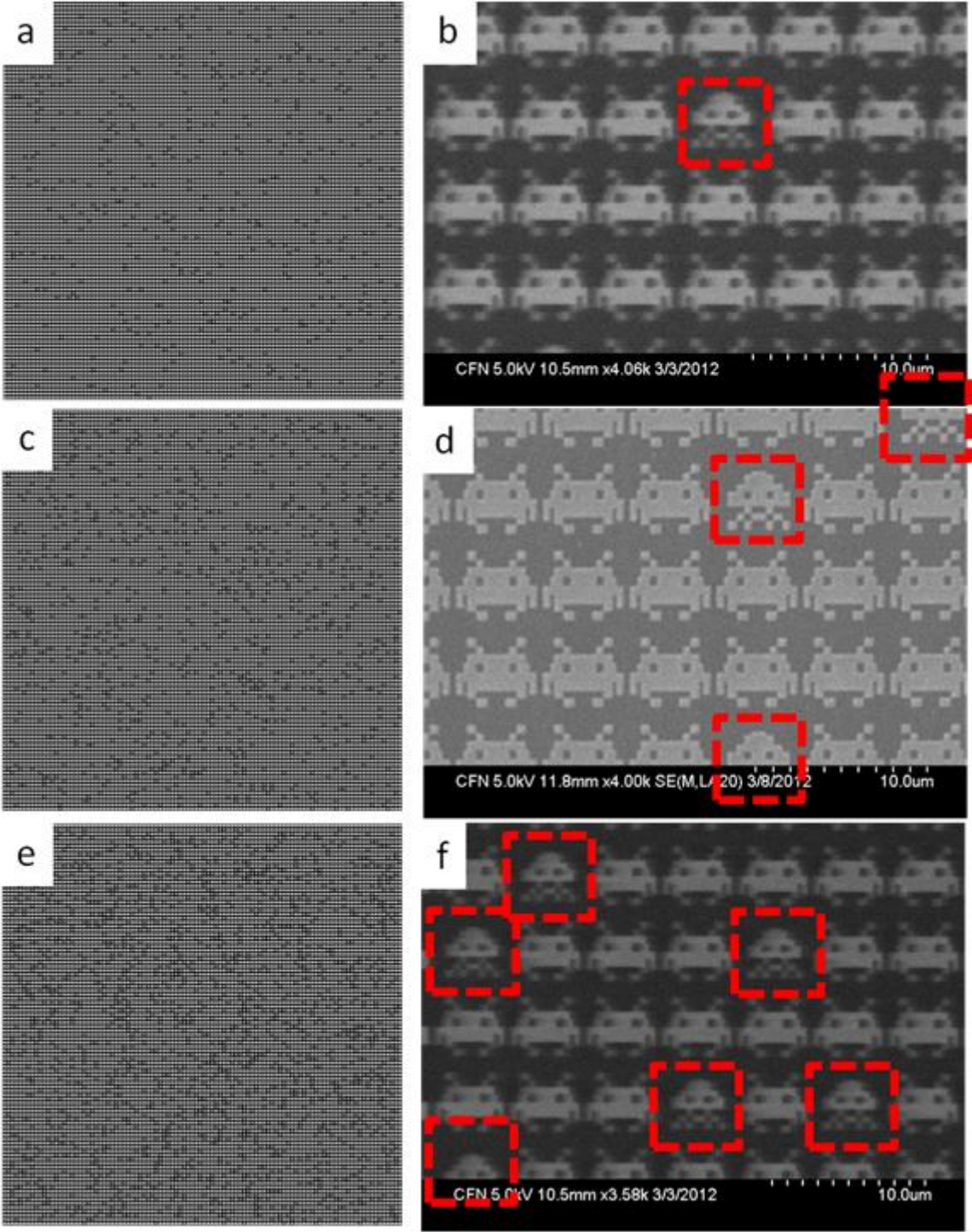


Figure 7-3. Masks with 5% (a,b), 10% (c,d) and 20% (e,f) of randomly distributed defect.

For comparison, the insets in the left column depict binary mask generated with MATLAB. The insets 3a, 3c, 3e represent the binary mask in the form that was used in the electron beam lithography.

7.4.2 EXPERIMENTAL SETUP

In order to verify the concept of defect tolerance in GTI, an experiment utilizing a compact EUV capillary discharge laser (CDL) was designed. The light source used in the experiment is well fitted to that purpose as it provides coherent illumination with high average power. More detailed description of the capillary discharge laser and its parameters can be found in chapter 2 and references [11, 12]. Inline geometry was used to illuminate the Talbot mask. The schematic of the experimental setup is shown on the Figure 7-4. The main components of the setup are the light source (EUV laser), the Talbot mask, and the recording medium.

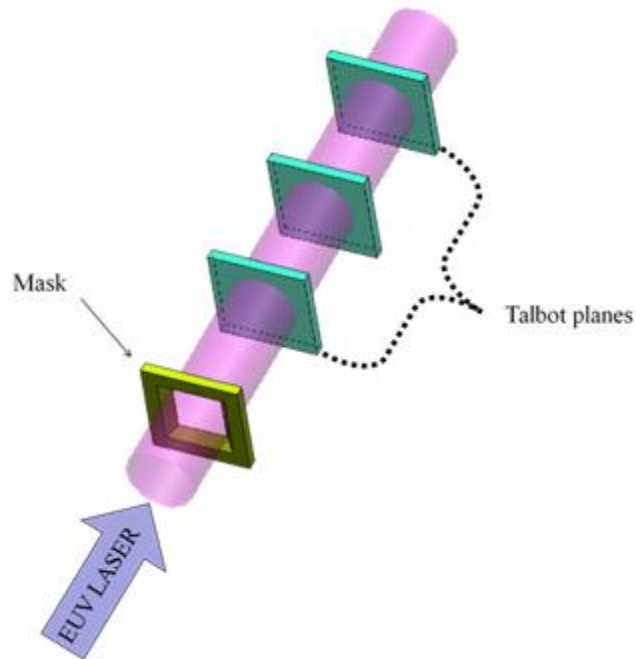


Figure 7-4. Schematic of experimental setup. The EUV laser beam illuminates the Talbot mask and the sample is placed at the Talbot planes.

A piece of silicon wafer coated with a photoresist was placed to record the self-image. The recording medium and its preparation protocol is described in greater detail in the appendix 2. The distance between the mask and the sample planes was constantly measured with a displacement sensor and controlled with an actuator. The exposure took 300 shots from the CDL. The sample was placed at the first Talbot plane. After the exposure, the sample was developed with a 25% solution of methyl-isobutyl ketone in isopropyl alcohol. Subsequently, the sample was rinsed with pure isopropyl alcohol and blown dry with ultra-high purity nitrogen. Samples were imaged with a scanning electron microscope (SEM) and atomic force microscope (AFM).

7.4.3 EXPERIMENTAL RESULTS

The replicas of the masks printed in the photoresist were examined by two independent methods, namely, atomic force microscopy and scanning electron microscopy. An SEM image of the reconstruction of a mask with an entire row of defects is shown in the Figure 7-5. The inset to the left shows the SEM image of a mask whereas the insets to the right show the mask copy at the first Talbot plane. The SEM image of the reconstruction is taken at the location where the defect in the mask exists. The exact loci of the defect in both the mask and its replica are indicated with yellow dashed lines. The presence of the defect in the mask replica manifests itself as a lighter background in the defected row. However, the features in the mask are printed with no visible deterioration.

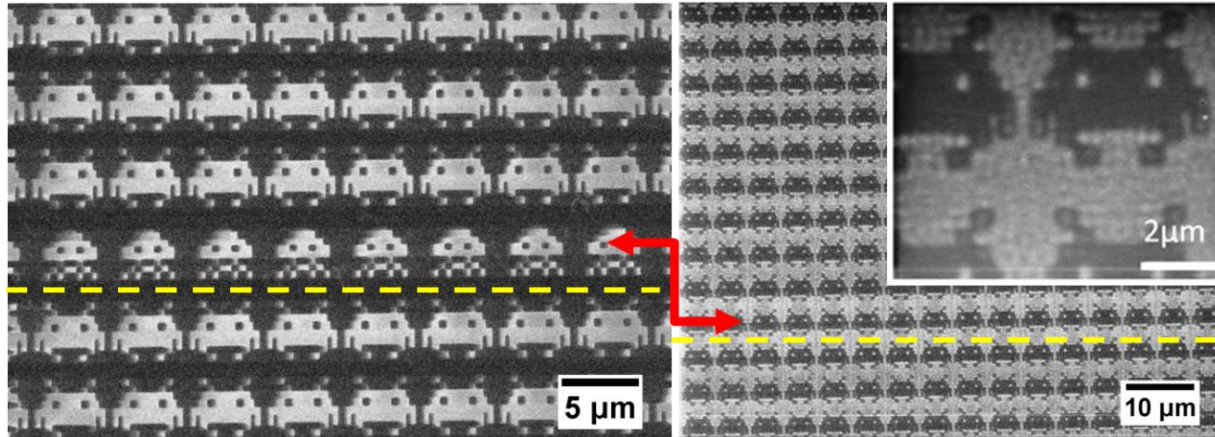

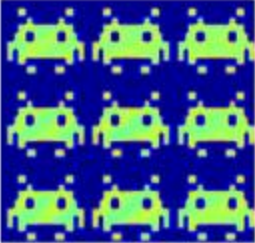


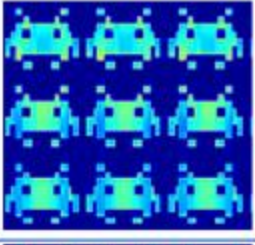
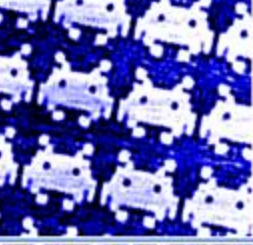

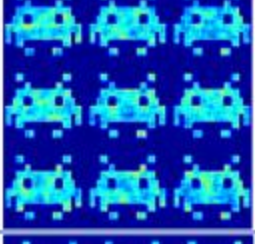
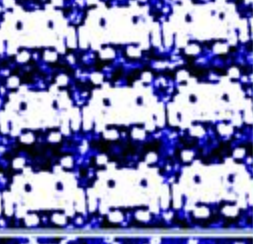

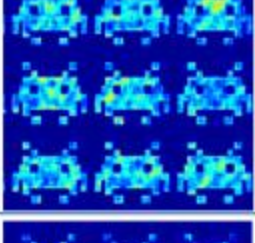
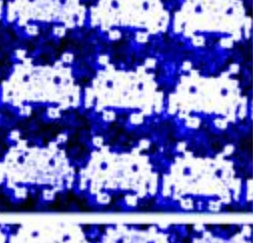

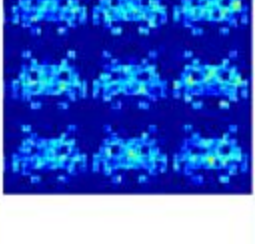
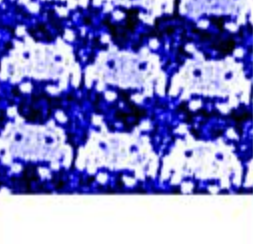


Figure 7-5. Defect tolerance feature of Generalized Talbot Imaging. Left - SEM micrograph of the periodic mask with an entire row of defects. Right: SEM micrograph of the print in photoresist obtained at the first Talbot plane. The row with defects in the mask reconstructs in a defect-free row (underlined and indicated by the arrow) in the reconstructed image

The SEM imaging was performed for limited mask replicas only. The thickness of the resist (~70nm) and the fact that the patterns were defined only at the surface (~25nm) of the resist resulted in charging effects which diminished the image quality. On top of that, the thin layer of the resist was getting activated with the scanning electron beam that led to further image deterioration. Independent of the SEM analysis, the replicas of all the masks shown in the previous section were inspected by the AFM, which in the course of the analysis turned out to be much less invasive method of examination. The results are summarized in table 7-2. The table entries illustrate binary masks with different defect concentration (column 2) along with corresponding numerical reconstructions (column 3); the last column (4) contains AFM scans of the patterned resist.

Table 7-2. Defect tolerance summary. Rows contain the image of binary mask, corresponding numerical reconstruction and experimental results for 0.01%, 1%, 5%, 10% and 20% concentration of defect (Def. Conc.).

Def. Conc.	Binary Mask	Numerical Reconstruction	Reconstruction in Resist
0.01%			
1%			
5%			
10%			
20%			

A result worthwhile noticing in the experimental data presented is the fact that regardless of the presence of the defect, the main feature of the mask is still being printed. As expected, the quality of the replicas diminishes with increasing defect concentration. However, even in the case when one fifth of the mask is defective (mask #5), the silhouette of the native cells is kept.

The defect tolerance property that is observed in the result summary (table 7-2), is due to both lateral and longitudinal periodicity of the light diffracted by the mask. The intensity of the light diffracted by the defect is proportional to its size. It is also inversely proportional to the square of the propagation distance. The contribution from the defect is smaller area wise than the contribution from the native motif of the mask. Thus the contribution from the healthy mask (second term in the equation 14) overwhelms the input of the field diffracted by the defect (first term in the equation 14). It is expected, that different defect layouts have different effect on the ultimate quality of the replica. Direct comparison of the replicas rendered by masks with different defect layouts is not conclusive. For example, clustered defect of different sizes should not be compared with a defect distributed randomly throughout the mask. As a consequence, a case-by-case analysis is required. The influence of the defect density on the quality of the print is subject to a more detailed analysis presented in the section to follow.

7.5 DATA ANALYSIS

The prints obtained with masks containing 0.01%, 1%, 5%, 10% and 20% were analyzed comparing their resemblance to the original mask. To quantify the original-to-replica similarity, the peak value of the cross correlation function between the replica and the original mask was used. The cross correlation function indicates the degree to which two images are similar (correlated). The bound values of the cross correlation function are -1 and +1. The upper bound

value of the cross correlation function indicates that two images are identical; the lower bound indicates that the images are complementary to one another. The value zero of the cross correlation function indicates no resemblance between the images. The cross correlation between two images is a standard approach to feature detection [13]. The peak value of the normalized cross correlation function used to quantify the image quality is given by equation 15.

$$\gamma(u, v) = \left| \frac{\sum_{x,y} [f(x, y) - \bar{f}_{u,v}] [t(x-u, y-v) - \bar{t}]}{\left\{ \sum_{x,y} [f(x, y) - \bar{f}_{u,v}]^2 \sum_{x,y} [t(x-u, y-v) - \bar{t}]^2 \right\}^{0.5}} \right|_{\max} \quad (15)$$

Where $f(x,y)$ is the image printed, t -ideal native cell, \bar{t} - mean of the ideal native cell, $\bar{f}_{u,v}$ - is the mean of the image under the region subtended by t .

The analysis was performed on single cells, which were obtained by sectioning out $5 \times 5 \mu\text{m}^2$ squares from the entire $20 \times 20 \mu\text{m}^2$ AFM scan. The cells which underwent the analysis are shown in the Figure 7-6. From each print rendered by masks with different defect densities, 9 cells were sectioned. For each sectioned cell, its peak value of cross correlation with the ideal native cell was calculated. Out of the 9 cross correlation values obtained for different defect densities, the mean value and the standard deviation were calculated. The mean values of cross correlation along with the error bars are plotted in the Figure 7-7.

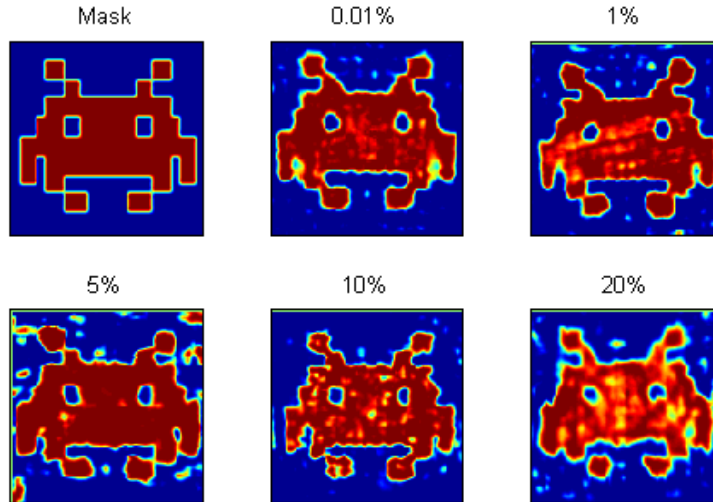


Figure 7-6. The ideal native cell and cells sectioned from the AFM scans which were subjected to analysis. The prints were rendered by masks with different defects.

For comparison, the cross correlation value was calculated for the ideal native cell and the reconstructions obtained via numerical simulation. The results of the analysis are summarized in table 7-3 and plotted in the Figure 7-7. One can observe good correspondence between simulation and measurement.

Table 7-3. Summarized values of the normalized cross-correlation between the original and replica for different defect concentration.

	0.01%	1%	5%	10%	20%
<i>Simulation</i>	$\gamma_5^N =$ 0.894	$\gamma_5^N =$ 0.887	$\gamma_5^N =$ 0.8804	$\gamma_{10}^N =$ 0.8665	$\gamma_{20}^N = 0.8199$
<i>Experiment</i> (mean)	γ_{001} =0.9335	γ_1 =0.9089	$\gamma_5 =$ 0.8484	$\gamma_{10} =$ 0.8661	$\gamma_{20} =$ 0.8317

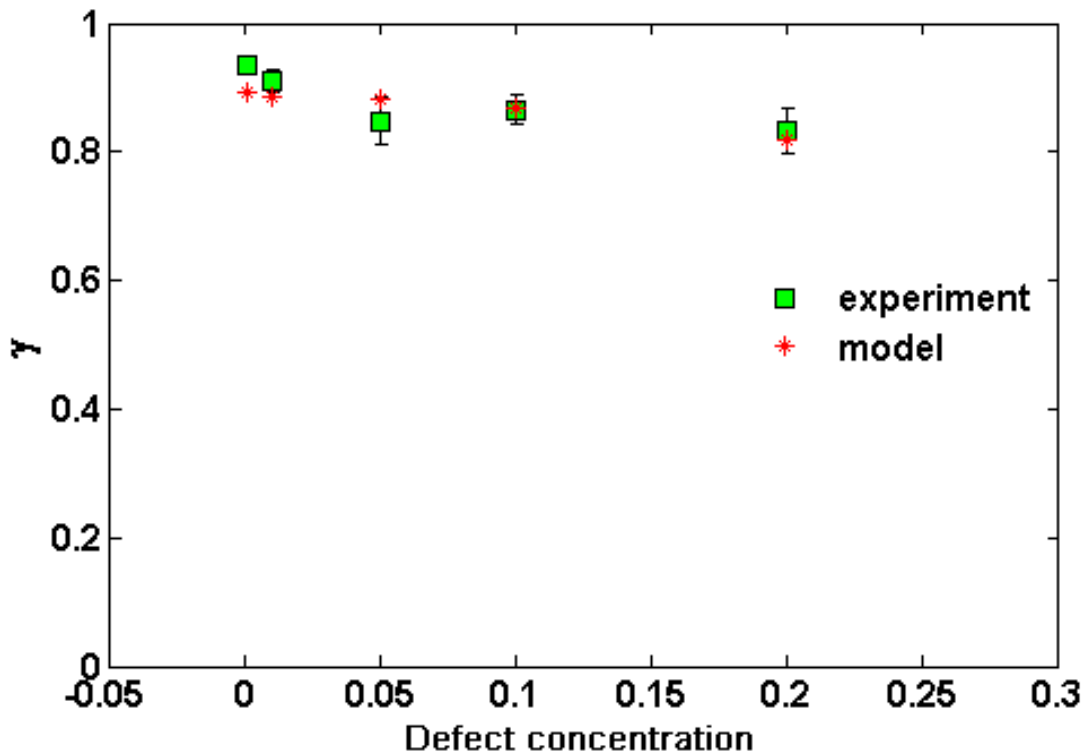


Figure 7-7. Image quality as a function of defect concentration. Results of the experiment compared to numerical calculation. The insets shown on the plot are the sections retrieved from full AFM scans.

A slight discrepancy is observed between the values of measured and modeled image quality (γ). The majority of the model image quality (1%, 5%, 10%, 20%) lay within the error bar of the measured experimental data. The discrepancies may be attributed to errors in scanning with the AFM induced by different environment conditions (temperature, humidity, electromagnetic, acoustic and building mechanical noise). The probe used for scanning was different for most of

the cases, which also contributes to the ultimate error. Another contribution to the error is the resist surface roughness.

7.6 SUMMARY

In summary, in this chapter the GTI technique has been examined with regards to defect tolerance. Masks with five different layouts and concentrations of defects were investigated. A single cell (defect to mask ratio of 0.01%), an entire row of cells (defect to mask ratio of 1%), layouts with 5%, 10% and 20% of randomly distributed defect were tested. The obtained results are in good agreement with theoretical considerations both analytical and numerical. Despite of defects purposely planted within the masks, the native features of masks still faithfully reconstruct. The influence of the defect on the image quality was quantified and analyzed. The defect concentration deteriorates the image quality as predicted. Yet, the method's tolerance for defects is high. The replicas rendered by the masks with 0.01%, 1% of defect exhibit no image deterioration that is observable with AFM and SEM. The masks with 5%, 10% and 20% of defected cells were showing good resemblance to the ideal native cell measured by the γ factor between 80%-90%. The image starts visibly deteriorate once the defect concentration exceeds 10%. Although the error tolerance analysis must be made for each individual case, a plausible methodology to assess the error tolerance of the method was presented using 2D image correlation that agrees with the numerical data.

The defect tolerance feature of the GTI is an inherent property of the method. It is due to periodic character of the mask. The defect tolerance is powerful feature of GTI which allows for successful printing even though over a tenth part of the mask is defective. Part of the work presented in this chapter has been published in [14].

7.7 REFERENCES

- [1] *Talbot lithography: Self-imaging of complex structures*, A. Isoyan, F. Jiang, Y. C. Cheng, F. Cerrina, P. Wachulak, L. Urbanski, J. Rocca, C. Menoni, and M. Marconi, *J. Vac. Sci. Technol. B*, **27**, 2931 (2009).
- [2] *Restoration of faulty images of periodic objects by means of self-imaging*, H. Dammann, G. Groh, and M. Kock. *Appl. Opt.* **10**, 1454 (1971).
- [3] *Making an array illuminator based on the talbot effect*, A.W. Lohmann and J.A. Thomas. *Appl. Opt.* **29**, 4337 (1990).
- [4] *Analysis of a scheme for de-magnified talbot lithography*, L. Urbanski, M. C. Marconi, A. Isoyan, A. Stein, C. S. Menoni, and J. J. Rocca, *J. Vac. Sci. Technol. B*, **29**, 06F504 (2011).
- [5] *Single molecule detection using surface-enhanced Raman scattering (SERS)*, K. Kneipp, Y. Wang, H. Kneipp, L.T. Perelman, I. Itzkan, R.R. Dasari, and M.S. Feld. *Phys. Rev. Lett.* **78**, 1667 (1997).
- [6] *Surface plasmon resonant interference nanolithography technique*, X.G. Luo and T. Ishihara, *Appl. Phys. Lett.* **84**, 4780 (2004).
- [7] *Surface plasmon interference nanolithography*, Z.W. Liu, Q.H. Wei, and X. Zhang, *Nano Lett.* **5**, 957 (2005).
- [8] *Optical metamaterials-more bulky and less lossy*, C.M. Soukoulis and M. Wegener, *Science*, **330**, 1633 (2010).

- [9] *Fabrication and tuning of nanoscale metallic ring and split-ring arrays*, A. K. Sheridan, A. W. Clark, A. Glidle, J. M. Cooper, and D. R. S. Cumming, *J. Vac. Sci. Technol. B*, **25**, 2628 (2007).
- [10] *Fractional montgomery effect: a self-imaging phenomenon*, A.W. Lohmann, H. Knuppertz, and J. Jahns, *J. Opt. Soc. Am. A*, **22**, 1500 (2005).
- [11] *Demonstration of a high average power tabletop soft x-ray laser*, B. R. Benware, C. D. Macchietto, C. H. Moreno, and J. J. Rocca, *Phys. Rev. Lett.* **81**, 5804 (1998).
- [12] *Generation of millijoule-level soft-x-ray laser pulses at a 4-hz repetition rate in a highly saturated tabletop capillary discharge amplifier*, C. D. Macchietto, B. R. Benware, and J. J. Rocca, *Opt. Lett.* **24**, 1115 (1999).
- [13] *Pattern classification and scene analysis*, Richard O. Duda and Peter E. Hart, *Wiley-Interscience Publication, New York* (1973).
- [14] *Defect tolerant extreme ultraviolet nanoscale printing*, L. Urbanski, A. Isoyan, A. Stein, J.J. Rocca, C.S. Menoni and M.C. Marconi, *Opt. Lett.* **37**, 3633 (2012).

APPENDIX 1 DERIVATION OF THE TALBOT DISTANCE IN THE DEMAGNIFIED TALBOT IMAGING.

By applying definitions of the operators in the set geometry of the problem (Figure 6-1, chapter 6) we obtain the solution for the diffracted field on the following form (eq. 10, chapter 6):

$$S = \sqrt{\frac{z}{f-s} \left| \frac{z}{i\lambda(f-s-z)(f-s)} e^{\frac{ik}{z}x_2^2} \cdot \int_{-\infty}^{\infty} U\left(x_1 \frac{z}{f-s}\right) \exp\left[-ik \frac{z(x_2-x_1)^2}{(f-s-z)(f-s)}\right] dx_1 \right.} \quad (1)$$

The integrand can be then viewed as two terms: the first one is responsible for de-magnification in the image. It depends on the mirror to mask distance. The second term describes the propagation with a phase acquired by reflection from a concave mirror. From equation 1 one can calculate the Talbot distance in the following way:

$$z_T = \frac{(f-s-z)(f-s)}{z} = 2 \frac{Mp^2}{\lambda} \quad (2)$$

$$\frac{(f-s-z)}{z} = 2 \frac{Mp^2}{(f-s)\lambda} \quad (3)$$

$$\frac{f-s}{z} - 1 = 2 \frac{Mp^2}{(f-s)\lambda} \quad (4)$$

$$\frac{f-s}{z} = 2 \frac{Mp^2}{(f-s)\lambda} + \frac{(f-s)\lambda}{(f-s)\lambda} \quad (5)$$

$$\frac{f-s}{z} = 2 \frac{Mp^2 + (f-s)\lambda}{(f-s)\lambda} \quad (6)$$

$$z = \frac{\lambda(f-s)^2}{2Mp^2 + (f-s)\lambda} \quad (7)$$

$$z_T = f - s - z \quad (8)$$

$$z_T = f - s - \frac{\lambda(f-s)^2}{2Mp^2 + (f-s)\lambda} \quad (9)$$

$$z_T = \frac{2Mp^2(f-s) + \lambda(f-s)^2 - \lambda(f-s)^2}{2Mp^2 + (f-s)\lambda} \quad (10)$$

$$z_T = \frac{2Mp^2(f-s)}{2Mp^2 + (f-s)\lambda} \quad (11)$$

APPENDIX 2 RESIST PROCESSING

PMMA (Microchem Corp.)

Resist Type: 495PMMA A,

Concentration: 2% solids,

Solvent: Anisole,

Application: Spin Coating at 3500 RPM (Program F),

Thickness: 70±10nm,

Solvent drive-off baking: 60min @ 60°C,

Exposure: 60shots (free standing masks), 300shots (~25nm silicon nitride membrane of 200nm silicon membrane),

Post exposure baking (PEB): NONE,

Development: puddle,

Developing time: 45-70 seconds,

Developing solution: 25% MIBK (Methyl Iso-butyl Ketone) in IPA (Isopropanol),

Rinse: IPA - 20seconds,

CAUTION: The maximum modulation depth ~20-30nm.

SU-8 (Microchem Corp.)

Resist Type: SU-8,

Concentration: 5.7% solids,

Solvent: Cyclopentanone ,

Application: Spin Coating at 3500 RPM (Program G),

Thickness: 60±5nm,

Solvent drive-off baking: 60s @ 65°C, then 120s @ 95°C,

Exposure: ~20shots (free standing masks), ~300shots (~25nm silicon nitride membrane or ~200nm silicon membrane),

Post exposure baking (PEB): 8min @ 105°C,

Development: puddle,

Developing time: 3seconds,

Developing solution: 30% SU-8 Developer in IPA,

Rinse: IPA - 20seconds

Rinse: De-ionized (DI) Water - 20seconds,

CAUTION: The maximum modulation depth ~20-30nm.

AZPN 114 (Hoechst, Rohm Haas, AZ-materials)

Resist Type: AZPN114,

Concentration: 10% solids,

Solvent: AZ 1500 Thinner,

Application: Spin Coating at 1000 RPM (Program J),

Thickness: 100±10nm,

Solvent drive-off baking: 60s @ 120°C,

Exposure: ~5shots (free standing masks), ~120shots (~25nm silicon nitride membrane or ~200nm silicon membrane),

Post exposure baking (PEB): 8min @ 105°C,

COOLDOWN: 10min,

Development: puddle,

Developing time: 45seconds,

Developing solution: 50% (Tetra-methylammonium hydroxide)TMAH in DI water,

Rinse: De-ionized (DI) Water - 20seconds,

CAUTION: The full modulation depth, good for fabrication.

XR-1541 (HSQ - Hydrogen silsequioxane) (Dow Chemical Corp.)

Resist Type: XR-1541 ,

Concentration: 4-6% solids,

Solvent: MIBK,

Application: Spin Coating at 3500 RPM (Program G),

Thickness: 80±5nm,

Solvent drive-off baking: 60s @ 115°C,

Exposure: ~5shots (free standing masks), ~90shots (~25nm silicon nitride membrane or ~200nm silicon membrane),

Post exposure baking (PEB): NONE,

Development: puddle,

Developing time: 5-30 seconds,

Developing solution: 100% TMAH (LDD 26W),

Rinse: De-ionized (DI) Water - 20seconds.

Rinse: IPA - 20seconds.

CAUTION: Shelve life 6months, keep refrigerated, extremely sensitive to aging, extremely sensitive to fluctuation in the dose (warm up laser before exposing)

APPENDIX 3 NUMERICAL CALCULATIONS

Basic Fresnel Propagator

```
%*****  
  
% This code was developed to numerically calculate the Fresnel-Kirchhoff  
  
% diffraction integral. It written as a script rather than a function,  
  
% The user needs to provide the "Object" as a variable defined in the  
  
% MATLAB workspace. The output of this script is the intensity  
  
% distribution in the near field and the kernel of the transform  
  
% the variables used are commented 'on the fly' as the code executes.  
  
%*****  
  
tic  
  
[Nx,Ny]=size(Object);  
  
dx=140e-9;                   % x - pixel size  
  
dy=140e-9;                   % y - pixel size  
  
lambda=46.9e-9;             % wavelength of illumination  
  
Field=Nx*dx;                 % auxiliary object's field computation  
  
d=500e-6;                    % definition of the working distance  
  
  
NA=atan(Field/(2*d))         % auxiliary object's NA computation  
  
DOF=1*lambda/(NA^2)         % auxiliary object's DOF computation
```

```

res=lambda/NA

norm=sqrt(1/(Nx*Ny));           % normalization factor

%*****

% Definition of support for the Fresnel transformtion Kernel:

% /needs to be identical with the support of the mask/.

%*****

[k,l] = meshgrid(-(Nx-1)/2:1:(Nx-1)/2, -(Ny-1)/2:1:(Ny-1)/2);

%*****

% Definition of the Fresnel transformation Kernel:

% Definition of the inverse Fresnel transformation Kernel:

%*****

kernel=exp(-1i*pi*(k.^2*dx^2+l.^2*dy^2)./(lambda*d));

kernelR=exp(1i*pi*(k.^2*dx^2+l.^2*dy^2)./(lambda*d));

%*****

% optional phase (e.g. diverging, converging of tilted wavefront).

%*****

phase=exp(-1i*pi*(k*dx+l*dy)./.1e-5);

%*****

% intermittent output (final for continuous images e.g. hologram

```

```

% or Talbot mask reconstruction, calculation of the near field diffraction
% intensity distribution).

%*****

OUTi=fftshift(iff2(fft2(Object.*phase).*fft2(kernel)));

%*****

% optional normalization and halftoning techniques (to calculate a binary
% hologram mask) user needs to uncomment the technique of choice and leave
% others commented out. The routines for the halftoning operations are
% stored in the folder 'halftoning'.

%*****

nor1=(real(OUTi)-min(real(OUTi(:)))));

nor=nor1./max(nor1(:));

level=graythresh(nor);           % hard threshold with a level

%C=im2bw(nor,0.4120);

%C=screen_9u(nor);

C=screen_16u(nor);             % this routine will be executed

%C=floyd_serp(nor);

%C=stucki(nor);

figure, imagesc(C);           % plotting the binary hologram

```



```

%C=abs(C-1); % optional tone reversal

%*****

% optional reconstruction for quality check

%*****

OUT1=fftshift(iff2(fft2(real(C)).*fft2(kernelR)));

figure,imagesc(abs((OUT1.^2))); axis square % plotting the binary hologram

toc % stops timer (returns time elapsed)

```

Talbot Carpet Calculation (external function)

```

function y = carpet(x)

%*****

% This code was developed to numerically calculate the x-z field
% distribution, called the Talbot carpet.

% The user needs to provide the "Object" as a 1-D array defined in the
% MATLAB workspace (e.g. a profile of a rectangular binary grating).

% The output of this script is the intensity

```

```

% distribution in x-z plane.

% The calculation is carried out iteratively for each slice on the z axis.

% The variables used are commented 'on the fly' as the code executes.

% This function is also useful for calculation the field after diffracting

% structures such as Fresnel zone plates.

%*****

close all

lambda = 46.9e-9;           % wavelength of illumination

period = 5e-6;             % period of the structure (define in
                           % the MATLAB workspace)

zT=(period)^2/lambda;     % calculation of-

                           % -the Talbot distance

N=1400;                    % affixed number-

                           % -of points per slice (user defines)

dz=2*zT/N;

%*****

% strat the loop

%*****

for n=1:N

```

```

        y(:,n)=fresnel(x,dz*(n))      ;      % separate function propagator

%*****

% terminate the loop

%*****

end

imagesc(abs(y(2900:3200,:)))      % plot output

```

Talbot Carpet Calculation (internal Fresnel propagator function)

```

function g=fresnel(Object,d)

%*****

% This code was developed to numerically calculate the x-z field

% distribution, called the Talbot carpet. Is is an internal function called

% by the 'carpet.m' function.

% The user needs to provide the "Object" as a 1-D array defined in the

```

```

% MATLAB workspace (e.g. a profile of a rectangular binary grating) and the
% distance of propagation: 'd'.
% The output of this script is the intensity
% distribution in near field plane.
% The calculation is carried out iteratively for each slice on the z axis.
% The variables used are commented 'on the fly' as the code executes.
%*****

[Nx,Ny]=size(H');

%*****

% in case the propagation distance has not been defined previously, it is
% set at 500 microns by default
%*****

if nargin == 0
    d=0.5e-3;
end

lambda=46.9e-9;           % wavelength of illumination
dx=lambda;               % x - pixel size
dy=lambda;               % y - pixel size
%*****

```

```

% Definition of support for the Fresnel transformation Kernel:

%*****

[k,l] = meshgrid(-(Nx-1)/2:1:(Nx-1)/2, -(Ny-1)/2:1:(Ny-1)/2);

%*****

% Optional lens parameter definition (de-magnified Talbot carpet)

%*****

focal=25e-2;

L=exp(-1i*pi*(k.^2*dx^2+l.^2*dy^2)./(lambda*focal));

%*****

% Definition of the Fresnel transformation Kernel:

%*****

kernel=exp(i*pi*sqrt(k.^2*dx^2+l.^2*dy^2+d.^2)./lambda);

g=fftshift(iff2(fft2(H.*L).*fft2(kernel)))./sqrt(lambda*d);

% ^---here goes the lens operator

```